SYNTHESIS, PROPERTIES AND APPLICATIONS OF FUNCTIONAL POLYMER NANOCOMPOSITES

by

Lingqi Huang

A thesis submitted in partial fulfillment
of the requirements for the degree of
Doctor of Philosophy (PhD) in Natural Resources Engineering

The Faculty of Graduate Studies
Laurentian University
Sudbury, Ontario, Canada

© Lingqi Huang, 2019

THESIS DEFENCE COMMITTEE/COMITÉ DE SOUTENANCE DE THÈSE
Laurentian Université/Université Laurentienne
Faculty of Graduate Studies/Faculté des études supérieures

Title of Thesis Titre de la thèse	SYNTHESIS, PROPERTY AND APPLICATION OF FUNCTIONAL POLYMER NANOCOMPOSITES	
Name of Candidate Nom du candidat	Huang, Lingqi	
Degree Diplôme	Doctor of Philosophy Science	
Department/Program Département/Programme	Natural Resource Engineering	Date of Defence Date de la soutenance November 30, 3018

APPROVED/APPROUVÉ

Thesis Examiners/Examinateurs de thèse:

Dr. Zhibin Ye
(Supervisor/Directeur(trice) de thèse)

Dr. Ramesh Subramanian
(Committee member/Membre du comité)

Dr. Junfeng Zhang
(Committee member/Membre du comité)

Dr. Marianna Kontopoulou
(External Examiner/Examinateur externe)

Dr. Stefan Siemann
(Internal Examiner/Examinateur interne)

Approved for the Faculty of Graduate Studies
Approuvé pour la Faculté des études supérieures
Dr. David Lesbarrères
Monsieur David Lesbarrères
Dean, Faculty of Graduate Studies
Doyen, Faculté des études supérieures

ACCESSIBILITY CLAUSE AND PERMISSION TO USE

I, **Lingqi Huang**, hereby grant to Laurentian University and/or its agents the non-exclusive license to archive and make accessible my thesis, dissertation, or project report in whole or in part in all forms of media, now or for the duration of my copyright ownership. I retain all other ownership rights to the copyright of the thesis, dissertation or project report. I also reserve the right to use in future works (such as articles or books) all or part of this thesis, dissertation, or project report. I further agree that permission for copying of this thesis in any manner, in whole or in part, for scholarly purposes may be granted by the professor or professors who supervised my thesis work or, in their absence, by the Head of the Department in which my thesis work was done. It is understood that any copying or publication or use of this thesis or parts thereof for financial gain shall not be allowed without my written permission. It is also understood that this copy is being made available in this form by the authority of the copyright owner solely for the purpose of private study and research and may not be copied or reproduced except as permitted by the copyright laws without written authority from the copyright owner.

ABSTRACT

Polymer nanocomposites have been extensively studied and have found numerous applications as they provide versatile materials with substantially enhanced properties. Despite the enormous developments, design of novel value-added polymer nanocomposites with new superior functional properties through convenient low-cost synthesis remains a continuous challenge. This thesis demonstrates the alternative, simple design of several novel polymer nanocomposite systems with enhanced mechanical, surface, or catalytic properties.

Firstly, a new method for the modification of cellulose nanocrystals (CNCs) is developed with the use of hyperbranched polyethylene ionomers containing cationic quaternary ammonium ions through an ionic interaction mechanism. A systematic study has been undertaken on the modification process and the modified CNCs. In contrast to original CNCs that can only disperse in water or few highly polar solvents, ionomer modified CNCs are able to disperse in several nonpolar or low polarity organic solvents. Dispersions of several modified CNCs in THF exhibit the unique thixotropic rheological behavior. The modified CNCs have also become dispersible in a commercial non-polar hydrophobic ethylene-octene copolymer (EOC) elastomer due to the presence of nonpolar polyethylene modification layer. Based on thermal, rheological, and tensile mechanical characterizations, EOC nanocomposites filled with the modified CNCs are significantly reinforced with nearly doubled tensile modulus relative to neat EOC while with a much better-maintained elongation at break relative to those filled with unmodified CNCs or surfactant-modified CNCs.

Secondly, a class of CNC-sodium alginate (SA) nanocomposites derived exclusively from sustainable biopolymers has been designed to fabricate tough-strong nanocomposite film. A systematic study on the effects of composite composition on the optical, thermal, and mechanical properties of the prepared films has been undertaken. The calcium ion cross-linked composite films maintain high film transparency with higher thermal and mechanical properties than the uncross-linked films, indicating that the calcium ions play an important role in the enhancement of mechanical and thermal properties. The effects of various metal ions on film mechanical properties have also been studied. As a result, the bivalent calcium ions show the most optimum effect to render strong-tough composite films.

Thirdly, hybrid composites of multi-walled carbon nanotubes (MWCNTs) decorated with polycyclopentene crystals have been synthesized by a novel in situ Pd-catalyzed cyclopentene polymerization technique. It is demonstrated that the method offers a convenient, large-scale, one-pot noncovalent surface decoration of polycyclopentene crystals on the MWCNTs. Controlling the catalyst loading and/or polymerization time in the polymerization effectively tunes the composition and morphology of the as-prepared hybrid composites. Interestingly, films made of the composites show the characteristic lotus leaf-like superhydrophobicity featured with high water contact angle (> 150°), low contact angle hysteresis (< 10°), and low water adhesion, while being electrically conductive.

Lastly, a systematic study on ligand-assisted selective hydrogenation of alkynes (phenylacetylene and diphenylacetylene) over three Pd nanocatalysts have been presented with the purpose of identifying the most optimum ligands. Five ligands, including quinoline, pyridine, DMSO, 3,6-dithia-1,8-octanediol (DTO), and triphenylphosphine, have been

screened with their performance compared. It is demonstrated that the sulfur-containing DTO and phosphine-containing triphenylphosphine are the more efficient and practical ligands in improving the alkene selectivity of the catalysts.

ACKNOWLEDGEMENTS

I would like to thank my supervisor Dr. Zhibin Ye. I sincerely appreciate the learning opportunity he provided to me; I appreciate his guidance, insightful advice, and financial support throughout my study at Laurentian. In particular, I am grateful for his helpful suggestions and encouragements when I felt depressed and lost in my projects.

I am thankful to faculty and staff including Dr. Ramesh Subramanian, Dr. Krishna Challagulla, Henry Ylitalo, Greg Lakanen, and Natalie Boutet at Bharti School of Engineering, Dr. Jeffrey Shepherd, Luc Beaudet, and Paul Guérin at Department of Chemistry and Biochemistry, Dr. Lixin Xu and Dr. Jintao Yang at Zhejiang University of Technology (China), who have been really helpful in assisting me in my research. Specially, I enjoyed my many talks with Henry Ylitalo.

I am also thankful to my lab mates, Dr. Xiang Peng, Dr. Zhongming Dong, Mark Grundy, Zhe Chen, etc. They have been very helpful in sharing their lab skills with me in my first year. In addition, I am happy to have those people with me at specific timeline during my program: Henry Su, Dr. Asghar Ali, Dr. Muddassir Ali, Said Mahboob, Mohammed Faisaluddin, Saad Alessa, Dr. Jianjun He, Dr. Xudong Liu, Daniel De Almeida, Seyma Uslu, Jacob Schmidt, Dr. Madagonda M Vadiyar, Scarlett Zheng, and my dear family members.

Table of Content

List of Figures

List of Schemes

List of Tables

List of Abbreviations

$AETMA^+BF_4^-$	[2-(acryloyloxy)ethyl]Trimethylammonium Tetrafluoroborate
AFM	Atomic Force Microscopy
ATR	Attenuated Total Reflectance
$CDCl_3$	Deuterated Chloroform
CNCs	Cellulose Nanocrystals
CNTs	Carbon Nanotubes
CNFs	Cellulose Nanofibrils
CTAB	Cetyltrimethylammonium Bromide
DLS	Dynamic Lighting Scattering
DMA	Dynamic Mechanical Analysis
DMSO	Dimethyl Sulfoxide
d_p	Z-average Hydrodynamic Diameter
DPA	Diphenylacetylene
DNA	Deoxyribonucleic Acid
DSC	Differential Scanning Calorimetry
EOC	Ethylene-Octene Copolymer
FID	Flame Ionization Detector

FTIR	Fourier-Transform Infrared
G’	Storage Modulus
G”	Loss Modulus
GC	Gas Chromatography
GPC	Gel Permeation Chromatography
^{1}H NMR	Proton Nuclear Magnetic Resonance
LbL	Layer by Layer
MWCNTs	Multi-Walled Carbon Nanotubes
M_w	Weight-Average Molecular Weight
NHSK	Nanohybrid Shish-Kebab
PA	Phenylacetylene
PDI	Polydispersity Index
PCP	Polycyclopentene
PE	Polyethylene
PS	Polystyrene
PMMA	Poly(methyl methacrylate)
PTFE	Polytetrafluoroethylene
PVA	Polyvinyl Alcohol

PVDF	Polyvinylidene Fluoride
rGO	Reduced Graphene Oxide
RSC	Refrigerated Cooling System
SA	Sodium Alginate
SEM	Scanning Electron Microscopy
T_c	Crystallization Temperature
$T_{c,onset}$	Onset crystallization Temperature
$T_{d,max}$	Peak decomposition Temperature
T_m	Melting Temperatures
TEM	Transmission Electron Microscopy
TGA	Thermogravimetric Analysis
THF	Tetrahydrofuran
TOF	Turnover Frequency
UV	Ultraviolet
WAXRD	Wide Angle X-ray Diffraction
XRD	X-ray Diffraction
$[\eta]_w$	Weight-Average Intrinsic Viscosity
η^*	Complex Viscosity

ε_{max}	Maximum Tensile Strain
σ_{max}	Maximum Tensile Strength
δ	Phase Angle
ω	Frequency
ΔH_c	Crystallization Heat

Chapter 1

Introduction, Background and Research Objectives

1.1 Introduction

With the extensive efforts on nanotechnologies and nanomaterials in the last decades, the number of scientific publications and patents on polymer nanocomposites has continuously increased with the development of numerous new functional materials with improved thermal, mechanical, optical and other properties. Generally, polymer nanocomposites are defined as solid materials consisting of nanoparticles and polymeric substances.[1] The addition of nanoparticles brings advantageous value-added properties to the polymer nanocomposites. Polymer nanocomposites have been developed to modify light stability, thermal stability and mechanical behavior of the polymer matrices; they have also been applied to add new properties to the polymer matrices, such as conductivity, permeability, superhydrophobicity, etc.[2]

Nanoparticles are particles with at least one dimension below 100 nm and with fascinating nanoscale physicochemical and biological properties that differ from their bulk counterparts.[2] Based on dimensions, they can be classified into 0D, 1D, 2D and 3D nanoparticles.[3] The various nanoparticles are all potential components for novel nanocomposites.[4]

Many different types of nanoparticles have been incorporated within polymer matrices for the fabrication of polymer nanocomposites in the form of engineering bulk materials, films or hybrid powders. A prominent example of the application of nanoparticles in polymeric material is carbon black reinforced rubber tire, consisting of rubber material and carbon nanoparticles in the size range of 20–50 nm.[5] Because of the carbon nanoparticles, the rubber tire exhibits impressively enhanced properties including modulus, strength and flame resistance, compared to conventional filled rubber material.[6] Different nanoparticles have been applied for fabrication of many different types of polymer nanocomposites. The range of applications for polymer nanocomposites developed to date is very broad, including membranes, fibers, catalysts, cosmetics, packages, batteries, capacitors, modern organic solar cells and paints.[2] It has also been found that the performance of polymer nanocomposite intimately related to the characteristics of nanoparticles, such as the geometric structure, specific surface area, surface modification, surface functionality, and the polymer matrix–nanoparticle interface.[1] All the above factors should be taken into consideration when designing polymer nanocomposites and studying their applications.

1.2 Nanoparticles

Nanoparticles are now commonly used in polymer science and in the other fields of science like electronics, energy, catalysts.[1] To date, many synthetic or natural nanoparticles have been employed. In their classification based on dimensions, quantum dots, nano-clusters and nano-spheres are considered as 0D nanoparticles; nanowires, nano-rods, nanotubes are

1D nanomaterials. 2D nanomaterials display shapes such as disk, plate, sheet or ribbon; while 3D nanomaterials show topology structures that combine the above-mentioned nanostructures.

Nanoparticles have also been divided into different types depending on their properties and applications.

Based on the composition, nanoparticles can also be classified into metal-based, ceramic-based, carbon-based and organic-based nanoparticles. Metal nanoparticles such as cobalt, copper, iron, platinum, palladium nanoparticles are synthetic particles; they usually show specific physical properties, such as the catalytic properties for different heterogeneous chemical reactions.[7] In the case of metal oxide and ceramic particles, the reduction to nano dimensions endows the material new magnetic, catalytic or optical features.[8] Carbon nanotubes and graphene nanosheets are two popular carbon-based nanomaterials, which possess superior intrinsic mechanical and electrical properties.[9] In addition, the well-known carbon black, carbon nanofiber and sometimes the activated carbon in nanoscale are all carbon-based nanomaterials. Polymeric nanoparticles, such as micelles and dendrimers, are usually classified as organic nanoparticles.[10]

Primarily, nanoparticles can be prepared using various methods, either by breaking down bulky materials to nanoscale particles (top-down) or by building up from atoms to nanoparticles (bottom-up).[10] Table 1.1 shows some representative synthetic methods for different nanoparticles. Besides, nanoparticles are not necessarily produced by size modulation methods or nanotechnologies, but have also existed in nature. One example is the

cellulose nanofibril, a sustainable but robust carbohydrate nanomaterial that extracted from wood or cotton material.[11]

Table 1.1 Several synthesize methods of nanoparticles.[11]

Category	Synthetic Method	Nanoparticles
Bottom-up	Sol-gel	Carbon, metal, metal oxide, ceramic
	Spinning	Organic
	Chemical vapour deposition	Carbon, metal, ceramic
	Pyrolysis	Carbon, metal oxide
	Biochemical synthesis	Organic, metal
Top-down	Mechanical milling	Metal, ceramic, metal oxide
	Nanolithography	Metal
	Laser ablation	Carbon, metal oxide
	Sputtering	Metal
	Thermal decomposition	Carbon, metal oxide

1.3 Types of Polymer Nanocomposites

1.3.1 Polymer-Matrix Bulk Composites

Neat polymeric materials have some advantages over metal and mineral materials such as facile processability, low density, and low cost; they also have some disadvantages, such as low strength, low modulus, and low heat resistance. Reinforcing polymers with nanoparticles has been reported as a convenient way to improve material mechanical properties.[12] For example, a small amount of reinforcing nanoplatelets in a polymer matrix results in improved contact interface and consequently the improved mechanical properties (see Figure 1.1). Many different polymer matrices can be reinforced by various nanoparticles.

With only very small quantities of nanoparticles dispersed in the matrices, the properties of polymer matrices can be vastly changed.[13]

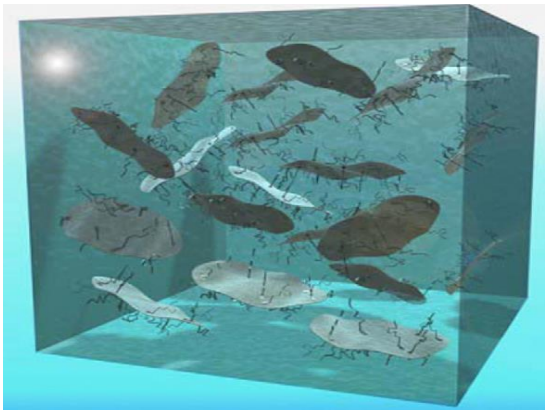

Figure 1.1 Schematic picture of a polymer-clay nanocomposite material with exfoliated clay sheets within the polymer matrix.[12]

Polymer nanocomposites can be prepared with conventional approaches, retaining the basic intrinsic properties, overcoming some disadvantages and presenting some new properties.[14] The combination of several different commercial polymers or high-performance engineering polymers with nanoparticles such as carbon nanofibers, metal oxide nanoparticles, or natural nanoclays have been presented using different approaches.[14] Njuguna et al. reported in most cases the beneficial effects (improving the glass transition temperature, thermal stability, storage modulus, tensile strength, crystallinity, etc.) of a small amount of nanoparticles.[14] More specifically, metal oxide nanoparticles have been applied in preparing photoluminescence polymer composites.[15,16] Ferrite nanoparticles have been used in developing polymeric composite materials with magnetic property.[17] Carbon-based nanoparticles, metallic nanotubes and conjugated polymer nanostructures show potential applications in the fabrication of nanoelectronics with conducting polymers (such as

polyaniline, polypyrrole, poly(3,4-ethylene dioxythiophene)) and their derivatives.[18] The diversity of nanoparticles and polymer matrices provides great possibilities in preparing new functional polymer nanocomposites to satisfy different kinds of demands.

Polymer nanocomposite material is a heterogeneous system consisting of polymer and nanoparticles, with the nanoparticles discretely dispersed in the polymer. The addition of nanoparticles brings beneficial effects to the polymer matrix, and the effect is particle number dependent. Aggregates will reduce the effective number of nanoparticles; well-dispersed nanoparticles in a polymer matrix is preferred.[1] In the synthesis of polymer nanocomposites, several common methods have been developed to achieve good dispersion states of nanoparticles in a polymer matrix. Intercalation of polymer chains into the nanoparticles is considered as the main method in nanocomposite preparation.[19] The process could be taken in polymer melts or in polymer solutions. Under vigorous shear force, the added nanoparticles can be evenly distributed in the polymer matrix. With proper surface modification on the nanoparticles, an improved dispersity of nanoparticles in the polymer matrix can be achieved with the same intercalation methods.[20] In-situ polymerization is also a regular method that can be used to improve the dispersity of nanoparticles in a polymer matrix.[21] Composites can be obtained after polymerization of monomers in the presence of nanoparticles. The nanoparticles can be dispersed in dilute monomer systems; afterwards, the well-disperse state of nanoparticles can be maintained during the polymerization, purification step and other processes. Similarly, in-situ growth of nanoparticles in the presence of polymer chains is another method that allows control over particles distribution, as well as the size and morphology of the generated nanoparticles.[22-24] Depending on the application to be

accomplished, different methods have been selected for the preparation of polymer nanocomposite that are reinforced with well-dispersed nanoparticles (see Table 1.2).

Table 1.2 Examples of polymer-matrix nanocomposites.[20]

Polymer matrices	Nanoparticles	Applications
PMMA	SiO_2	Bone, dental substitute, optical device
Polycaprolactone	SiO_2	Tissue repair
Polycarbonate	SiO_2	Abrasion resistant coatings
Polyimide	SiO_2	Microelectronics
Polyaniline	Fe_3O_4	Microwave absorber
Polyethylenimine	Fe_3O_4	Magnetic resonance imaging
HDPE	TiO_2	Bone repair
LDPE	ZnO, Ag	Juice packaging
Poly(3,4-ethylene-dioxythiophene	V_2O_5	Cathode materials for lithium batteries
Nylon-6	Nanoclay	Films and bottles
Polypropylene	Nanoclay	Packaging
Epoxy	Nanoclay	Materials for electronics

1.3.2 Composite Hybrids

Both nanoparticles supported on polymeric materials and polymer coated nanoparticles can be considered as another type of polymer nanocomposites.[2] In the first case, the nanoparticles can be immobilized onto the polymer supports through the nanoparticle-polymer interaction. The immobilization is due to one or multiple factors such as flexible polymer chains, functional groups on polymer chains which enable efficiently immobilization of nanoparticles, van der Waals, electrostatic or hydrogen bonds.[25] Nanoparticles can also be anchored onto a polymer by in situ preparation of nanoparticles from precursors within the polymer system. For the latter case, polymeric substances can be attached to nanoparticles via

various noncovalent or covalent functionalization protocols.[26,27] Direct grafting of polymer moieties onto nanoparticles is a common covalent route in composites preparation. The grafting method offers a good control over polymer architecture (*i.e.*, polymer chain ordination, polymer shell thickness, functional ends, etc.) on various shapes of nanoparticles.[11,28] For grafting method, surface-initiated free radical polymerization, atom transfer radical polymerization, reversible addition−fragmentation chain-transfer polymerization are commonly used techniques. Noncovalent functionalization strategies are also found attractive in literatures; pi-pi interaction, ionic interaction and hydrogen bonding allow the realization of noncovalent functionalization for nanoparticles.[26] Table 1.3 provides several selected examples of polymeric composite hybrids.

Table 1.3 Examples of composite hybrids.[20,22,25]

Categories	Nanoparticles	Supports	Applications
Nanoparticles immobilized on polymers	Pd^0, Cu^0	Chitosan, synthetic polymer	Chemical catalytic reaction
	SiO_2	Alginate	Electrocatalystic system
	Pd^0, Pt^0, Au^0	Synthetic polymer	Biosensor
	Fe_3O_4, ZrO_2	Synthetic polymer	Metal ion sorption
Polymer graft-immobilized nanoparticles	Pd^0, Ag^0, Au^0, Fe_2O_3	Synthetic polymer	Catalytic reduction
	Au^0	Dextran	Raman spectroscopy detection
	Ag^0, Au^0	Synthetic polymer	Plasmonic nanostructure
	Ag^0	Synthetic polymer	Antibacterial activity

The combinations between nanoparticles and polymer substances are versatile. On one hand, there are many different types of nanoparticles, varying from 0D nanoparticles to multiscale nanoparticles. On the other hand, the numerous polymeric platforms vary from

natural polymers to synthetic polymers provide multiple possibilities. Moreover, their architectures and compositions can be tuned for various novel composites. To date, nanocomposites have been demonstrated to be applicable in fabricating multifunctional materials in biomedicines,[29,30] catalysts,[31,32] electronics,[33] coatings,[34] energy materials,[35] and others.

1.3.3 Other Types of Polymer Nanocomposites

Biomimetic nacre materials have recently become research of interest. Polymer nanocomposites have been prepared with ordered structures by mimicking natural nacre. Nacre materials utilize natural mineral particles and polymers such as carbohydrates and/or proteins, resulting in strong and tough composites such as bones, pearl shells, and wood.[18] Constructed by nanoparticles, polymers and some other components, the artificial nacre composite materials can also exhibit remarkable features, such as light weight, high strength and toughness.[36] During the past ten years, many structural polymer nanocomposites have been successfully fabricated using various nanoparticles such as $CaCO_3$ nanoplates, nanoclays, Al_2O_3 nanoflakes, graphene oxide nanosheets, reduced graphene oxide nanosheets, etc.[37,38] In Figure 1.2 (a,b,c), an artificial nacre material is presented, composing of a large volume fraction of Al_2O_3 nanoflakes and a small volume fraction of polymer moieties. The obtained film shows excellent mechanical tensile strength. Cellulose nanocrystal (CNC) is also considered as a promising nanomaterial for the preparation of superior strong composites (see Figure 1.2 d,e,f).[39]

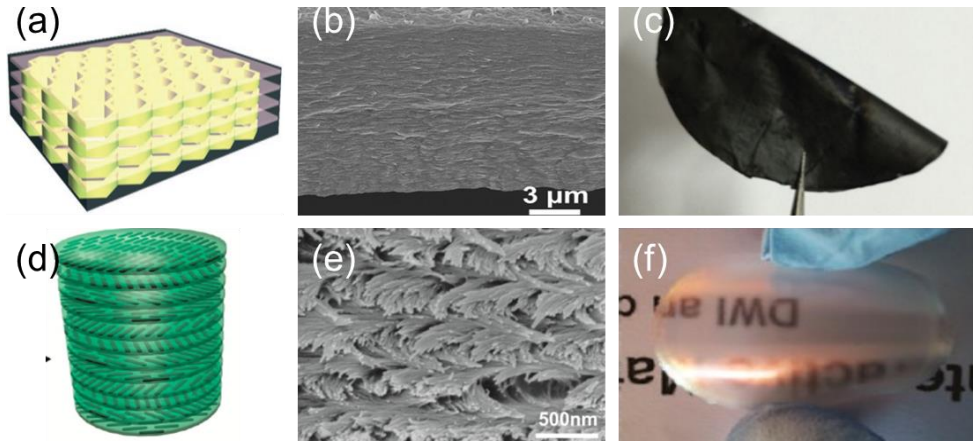

Figure 1.2 Ternary artificial nacre (alumina modified graphene oxide sheet/carboxymethyl cellulose): (a) sketch map of the composite, (b) image exhibiting that the film is well layered inside, (c) the film is free-standing and flexible; and binary artificial nacre (CNCs/PVA): (d) structural model of the composite, (e) image showing that the film is layered with helical pitch, (f) flexible iridescent film.[38,39]

Nacre composites can be prepared using methods such as layer-by-layer (LbL), evaporation, self-assembly, dip-coating or freeze-casting method.[38] The resulting composites demonstrate significant enhancement of their integrated properties (*i.e.* mechanical property), due to the hierarchical structures and enhanced interactions. More recently, some strategies such as ionic cross-linking, covalent cross-linking, and constructing bridges between nanoparticles have been developed for the preparation of tough strong composites. For instance, cellulose nanofibers have been successfully used for the preparation of strong ternary artificial nacre, the sliding effect, crack bridging and crack deflection of the cellulose nanofibers improve the resistance of material deformation.[40] The composites have found the applications in strong tough materials,[41] self-extinguishing composites,[42] and robust electrical devices.[43,44]

Some other structured polymer nanocomposites have also been reported. Mangeney et al. reported polystyrene (PS) microspheres containing γ-Fe_2O_3 superparamagnetic nanoparticles for bioreactivity application.[45] The magnetic nanoparticles were firstly coated with a PS nanoshell and then coated with a polypyrrole nanoshell. It was found that the bioreactivity of the complex nanoparticles was stronger and more stable. Tang et al. reported a electrical conductive composite material – PS microsphere-graphene-carbon nanotube (see Figure 1.3).[46] The self-assembly between PS microspheres and the CNT-graphene oxide sheet mixture offers precise construction of the ordered conductive network. The design presents a super-low nanofiller percolation threshold value (0.03 vol%), which can satisfy applications requiring high transparency and high electrical conductivity. Wang et al. reviewed nanogel composites composed of carbon nanoparticles for bioimaging and drug release.[47] The diversity of polymer manufacturing protocols as well as the species of nanoparticles provides various prominent features and applications of nanocomposites. Continuous research in the field is needed to develop new polymer nanocomposites and to promote the applications of the composites.

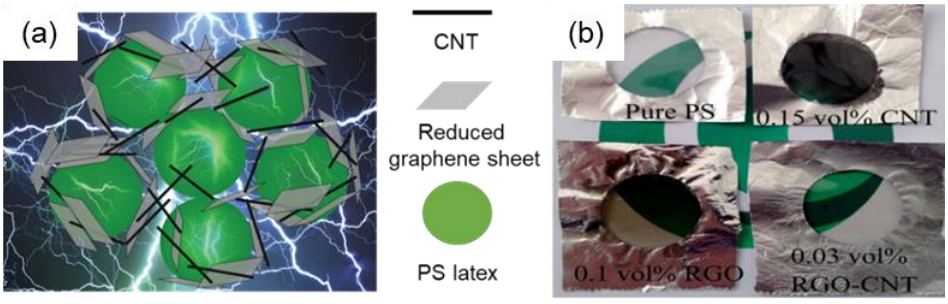

Figure 1.3 (a) Schematic illustration of the PS microsphere-graphene-carbon nanotube composite containing a conducting network; (b) photographs of films with carbon nanofiller contents at percolation threshold.[46]

1.4 Properties of Functional Polymer Nanocomposites

1.4.1 Thermomechanical Properties

The general reinforcing effect of traditional nanoparticles in polymer nanocomposites has been reviewed by Jordan et al and Tjong et al.[48,49] Normally, the elastic modulus increases with the increased content of nanoparticles in the composite; in particular, the smaller nanoparticles show a more impressive effect on the elastic modulus. The glass transition temperature, which is related to the operation temperature of materials, also has positive correlations with the size and their volume fraction of the added nanoparticles. It is also claimed that the properties of nanocomposites are greatly dependent on the nature of nanoparticles, nanoparticle-polymer interactions and the way in which composites are compounded. Unlike neat polymer materials, the interaction between the nanoparticles and polymer in a composite can prevent the propagation of material damage. The nanoparticles act as crack barriers which increase the energy absorption and damage tolerance, the composite will not fracture in short term.[50]

Many examples have demonstrated the influence of nanoparticles on the composite mechanical performance. Ansari et al. investigated the effect of surfactant-modified CNCs on the material mechanical properties of poly(vinyl acetate).[51] They reported that the addition of 5 wt% of CNCs to the polymer matrix yielded significant increases in average modulus (from 0.24 GPa to 1.8 GPa) and average ultimate tensile strength (from 4.6 MPa to 25 MPa). Meanwhile, the glass transition temperature of the composite was ca. 10 °C higher. Polymer nanocomposites of CNC incorporated into polypropylene, polyurethane, poly(ε-caprolactone)

have also been investigated.[52,53] Bozdoğan et al. studied the effect of layered graphene nanosheets on the properties of PVA.[54] Their thermal analysis results showed that the glass transition temperature and the polymer crystallization temperature of the optimal composite increased obviously due to the addition of nanosheets; the Young's modulus and ultimate tensile strength were enhanced by ca. 10-time and ca. 4-time, respectively, with the optimal composite.

In another case, a CNC/PVA composite containing 90 wt% of CNC particles showed ca. 6-time higher Young's modulus and 2-time higher tensile strength, compared to neat PVA.[39] The study demonstrated that polymer nanocomposites containing high fractions of reinforcing fillers could form ordered multiscale structures and exhibit excellent mechanical behavior. Similarly, nanoclay and graphene nanosheets have also been used to fabricate high strength and high toughness composites; the large content of nanoparticles with planar orientation in the composites allows effective load transfer between the nanoparticles and polymer chains.[55,56] To date, developing composites reinforced by nanoparticles is still the research area of strong interest and have led to considerably new composites.[57-60]

1.4.2 Surface Properties

Surface properties can be tuned in the development of polymer nanocomposites. The geometry of the nanoparticles and their surface chemistry are intrinsic factors affecting the surface property of a composite. Distribution of nanoparticles in polymer matrix, their fabrication method and the post-treatment process are also crucial factors to the resulting

surface property of a composite.[2] The surface properties can be designed to accomplish specific applications of composites, such as antibacterial, anti-fouling and self-cleaning, oil/water separation.

Guo et al. reviewed the advances in fabrication of polymer/nanosilver coating material for antibacterial application.[61] Nanosilver is considered as an excellent antibacterial agent, which has a broad-spectrum antibacterial activity. The surface layers of the polymer/nanosilver composite showed a clear inhibition area against various types of bacteria. Composite of silver nanoparticles in a cellulose matrix, which serves as a composite coating material for steel, showed benefits in anti-corrosion.[62] Selim et al. utilized silicone and spherical nano magnetite to prepare composite coating. The coating showed a superhydrophobic characteristics with self-cleaning foul release effect; and the best self-cleaning performance resulted at a low nanoparticle content (ca. 0.5 wt%).[63]

In oil/water separation, the technological focus is on the construction of superior surface wettability, such as superhydrophobic and superhydrophilic characteristics. Previously Laird et al. reported a superhydrophobic behavior of polyethylene/carbon nanotube composite and polytetrafluoroethylene/carbon nanotube composites. Their surface feature can be moderated by tuning the polymer morphology, polymer fractions and the preparation method.[64,65] On the contrary, composites of carbon nanotubes incorporated in polydopamine and polyethyleneimine were reported to have superhydrophilic surface characteristics and highly oleophobic characteristics under water.[66] More recently, Abraham

et. al designed a membrane fabricated with a CNT-based composite, which can be utilize for water or oil collection from environmental pollution (see Figure 1.4).[67]

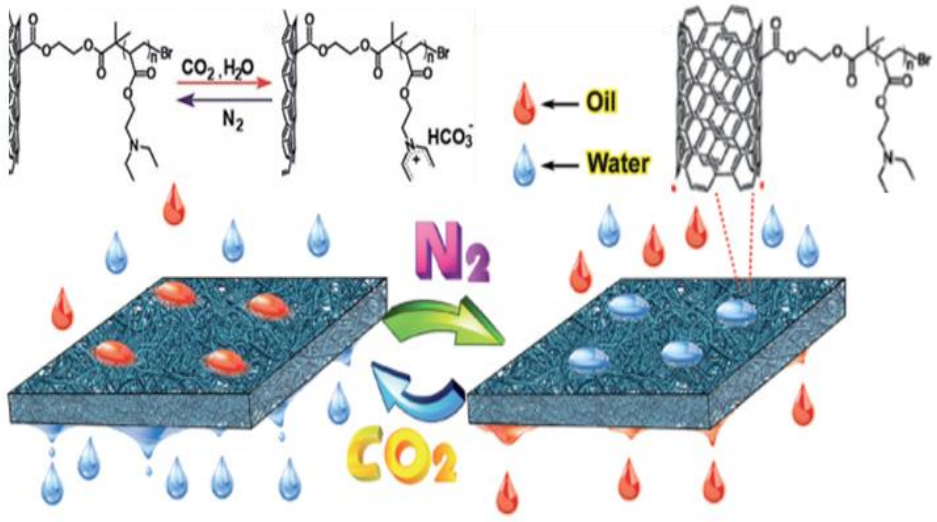

Figure 1.4 Schematic illustration of the surface features of gas-responsive CNTs/polymer composite membrane.[67]

1.4.3 Catalytic Properties

Metal nanoparticles have shown different catalytic behavior for different types of chemical reactions, such as oxidation, selective hydrogenation, coupling reactions, electrocatalytic reactions or photocatalytic reactions. The development of highly effective catalysts is of great significance for modern green chemistry. Traditionally, metal nanoparticles are supported onto the inorganic substrates to avoid the loss in catalytic efficiency caused by aggregation of nanoparticles. Many factors including the particle

geometry, particle size, composite composition, particle-support interaction, and particle-reactant/solvent interaction can have significant influences on the catalytic properties.[7]

In recent years, polymer nanocomposites have been applied as solid catalysts for application in heterogeneous catalytic reactions to address the increasing demand for high-performance catalytic processes. The use of the polymer can control the nanoparticle formation, stabilize the produced nanoparticles and play a role in enhancing the catalytic performance.[25] Some polymer supported metal nanoparticles are featured with outstanding reactivity, excellent recyclability and large-scale applicability. Masing et al. prepared palladium (Pd) nanoparticles supported on an acrylate copolymer for selective hydrogenation reactions, which showed high activity and facile reusability.[31] The Pd-based polymer nanocomposites have also been used in coupling reaction and electrochemical oxidation reaction.[68,69] Kwon et al. demonstrated that the multi-component polymer composite catalyst rendered remarkable catalytic behavior (see Figure 1.5).[70] Under the optimized reaction condition, the coupling between iodobenzene and phenylboronic acid showed excellent high yield (99%); meanwhile, the reactivity was about 16-time higher than the Pd-rGO (without polymer) catalyst. The rate-promoted reaction was attributed to the better accessibility and improved chemical diffusion of reactants facilitated by the polymer. Moreover, the strong interaction between polymer and Pd nanoparticles also endows the catalyst excellent recyclability.

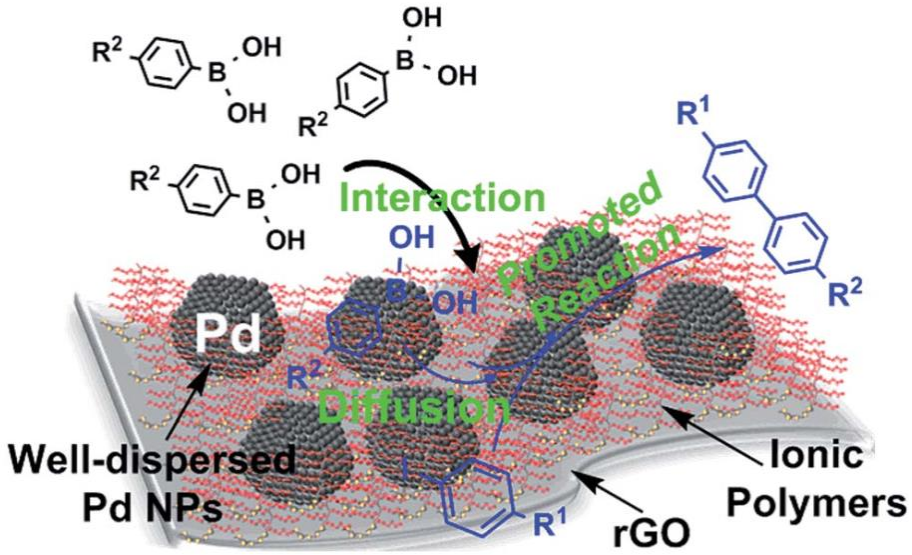

Figure 1.5 Schematic illustration of the role of polymer nanocomposite catalyst in the coupling reaction.[70]

Nanoparticles of cheaper metals such as copper and iron are attractive alternative catalysts for various reactions. Sharma et al. reviewed the catalytic properties iron oxide nanoparticles supported on polymers for different types of coupling reactions.[71] The use of iron oxide nanoparticles for the development of catalytic systems has led to increasing applications as they enable environmentally-friendly and sustainable catalytic processes.[71] An additional example is the heterogeneous catalytic reaction performed over polymer supported copper nanoparticles.[32] With a polymer coating on the surface, the highly active crystal facets of nanoparticles are more stable upon exposure to reaction condition. Moreover, the functionalized polymer could bring novel cooperative catalytic properties.[25]

1.4.4 Optical Properties

The incorporation of nanoparticles in polymer nanocomposites offers the possibility to change the optical properties of the matrix, even at a small number of nanoparticles. Metal nanoparticles have drawn a lot of attention due to their intense plasmon resonance response.[72] Among the many metal nanoparticles, gold nanorod is one of the most studied metal nanoparticles in the field, due to their excellent optical properties and photothermal property. Depending on the intrinsic features of the nanoparticles as well as the particle arrangement on polymer supports, the resulting composites are applicable in medical imaging light filter, optical sensor, and Raman scattering device.[73] Useful optical properties, including UV absorption, light absorption, photoluminescence, can be achieved by compounding polymer and metal oxide nanoparticles. Kango et al. overviewed the optical properties of several synthetic polymer nanocomposites using ZnO, Al_2O_3, ZrO_2, TiO_2 nanoparticles.[20] Another example is the CNC-based polymer nanocomposites; the composite can present iridescence as a function of the composition with respect to polymer contents, if a proper polymer matrix is applied. The feature is attributed to the self-assembly helical structure of the rod shape nanoparticles. Combining CNC particles and polymers increases the mechanical performance and alter the optical properties of the composites.[39]

Besides the mentioned mechanical, surface, catalytic and optical properties, some other properties such as magnetic, dielectric and electrical, barrier properties can also be significantly enhanced through the efficient design of polymer nanocomposite systems.

1.5 Thesis Research Objectives

Despite the tremendous developments in the field of polymer nanocomposites, there is still large room for new advancements. This thesis research is aimed at designing new polymer nanocomposites with the use of nanomaterials including CNCs, CNTs, and Pd nanoparticles, developing novel/improved methods/strategies for nanocomposite synthesis, and demonstrating/exploring their new applications. In specific, in Chapter 2, CNCs are modified with hyperbranched polyethylene ionomers containing quaternary ammonium ions through ionic interactions; modified CNCs are used as the nanofillers to reinforce a hydrophobic ethylene-octene copolymer elastomer. In Chapter 3, CNCs are employed to reinforce sodium alginate for the fabrication of tough strong film materials with the use of materials from sustainable biostocks. In Chapter 4, a new facile in situ catalytic polymerization method is developed to fabricate CNT/polycyclopentene hybrids with the CNTs decorated with polycyclopentene crystals at controllable compositions. These composites have been demonstrated for the direct fabrication of lotus leaf-like superhydrophobic films. In Chapter 5, supported Pd nanocatalysts modified with various ligands are investigated for their catalytic efficiency in the selective hydrogenation of alkynes. The effects of the ligands on the catalytic performance have been elucidated with the optimum ligands demonstrated.

1.6 References

1. Müller, K.; Bugnicourt, E.; Latorre, M.; Jorda, M.; Sanz, Y. Z.; Lagaron, J. M.; Miesbauer, O.; Bianchin, A.; Hankin, S.; Bölz, U.; Pérez, G.; Jesdinszki, M.; Lindner, M.; Scheuerer. Z.; Castelló, S.; Schmid, M. *Nanomaterials*, **2017**, *7*, 74.
2. Hanemann, T.; Szabo, D. V. *Materials*, **2010**, *3*, 3468–3517.
3. Tiwari, J. N.; Tiwari, R. N.; Kim, K. S. *Prog. Mater. Sci.*, **2012**, *57*, 724–803.
4. Srivastava, S.; Kotov, N. A. *Soft Matter*, **2009**, *5*, 1146–1156.
5. Heiligtag, F. J.; Niederberger, M. *Mater. Today*, **2013**, *16*, 262–271.
6. Bhattacharya, M. *Materials*, **2016**, *9*, 262.
7. Liu, L.; Corma, A. *Chem. Rev.*, **2018**, *118*, 4981–5079.
8. Sui, Ruohong, Charpentier, P. *Chem. Rev.*, **2012**, *112*, 3057–3082.
9. Hong, G. S.; Diao, S. O.; Antaris, A. L.; Dai, H. J. *Chem. Rev.*, **2015**, *115*, 10816–10906.
10. Anu, M. E.; Saravanakumar. M. P. *IOP Conf. Ser.: Mater. Sci. Eng.*, **2017**, *263*, 032019.
11. Moon, R. J.; Martini, A.; Nairn, J.; Simonsen, J.; Youngblood, J. *Chem. Soc. Rev.*, **2011**, *40*, 3941–3994.
12. Fischer, H. *Mater. Sci. Eng. C*, **2003**, *23*, 763–772.
13. Usuki, A.; Kojima, Y.; Kawasumi, M.; Okada, A.; Fukushima, Y.; Kurauchi, T.; Kamigaito, O. *J. Mater. Res.*, **1993**, *8*, 1179–1184.
14. Njuguna, J.; Pielichowski, K.; Desai, S. *Polym. Adv. Technol.*, **2008**, *19*, 947–959.
15. Sun, D. Z.; Sue, H. J. *Appl. Phys. Lett.*, **2009**, *94*, 253106.

16. Peres, M.; Costa, L. C.; Neves, A.; Soares, M. J.; Monteiro, T.; Esteves, A. C.; Barros-Timmons, A.; Trindade, T.; Kholkin, A.; Alves, E. *Nanotechnology*, **2005**, *16*, 1969–1973.
17. Koo, J.; Kim, H.; Kim, K. Y.; Jang, Y. R.; Lee, J. S.; Yoon, S. W.; Suh, B. J.; Yu, T.; Bang, J.; Yoon, K.; Yuan, G.; Satija, S. K. *RSC Adv.*, **2016**, *6*, 55842–55847.
18. Kumar, S.; Purohit, R.; Malik, M. M. *Mater. Today: Proc.*, **2015**, *2*, 3704–3711.
19. Alexandre, M.; Dubois, P. *Mater. Sci. Eng.*, **2000**, *28*, 1–63.
20. Kango, S.; Kalia, S.; Celli, A.; Njuguna, J.; Habibi, Y.; Kumar, R. *Prog. Polym. Sci.*, **2013**, *38*, 1232–1261.
21. Guo, Q. C.; Ghadiri, R.; Weigel, T.; Aumann, A.; Gurevich, E. L.; Esen, C.; Medenbach, O.; Cheng, W.; Chichkov, B.; Ostendorf, A. *Polymers*, **2014**, *6*, 2037–2050.
22. Sarkar, S.; Guibal, E.; Quignard, F.; SenGupta, A. K. *J. Nanopart. Res.*, **2012**, *14*, 715.
23. Pomogailo, A. D. *Colloid J.*, **2005**, *67*, 726–747.
24. Gangopadhyay, R.; De, A. *Chem. Mater.*, **2000**, *12*, 608–622.
25. Mahouche-Chergui, S.; Guerrouache, M.; Carbonnier, B.; Chehimi, M. M. *Colloids Surf., A: Physicochem. Eng. Asp.*, **2013**, *439*, 43–68.
26. Georgakilas, V.; Tiwari, J. N.; Kemp, K. C.; Perman, J. A.; Bourlinos, A. B.; Kim, K. S.; Zboril, R. *Chem. Rev.*, **2016**, *116*, 5464–5519.
27. Eyley, S.; Thielemans, W. *Nanoscale*, **2014**, *6*, 7764–7779.
28. Lonkar, S. P.; Deshmukh, Y. S.; Abdala, A. A. *Nano Res.*, **2015**, *8*, 1039–1074.

29. Park, J.; Kadasala, N. R.; Abouelmagd, S. A.; Castanares, M. A.; Collins, D. S.; Wei, A.; Yeo, Y. *Biomaterials*, **2016**, *101*, 285–295.

30. Lin, Y. S.; Wu, S. H.; Hung, Y.; Chou, Y. H.; Chang, C.; Lin, M. L.; Tsai, C. P.; Mou, C. Y. *Chem. Mater.*, **2006**, *18*, 5170–5172.

31. Masing, F.; Wang, X.; Nusse, H.; Klingauf, J.; Studer, A. *Chem. Eur. J.*, **2017**, *23*, 6014–6018.

32. Zuraev, A. V.; Grigoriev, Y. V.; Budevich, V. A.; Ivashkevich, O. A. *Tetrahedron Lett.*, **2018**, *59*, 1583–1586.

33. de Roo, T.; Huber, S.; Mecking, S. *ACS Macro Lett.*, **2016**, *5*, 786–789.

34. He, L.; Karumuri, A.; Mukhopadhyay, S. M. *RSC Adv.*, **2017**, *7*, 25265–26575.

35. Mariani, G.; Wang, Y.; Wong, P. S.; Lech, A.; Hung, C. H.; Shapiro, J.; Prikhodko, S.; El-Kady, M.; Kaner, R. B.; Hufraker, D. L. *Nano Lett.*, **2012**, *12*, 3581–3586.

36. Rim, J. E.; Zavattieri, P.; Juster, A.; Espinosa, H. D. *J. Mech. Behav. Biomed. Mater.*, **2011**, *4*, 190–211.

37. Wan, S.; Li, Y.; Peng, J.; Hu, H.; Cheng, Q.; Jiang, L. *ACS Nano*, **2015**, *9*, 708–714.

38. Zhao, H. W.; Yue, Y. H.; Zhang, Y. W.; Li, L. D.; Guo, L. *Adv. Mater.*, **2016**, *28*, 2037–2042.

39. Wang, B.; Walther, A. *ACS Nano*, **2015**, *9*, 10637–10646

40. Zhao, H. W.; Guo, L. *Adv. Mater.*, **2017**, *29*, 1702903.

41. Malho, J. M.; Laaksonen, P.; Walther, A.; Ikkala, O.; Linder, M. *Biomacromolecules*, **2012**, *13*, 1093–1099.

42. Liu, A. D.; Walther, A.; Ikkala, O.; Belova, L.; Berglund, L. A. *Biomacromolecules*, **2011**, *12*, 633–641.

43. Lee, T.; Min, S. H.; Gu, M.; Jung, Y. K.; Lee, W.; Lee, J. U.; Seong, D. G.; Kim, B. S. *Chem. Mater.*, **2015**, *27*, 3785–3796.

44. Cheng, Q. F.; Wu, M. X.; Li, M. Z.; Jiang, L.; Tang, Z. Y. *Angew. Chem. Int. Ed.*, **2013**, *52*, 3750–3755.

45. Mangeney, C.; Fertani, M.; Bousalem, S.; Zhicai, M.; Ammar, S.; Herbst, F.; Beaunier, P.; Elaissari, A.; Chehimi, M. M. *Langmuir*, **2007**, *23*, 10940–10949.

46. Tang, C. Y.; Long, G. C.; Hu, X.; Wong, K. W.; Lau, W. M.; Fan, M. K.; Mei, J.; Xu, T.; Wang, B.; Hui, D. *Nanoscale*, **2014**, *6*, 7877–7888.

47. Wang, H.; Chen, Q. W.; Zhou, S. Q. *Chem. Soc. Rev.*, **2018**, *47*, 4198–4232.

48. Jordan, J.; Jacob, K. I.; Tannenbaum, R.; Sharaf, M. A.; Jasiuk, I. *Mater. Sci. Eng., A*, **2005**, *393*, 1–11.

49. Tjong, S. C. *Mater. Sci. Eng., R*, **2006**, *53*, 73–197.

50. Eslami-Farsani, R.; Shahrabi-Farahani, A. *Fiber Polym.*, **2017**, *18*, 965–970

51. Ansari, F.; Salajkova, M.; Zhou, Q.; Berglund, L. A. *Biomacromolecules*, **2015**, *16*, 3916–3924.

52. Wohlhauser, S.; Delepierre, G.; Labet, M.; Morandi, G.; Thielemans, W.; Weder, C.; Zoppe, J. O. *Macromolecules*, **2008**, *51*, 6157–6189.

53. Ljungberg, N.; Bonini, C.; Bortolussi, F.; Boisson, C.; Heux, L.; Cavaille, J. Y. *Biomacromolecules*, **2005**, *6*, 2732–2739.

54. Bozdoğan, A.; Aksakal, B.; Şahintürk, U.; Yargı, Ö. *J. Mol. Struct.*, **2018**, *1174*, 133–141.

55. Podsiadlo, P.; Kaushik, A. K.; Arruda, E. M.; Waas, A. M.; Shim, B. S.; Xu, J. D.; Nandivada, H.; Pumplin, B. G.; Lahann, J.; Ramamoorthy, A.; Kotov, N. A. *Science*, **2007**, *318*, 80–83.

56. Tan, Z. B.; Zhang, M.; Li, C.; Yu, S. Y.; Shi, G. Q. *ACS Appl. Mater. Interfaces*, **2015**, *7*, 15010–15016.

57. Salimian, S.; Zadhoush, A.; Mohammadi, A. *J. Reinf. Plast. Compos.*, **2018**, *37*, 441–459.

58. Salimian, S.; Zadhoush, A.; Mohammadi, A. *J. Reinf. Plast. Compos.*, **2018**, *37*, 738–769.

59. Zhang, C. Y.; Wang, J. C. *Materials*, **2018**, *11*, 41.

60. Yurddaskal, M.; Celik, E. *Compos. Struct.*, **2018**, *183*, 381–388.

61. Guo, L. Y.; Yuan, W. Y.; Lu, Z. S.; Li, C. M. *Colloids Surf., A: Physicochem. Eng. Asp.*, **2013**, *439*, 69–83.

62. Solomon, M. M.; Gerengi, H.; Umoren, S. A. *ACS Appl. Mater. Interfaces*, **2017**, *9*, 6376–6389.

63. Selim, M. S.; Elmarakbi, A.; Azzam, A. M.; Shenashen, M. A.; EL-Saeed, A. M.; El-Safty, S. A. *Prog. Org. Coat.*, **2018**, *116*, 21–34.

64. Laird, E. D.; Bose, R. K.; Qi, H.; Lau, K. K. S.; Li, C. Y. *ACS Appl. Mater. Interfaces*, **2013**, *5*, 12089–12098.

65. Laird, E. D.; Wang, W. D.; Cheng, S.; Li, B.; Presser, V.; Dyatkin, B.; Gogotsi, Y.; Li, C. Y. *ACS Nano*, **2012**, *6*, 1204–1213.

66. Gao, S. J.; Zhu, Y. Z.; Zhang, F.; Jin, J. *J. Mater. Chem. A*, **2015**, *3*, 2895–2902.

67. Abraham, S.; Kumaran, S. K.; Montemagno, C. D. *RSC Adv.*, **2017**, *7*, 39465–39470.

68. Siwal, S.; Matseke, S.; Mpelane, S.; Hooda, N.; Nandi, D.; Mallick, K. *Int. J. Hydrogen Energy*, **2017**, *42*, 23599–23605.

69. Wang, M.; Xue, H.; Ju, F.; Yang, H. *Sci Rep.*, **2017**, *7*, 7006.

70. Kwon, T. H.; Cho, K. Y.; Baek, K. Y.; Yoon, H. G.; Kim, B. M. *RSC Adv.*, **2017**, *7*, 11684–11690.

71. Sharma, R. K.; Dutta, S.; Sharma, S.; Zboril, R.; Varma, R. S.; Gawande, M. B. *Green Chem.*, **2016**, *18*, 3184–3209.

72. Srivastava, S.; Haridas, M.; Basu, J. K. *Bull. Mater. Sci.*, **2008**, *31*, 213–217.

73. Jiang, G. Q.; Hore, M. J. A.; Gam, S.; Composto, R. J. *ACS Nano*, **2012**, *6*, 1578–1588.

Chapter 2

Modification of Cellulose Nanocrystals with Quaternary Ammonium-Containing Hyperbranched Polyethylene Ionomers by Ionic Assembly

This chapter is adapted from a paper published by L. Huang, Z. Ye and R. Berry (ACS Sustainable Chem. Eng., 2016, 4, 4937–4950).

Abstract

This chapter reports the first surface modification of cellulose nanocrystals (CNCs) with quaternary ammonium-containing ionomers by ionic binding of their positively charged ammonium ions onto the negatively charged surface of CNCs. A range of hyperbranched polyethylene ionomers (I1–I6) having different ionic content (0.2–2.3 mol%) has been designed and employed for this purpose. The simple dropwise addition and mixing of the aqueous dispersion of CNCs with the ionomer solution in tetrahydrofuran (THF) conveniently renders the ionomer-modified CNCs (mCNC1–mCNC6). The presence of adsorbed ionomers on the modified CNCs is confirmed with spectroscopic and X-ray diffraction evidence, and quantified through thermogravimetric analysis. The effects of the ionomer to CNC feed mass ratio and the ionomers of different ionic content on the modification have been examined. A study on the morphology of the modified CNCs by Atomic force microscopy discloses the occurrence of side-to-side and/or end-to-end assembly of the CNC nanorods due to the "cross-linking" or bridging effects of the multidentate ionomers. Because of the hydrophobic hyperbranched polyethylene segments in the adsorbed ionomers, the modified CNCs can be dispersed in nonpolar or low-polarity organic solvents (such as THF, toluene, and chloroform). In particular, the THF dispersions of modified CNCs

prepared with ionomers having ionic content ≥ 0.7 mol% (I3–I6) behave as thixotropic organo-gels at concentrations ≥ 40 mg·mL^{-1}. Further, the modified CNCs better disperse than unmodified CNCs in a hydrophobic ethylene-octene copolymer (EOC) elastomer matrix and show better thermal stability than a surfactant-modified CNC sample. Tensile testing confirms that the EOC composites, filled with the ionomer-modified CNCs, are significantly reinforced with a tensile modulus nearly doubled that of neat EOC, and better elongation at break relative to those filled with unmodified CNCs or surfactant-modified CNCs.

2.1 Introduction

Cellulose nanocrystals (CNCs) extracted from abundant and renewable biosources have been receiving extensive attention.[1-6] Having a rod-like shape with generally a diameter between 5 and 15 nm and a length between 100 and 300 nm, CNCs have high elastic moduli (over 100 GPa), high specific surface area (several hundred m^2/g), and a reactive surface while being low density.[7] As such, they have been widely investigated, since the first demonstration in 1995,[8] as the reinforcing bionanofillers for the construction of polymer nanocomposites with significantly enhanced mechanical properties.[9-11]

CNCs are generally produced as stable aqueous dispersions often by sulfuric acid hydrolysis of cellulose fibers. Their surface is highly polar and negatively charged due to the presence of sulfate groups resulting from sulfuric acid hydrolysis.[1-6] Most applications of CNCs have thus focused on the aqueous systems by mixing aqueous CNC dispersions with various compatible water-soluble or water-dispersible components (such as water-soluble

monomers and polymers,[12-21] water-dispersible nanoparticles[22-24] and latexes,[25-29] etc.) to obtain functional composite materials. In particular, water-soluble hydrophilic polymers or water-dispersible latexes, including poly(vinyl alcohol),[17,18] poly(ethylene oxide),[19,20] poly(furfuryl alcohol),[21] latexes of poly(styrene-co-butyl acrylate), poly(styrene-co-butadiene), and polybutadiene,[26-29] etc., have been employed as the compatible polymer matrices for the construction of CNC-reinforced polymer nanocomposites by solution mixing. CNCs can be well dispersed in these polar polymer matrices, which maximizes the reinforcement. However, without proper surface modification, the dispersion of CNCs in nonpolar solvents or hydrophobic polymers, such as polyolefins which are produced in the largest volume, are poor.[1-5,9-11,30,31]

To broaden their application scope, surface modification of CNCs through both covalent and noncovalent approaches has been attempted to modify their surface properties so as to render them dispersible in organic solvents (particularly, nonpolar and low-polarity solvents) and hydrophobic polymer matrices.[1-5,9-11,30,31] In the covalent approaches, desired organic groups are directly attached onto the surface of CNCs through the hydroxyl groups present on their surface. Various polymers have also been covalently grafted onto the surface of CNCs through both graft-from[32-34] and graft-to strategies.[35-37] Though highly effective, these covalent surface modification methods often involve tedious and delicate reaction/polymerization chemistry and are inconvenient. In the noncovalent approaches, CNCs are often modified with surfactants through their adsorption via noncovalent electrostatic attraction, hydrophilic affinity, hydrogen bonding, or van der Waals interactions.[30,31] Thus far, various surfactants (anionic, cationic, and nonionic),[32,38-44] as well

as specifically designed block polymers,[25,45] have been employed, rendering the modified CNCs with good dispersibility in desired nonpolar organic solvent or polymer matrices. Relative to covalent ones, these noncovalent approaches are more convenient and easier to implement. However, the amount of surfactant required to cover CNCs is often high, along with the highly possible desorption of the adsorbed surfactant given the involvement of only weak monodentate noncovalent interactions, which could undermine the properties of the resulting composites.[11,40]

In this chapter, the convenient noncovalent surface modification of CNCs with the use of a range of quaternary ammonium-containing hyperbranched polyethylene ionomers is demonstrated. Ionomers are polymers containing a small fraction of ionic functional groups (typically less than 10 mol%) that are covalently bonded to the polymer backbone as pendant groups. Designed with positively charged quaternary ammonium ions tethered onto the nonpolar hyperbranched polyethylene skeleton, these ionomers have been found to bind to the negatively charged surface of CNCs through multidentate ionic interactions, rendering modified CNCs as self-assembled CNC/ionomer composites. The modified CNCs have been thoroughly characterized with various techniques for their compositional, structural, thermal, and morphological features. They have also been investigated for their dispersion in various nonpolar or low-polarity organic solvents and a commercial hydrophobic ethylene-octene copolymer (EOC) matrix. The dispersions have been systematically characterized, with the enhanced dispersibility of the modified CNCs in these media and improved properties demonstrated. Though various quaternary ammonium-containing surfactants[42-44] or polyelectrolytes[25,46,47] have been previously employed for the modification of CNCs, this is

the first report on the use of quaternary ammonium-containing ionomers with a hydrophobic skeleton for rendering modified CNCs.

2.2 Experimental Section

2.2.1 Materials

An aqueous dispersion of CNCs (concentration: 21 mg·mL^{-1}; the average length and average diameter are ~150 nm and ~5 nm) prepared by sulfuric acid hydrolysis of bleached softwood kraft was obtained from CelluForce (Canada) and was subjected to purification by dialysis with deionized water. The Pd–diimine catalyst, [(ArN=C(Me)−(Me)C=NAr)Pd(CH_3)(N≡CMe)]$^+SbF_6^-$ (Ar = 2,6-(iPr)$_2C_6H_3$), was synthesized according to the literature procedure.[48] The acrylate-type ionic liquid comonomer, [2-(acryloyloxy)ethyl]trimethylammonium tetrafluoroborate (AETMA$^+BF_4^-$) was prepared from [2-(acryloyloxy)ethyl]trimethylammonium chloride (80 wt% aqueous solution, Aldrich) via anion exchange with $NaBF_4$ (Aldrich) by following a procedure reported in an earlier paper.[49] Ethylene cylinder (polymer grade) was obtained from Praxair Canada and was purified by passing through purification columns. Acetone (certified ACS grade, Fisher Scientific) was dehydrated with molecular sieves before use. The EOC used herein as the polymer matrix for the compounding of polymer nanocomposites is Engage 8130 obtained from Dow Chemical, which is an ethylene-octene copolymer with the octene comonomer content of 42 wt%. It has a density of 0.864 g·cm^{-3}, a melt flow index of 13 g·min^{-1} (at 190 ºC). Cetyltrimethylammonium bromide (CTAB, ≥ 98%) was obtained from Aldrich. All other

reagents or solvents were obtained from either Aldrich or Fisher Scientific and were used as received.

2.2.2 Synthesis of Hyperbranched Polyethylene Ionomers

The hyperbranched polyethylene ionomers (I1–I6) were synthesized by direct copolymerization of ethylene with ionic liquid comonomer $AETMA^{+}BF_4^{-}$ by following the procedure reported in an earlier paper.[49] The polymerization reactions were all carried out in a 50 mL Schlenk flask equipped with a magnetic stirrer. The flask sealed with a rubber septum was first flame-dried under vacuum. After being cooled down to room temperature, the reactor was purged with ethylene for at least three times, and then filled with ethylene to 1 atm (absolute pressure). A solution of the ionic liquid comonomer (0.245–2.45 g in 5 mL of dry acetone) was then injected into the reactor. Subsequently, the polymerization was started upon the injection of the Pd–diimine catalyst solution (0.08 g, 0.1 mmol in 5 mL of dry acetone). During the polymerization, ethylene pressure was maintained constant by continuous feed from a cylinder and the polymerization temperature was maintained at room temperature with a water bath. After 24 h, the polymerization was stopped by shutting down the ethylene supply and venting the reactor. The black product containing Pd(0) particles resulting from the decomposition of the Pd–diimine catalyst was precipitated out with a large amount of methanol. The precipitate was redissolved in a small amount of THF for multiple washings with methanol. The polymer precipitate was purified to remove Pd black and then dried under vacuum at room temperature, rendering ionomers.[49] As per ^{1}H NMR

spectroscopy, the resulting ionomers (I1–I6) contain quaternary ammonium ion content of 0.2, 0.4, 0.7, 1.1, 1.5, and 2.3 mol%, respectively.

2.2.3 Preparation of Ionomer-Modified CNCs

Typically, the hyperbranched polyethylene ionomer (5–40 mg) was dissolved in THF (40 mL). Under ultrasonication, the aqueous CNC dispersion (10 mg in 0.5 mL) was added dropwise into the ionomer solution. The resulting dispersion was further ultrasonicated for ca. 15 min and was then vacuum-filtered on a PTFE membrane (0.22 μm pore size). The filter cake was thoroughly washed with fresh THF, then dried under vacuum at ca. 50 ºC to render the modified CNCs.

2.2.4 Preparation of CTAB-Modified CNCs

CTAB-modified CNCs were prepared by following a literature procedure[44] with minor modifications. The original CNC aqueous dispersion was diluted to a concentration of 5 $mg \cdot mL^{-1}$, with the adjustment of its pH to 10 by the addition of a NaOH solution. Subsequently, the CNC dispersion (120 mL) was added dropwise into an aqueous CTAB solution (120 mL at 5 $mg \cdot mL^{-1}$) at 60 ºC under vigorous stirring. The mixture was continuously stirred at 60 ºC for 3 h, and then stirred overnight at room temperature. Afterwards, unbound CTAB was removed by dialysis with about 20 water changes. Freeze-drying of the resulting dispersion rendered the CTAB-modified CNCs (610 mg), termed as

CTAB-CNC. The CTAB content in CTAB-CNC was 15 wt% (as per thermogravimetric analysis).

2.2.5 Preparation of EOC Composites

The EOC composites were prepared by a solution mixing method. A prescribed quantity of modified CNCs (equivalent to 10 wt% of neat CNCs in composites) was dispersed at 10 $mg \cdot mL^{-1}$ in toluene by ultrasonication for 24 h. In the case with original unmodified CNCs, freeze-dried CNCs were dispersed in THF at 10 $mg \cdot mL^{-1}$. The dispersion was added dropwise into a toluene solution of EOC (50 $mg \cdot mL^{-1}$) within 1 h under magnetic stirring. The mixture was continuously stirred for 3 h before precipitation in a large amount of methanol. The precipitate was dried at 120 ºC in a vacuum oven for 24 h.

2.2.6 Characterizations and Measurements

^1H NMR spectra of the ionomers were all collected on a Varian Gemini 2000 spectrometer (200 MHz) with $CDCl_3$ as the solvent. Average molecular weights and dilute solution properties of the ionomers were measured with a triple-detection gel permeation chromatography (GPC) equipped with a three-angle light scattering detector, a refractive index concentration detector, and a viscosity detector in THF at 33 ºC. Please refer to an earlier paper.[49] Fourier-transform infrared (FTIR) spectra were obtained on a Thermo Scientific Nicolet 6700 Analytical FTIR spectrometer. The samples were prepared as pellets

using spectroscopic-grade KBr. Thermogravimetric analysis (TGA) was carried out on a TA Instruments Q50 thermogravimetric analyzer. Measurements were performed in a N_2 atmosphere with a continuous flow of 60 mL·min^{-1} through the sample furnace and a flow of 40 mL·min^{-1} through the balance compartment. In a typical measurement, the sample (ca. 5 to 10 mg) was heated from 30 to 800 ºC at 10 ºC·min^{-1}. Differential scanning calorimetry (DSC) measurements were performed on a TA Instruments Q100 DSC equipped with a refrigerated cooling system (RCS) under a N_2 atmosphere at a flow of 50 mL·min^{-1}. The instrument was operated in the standard DSC mode and was calibrated with an indium standard. Samples (ca. 8 mg) were heated from 40 to 170 ºC at 10 ºC·min^{-1}, held at 170 ºC for 3 min, and cooled to –90 ºC at 10 ºC·min^{-1}, followed with a heating ramp from –90 to 170 ºC at 10 ºC·min^{-1}.

Dynamic light scattering (DLS) measurements of the dilute dispersions (ca. 0.1 mg·mL^{-1}) of the various CNC samples for their hydrodynamic particle size and ζ potential were performed on a Brookhaven NanoBrook Omni Instrument at 25 ºC. Wide-angle X-ray diffraction patterns of the ionomer and CNC samples were recorded on an X'Pert Pro diffractometer with Cu Kα radiation (wavelength 1.54 Å) at room temperature. Atomic force microscopy (AFM) imaging of the various CNC samples was performed on a Bruker multimode AFM in the tapping mode with a phosphorous-doped silicon tip having a force constant of 20–80 N·m^{-1}. AFM samples were prepared by placing a freshly cleaved mica piece in the dilute dispersion (ca. 0.1 mg·mL^{-1}) of the corresponding CNC sample overnight for sample deposition, which was then taken out and dried for the imaging.

Rheological characterizations of the organo-gels of modified CNCs in THF were performed on a TA Instruments AR-G2 rheometer through both small amplitude dynamic oscillation and steady shear measurements with a cone-plate geometry (2º in cone angle and 40 mm in diameter). One measurement was performed for each organo-gel. To avoid evaporation of THF, the measurements were all undertaken at 10 ºC, which was maintained with a Pelletier plate temperature controlling system, along with the use of a solvent trap to minimize THF evaporation. For the dynamic oscillation measurements, the following procedure was used. A rotational pre-shear rate at 50 s^{-1} was first performed to destroy the gel network structure. Then a dynamic oscillation frequency scan from 0.01 to 100 Hz was undertaken at a high strain of 100%. After resting for 15 min for the rebuilding of the gel network, the second dynamic oscillation frequency scan from 0.01 to 100 Hz was performed at a low strain of 0.01%. The steady shear measurements were done by increasing the shear rate from 0.0001 to 200 s^{-1}, followed with the decrease of shear rate from 200 to 0.0001 s^{-1}. Prior to each steady shear measurement, the sample was equilibrated for 15 min for the formation of the gel network.

Rheological characterizations of EOC and its various composites were performed on the same instrument with a 20 mm parallel plate geometry at a gap of 1 mm. The measurements were all carried out in the small amplitude dynamic oscillation mode at the strain of 0.1% within a frequency range of 0.01−100 Hz at 190 ºC. The temperature was maintained within ± 0.1 ºC with the electrically heated plate system and the measurements were done under N_2 protection. Rheology sample discs were prepared by compression molding in a Carver press at approximately 135 ºC for 1 min.

Tensile properties of nanocomposites were examined using an Instron 5943 universal tester equipped with a 1 KN load cell. All experiments were carried out with a crosshead speed of 500 mm·min^{-1}. Type VI (ASTM D638) dog-bone shaped samples were cut from a sheet with an average thickness of 2.7 mm with a die. The sheets were prepared by compression molding in a Carver press at approximately 135 ºC for 1 min. Three repeat trials were performed for most specimens with two repeats for composites made in lower quantity and the average is reported.

2.3 Results and Discussion

2.3.1 Synthesis of Hyperbranched Polyethylene Ionomers

The hyperbranched polyethylene ionomers (I1–I6) containing the tetralkylammonium ions at different content were synthesized herein by Pd–diimine-catalyzed direct copolymerization of ethylene with AETMA$^+$BF$_4^-$ as the ionic liquid comonomer (see Scheme 2.1). It was recently discovered this direct copolymerization strategy for convenient synthesis of quaternary ammonium-containing polyethylene ionomers and elucidated the structures and physical properties of these ionomers.[49] Table 2.1 summarizes the copolymerization conditions and detailed characterization results (including composition, branching structure, molecular weight, and dilute solution properties) of the ionomers. Figure 2.1 shows their ^{1}H NMR spectra, which confirm their possession of the covalently tethered quaternary ammonium ions and the highly branched polyethylene skeleton.

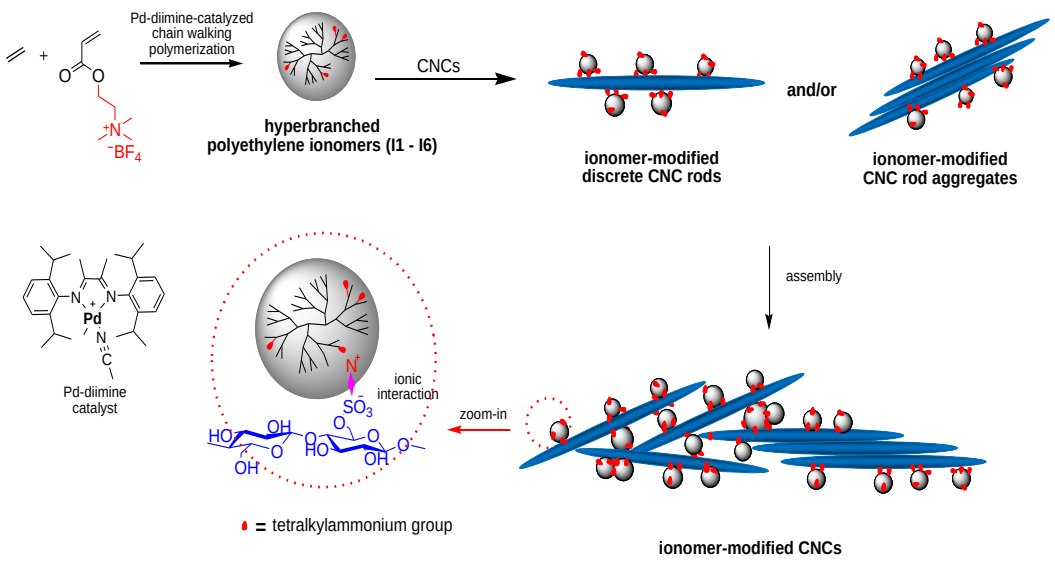

Scheme 2.1 Schematically illustrate the synthesis of hyperbranched polyethylene ionomers, the modification for CNC particles, and the modified assemblies.

Changing the feed concentration of $AETMA^{+}BF_4^{-}$ in the polymerization allows the convenient tuning of its content (*i.e.*, quaternary ammonium content; 0.2, 0.4, 0.7, 1.1, 1.5, and 2.3 mol% for I1–I6, respectively; see Table 2.1) in the ionomers.[49] In consequence, the average molecular weight (see Table 2.1) of the ionomers generally decreases with the increase of the quaternary ammonium content.[49] The quaternary ammonium ions are randomly distributed in the ionomer chains given the statistical Pd–diimine-catalyzed ethylene-acrylate copolymerization mechanism,[50,51] with each ionomer chain containing multiple ions on average. As per their low intrinsic viscosity (see Table 2.1), the polyethylene skeleton of these ionomers features a spherical dendrimer-like, highly compact hyperbranched chain architecture, resulting from the well-known chain walking mechanism of the Pd–diimine catalyst.[50,51] This hyperbranched architecture is beneficial since it

completely disrupts the formation of polyethylene crystals and thus renders the ionomers with good dispersibility/solubility in nonpolar/low-polarity solvents (such as THF, toluene, chloroform, etc.), which facilitates the subsequent surface modification of CNCs through solution mixing. In the solvents, the ionomers form three-dimensional physical cross-linking networks due to the aggregation of the quaternary ammonium ions.[49] DLS characterization of I4 as a representative ionomer in THF shows a large Z-average hydrodynamic size of ca. 280 nm with a very broad size distribution (ranging from ca. 10 nm to 10,000 nm with a high polydispersity index, PDI = 0.56) and a ζ potential of ca. 10 mV. The large size and broad distribution provide the evidence supporting the presence ionic aggregation.

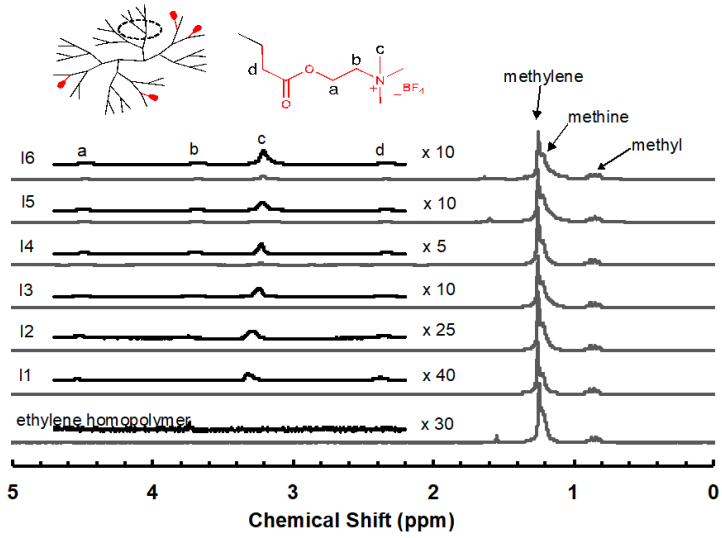

Figure 2.1 ^{1}H NMR spectra of the quaternary ammonium-containing hyperbranched polyethylene ionomers (I1–I6) and a nonionic hyperbranched ethylene homopolymer.

Table 2.1 Synthesis and characterization of the quaternary ammonium-containing hyperbranched polyethylene ionomers (I1–I6).

Ionomer[a]	Catalyst (mmol)	Comonomer[b] (mol/L)	Yield (g)	C_2H_4 TOF[c] (1/h)	Comonomer content[d] (mol%)	Branch density[e] (1/1000 C)	GPC results of hydrolyzed samples[f]				
							M_w (kg/mol)	PDI	$[\eta]_w$ (mL/g)	K (mL/g)	α
I1	0.1	0.10	1.20	17.9	0.2	92	18	1.7	9.5	0.55	0.30
I2	0.3	0.14	2.85	14.1	0.4	92	16	1.4	10.2	0.31	0.37
I3	0.1	0.20	1.40	20.8	0.7	85	18	1.3	10.2	0.20	0.41
I4	0.3	0.36	1.85	9.2	1.1	90	29	1.5	11.5	0.29	0.36
I5	0.1	0.50	0.82	12.2	1.5	88	15	1.3	10.1	0.17	0.43
I6	0.1	1.00	0.19	2.8	2.3	92	9	1.4	8.4	0.26	0.39

[a] Polymerizations were all conducted under 1 atm ethylene pressure in 10 mL acetone as solvent at room temperature for 24 h. [b] Feed concentration of ionic liquid comonomer, $AETMA^+BF_4^-$. [c] Ethylene turnover frequency (TOF) calculated as $\frac{\frac{m_{yield}\,(g)}{24\,(h)\times 28\left(\frac{g}{mol}\right)}}{n_{catalyst}\,(mol)}$. [d] Content of quaternary ammonium ion in ionomers, determined with ^{1}H NMR spectroscopy as $100\% \times 4I_1/9I_2$, where I_1 represents the integration area for methyl protons on the ammonium ion (ca. 3.25 ppm) and I_2 represents peak integration area for protons on ethylene sequences (0.7–1.5 ppm). [e] Branch density determined with ^{1}H NMR as $1000 \times 2I_3/3I_2$, where I_3 represents the integration area for methyl protons in ethylene sequences (0.7–1.0 ppm). [f] Weight-average molecular weight (M_w) and polydispersity index (PDI) were determined with the light scattering detector in the characterization of hydrolyzed ionomers with triple-detection GPC; weight-average intrinsic viscosity ($[\eta]_w$), Mark-Houwink-Sakurada parameters (K, α) were measured with the viscosity detector in triple detection GPC.

Herein, surface modification of CNCs with the ionomers is conveniently achieved by the simple dropwise addition of an aqueous CNC dispersion (21 $mg \cdot mL^{-1}$) into a dilute solution of each ionomer in THF at desired concentrations under ultrasonication. In this procedure, the volume ratio of the aqueous CNC dispersion to the THF ionomer solution was made low, 1:80, to prevent the undesired precipitation of the ionomers upon the addition of excess water. During the dropwise addition of the CNC solution, the mixture became cloudy initially, followed with the gradual formation of fluffy white precipitates. The phenomenon is drastically different from the control experiment by dropping CNC solution into pure THF without containing ionomers, where visible large aggregates immediately formed. This difference clearly indicates the effect of the ionomers. The resulting mixture was vacuum-filtered; the solids were thoroughly washed with excess fresh THF to remove unused ionomers and then dried, rendering the modified CNCs as white solid powders. Through this procedure, it was found that a nearly quantitative retention of the feed CNCs was achieved in all cases. In the case with I3 as the modifying ionomer, the effect of the feed mass ratio of ionomer to CNC [$(m_{ionomer}/m_{CNC})_0$, in the broad range of 0.5 to 4] on the modification was investigated by changing the concentration of the ionomer solution while with a fixed weight of CNCs. With the other ionomers, the $(m_{ionomer}/m_{CNC})_0$ ratio was set at 2 to investigate the effect of ionic content of the ionomer on the modification. The resulting modified ionomers are termed as mCNC# (*i.e.*, mCNC1 to mCNC6) with the number denoting the corresponding ionomers (I1 to I6), or mCNC3-# (*i.e.*, mCNC3-1 to mCNC3-4) for those modified with I3 at different $(m_{ionomer}/m_{CNC})_0$ ratios. Table 2.2 summarizes the characterizations of these modified CNCs.

Figure 2.2 shows the FTIR spectrum of a representative modified CNC sample, mCNC4, as well as the spectra of the corresponding ionomer (I4) and dried original unmodified CNCs for comparison. I4 shows two characteristic bands at 1737 and 1460 cm^{-1}, respectively. They correspond respectively to the C=O stretching frequency of the carbonyl group and the trimethyl groups of the quaternary ammonium in the incorporated $AETMA^{+}BF_4^{-}$ units in the ionomer.[42] These two bands are absent in the unmodified CNCs but are clearly present in mCNC4, thus confirming qualitatively the presence of the adsorbed ionomer in the modified CNC sample.

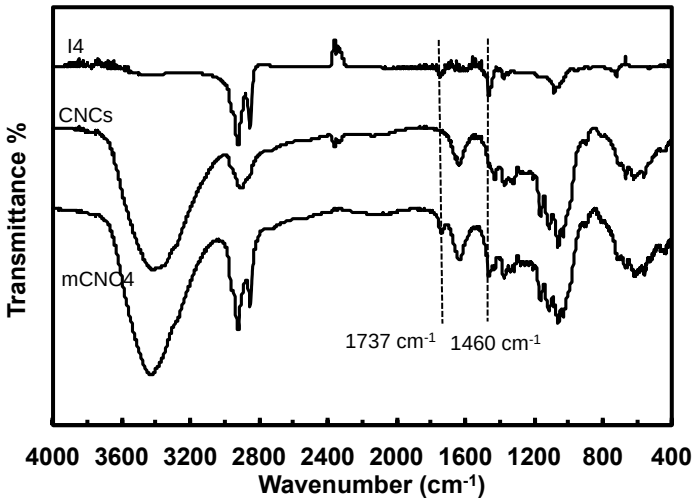

Figure 2.2 FTIR spectra of I4, dried original unmodified CNCs, and I4-modified mCNC4.

TGA characterization was performed on the modified CNCs to evaluate their thermal behavior and quantify their ionomer content. Figure 2.3(a) shows the TGA curves of the I3-modified CNCs obtained at various $(m_{ionomer}/m_{CNC})_0$ ratios, along with those of I3 and dried unmodified CNCs for comparison. I3 starts decomposition at around 350 ºC with the nearly complete weight loss at 500 ºC (char yield of 0.5% at 500 ºC). Nearly identical TGA curves

were observed with the other ionomers. Dried unmodified CNCs start decomposition at about 220 ºC and exhibit a drastic 63% weight loss within 220–330 ºC followed with a gradual weight loss upon the further temperature increase (with an additional weight loss of 16% within 320–500 ºC), which is typical of sulfonated CNCs.[52,53] All the I3-modified CNCs exhibit a well-separated two-step weight loss, with the first step within 220–330 ºC (ΔW_1) attributable solely to the decomposition of CNCs and the second step within 330–500 ºC (ΔW_2) resulting from the degradation of both CNCs and the ionomer.

The mass content of the ionomer in the modified CNCs has thus been quantified from ΔW_1 and are summarized in Table 2.2. Figure 2.3(b) plots the dependence of the mass content of I3 in the I3-modified CNCs on the $(m_{ionomer}/m_{CNC})_0$ ratio. Increasing the $(m_{ionomer}/m_{CNC})_0$ ratio from 0.5 to 4 leads to a significant increase in the mass content of I3 from 8 to 35 wt%. This indicates the amount of adsorbed ionomer increases with its feed concentration. However, the increase in the ionomer mass content is much more significant within the $(m_{ionomer}/m_{CNC})_0$ ratio of 0.5–2. As such, the modification with the other ionomers was all undertaken at the $(m_{ionomer}/m_{CNC})_0$ ratio of 2.

Table 2.2 Characterization of the modified CNCs prepared with different ionomers.

Modified CNCs	Ionomer	$(m_{ionomer}/m_{CNC})_0$ [a]	TGA results				DLS results [e]		
			ΔW_1 [b] (%)	ΔW_2 [b] (%)	$T_{d,max}$ [c] (ºC)	Ionomer content [d] (wt%)	d_p (nm)	PDI	ζ potential (mV)
CNCs	N/A	0	63	16	311	0	91	0.3	-27
mCNC1	I1	2	58	32	311	8			
mCNC2	I2	2	51	38	311	19	401	0.39	-15
mCNC3-1	I3	0.5	58	34	314	8			
mCNC3-2	I3	1	52	41	314	17	273	0.37	17
mCNC3-3	I3	2	46	47	321	27	332	0.41	17
mCNC3-4	I3	4	41	50	323	35	255	0.39	22
mCNC4	I4	2	43	46	326	32	265	0.36	20
mCNC5	I5	2	46	44	320	27	552	0.56	22
mCNC6	I6	2	45	42	320	29	287	0.34	30

[a] Feed mass ratio of ionomer to CNC employed in the preparation of modified CNCs. [b] ΔW_1: percentage weight loss within the temperature range of 220–330 ºC; ΔW_2: percentage weight loss within the temperature range of 330–500 ºC. [c] Peak CNC-decomposition temperature. [d] Percentage ionomer mass content in the modified CNCs calculated according to: $Percentage\ of\ ionomer = 100 - \Delta W_1/0.63$. [e] Z-average hydrodynamic particle size (d_p), polydispersity index (PDI) for size distribution, and ζ potential determined by DLS from dilute dispersions in water (for original unmodified CNCs) or THF (for ionomer-modified CNCs).

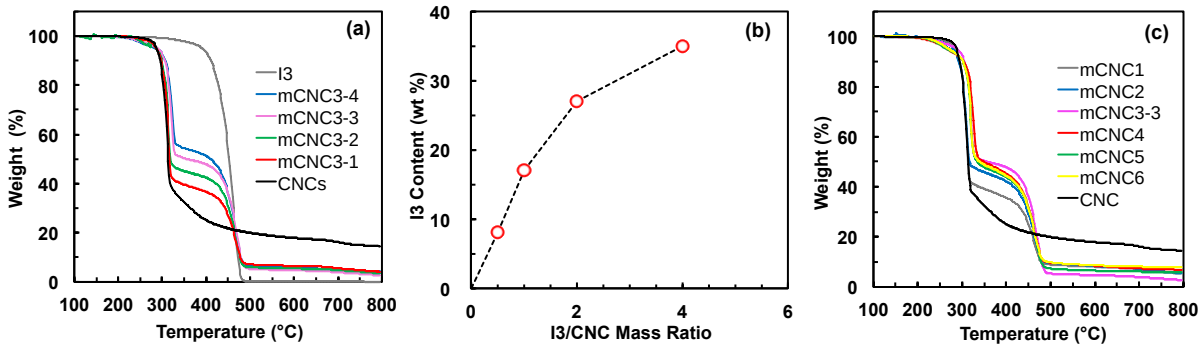

Figure 2.3 (a) TGA curves of I3, dried unmodified CNCs, and CNCs modified with I3 (mCNC3-1 to mCNC3-4) at different ionomer/CNC mass ratios; (b) effect of I3/CNC mass ratio on the content of I3 in the mCNC3 set of modified CNCs; (c) TGA curves of various modified CNCs prepared at the mass ratio of 2, along with that of unmodified CNCs for comparison.

Similar two-step TGA curves (see Figure 2.3(c)) were found with modified CNCs prepared with the other ionomers at the same $(m_{ionomer}/m_{CNC})_0$ ratio of 2. Except mCNC1 and mCNC2 having lower ionomer content of 8 and 19 wt%, respectively, the other modified CNCs all have similar ionomer content within 27–32 wt%. This indicates that increasing the content of the quaternary ammonium ions in the ionomers from 0.2 (in I1) to 0.7 mol% (in I3) leads to the enhanced ionomer adsorption due to the increased binding sites for ionic complexation with CNCs. However, this effect levels off with the further increase in the ionic content in the ionomers from I3 to I6.

In addition, the ionomer modification is found to slightly improve the thermal stability of CNCs. Except mCNC1 and mCNC2, the peak CNC-decomposition temperature of most modified CNCs ($T_{d,max}$, see Table 2.2) in the first step is generally slightly higher (314−326 ºC) than that of dried unmodified CNCs (311 ºC). With the mCNC3 set of modified samples (mCNC3-1 to mCNC3-4), one can find the increasing trend of $T_{d,max}$ (from 314 to 323 ºC) with increase of the ionomer content from mCNC3-1 to mCNC3-4. These results indicate that the adsorbed ionomers on the surface of modified CNCs can serve as a protecting coating layer enhancing the thermal stability of the CNCs.

Figure 2.4 shows the XRD pattern of mCNC3-4 as a representative modified CNC sample, along with those of the corresponding ionomer, I3, and dried unmodified CNCs for comparison. According to literature, the diffraction peaks of cellulose I crystal structures in unmodified CNCs at 2θ values of 14.7, 17.0, 22.4, and 35.1º, are attributed to the (101), ($10\bar{1}$), (002), and (040), respectively.[54] I3 shows a broad diffraction peak centered at 18.3º within the 2θ range, which is the typical amorphous polymer peak found with this range of polyethylene-based ionomers.[49] The diffraction pattern of mCNC3-4 is superimposed by the peaks of both the original CNCs and the ionomer. The characteristic cellulose I diffraction peaks are well retained, confirming as expected that the CNC structures remain intact during this physical surface modification process.

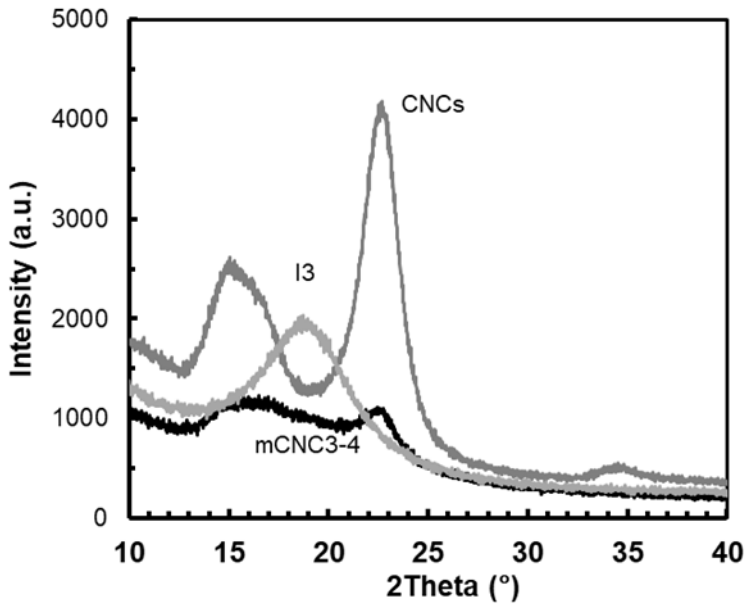

Figure 2.4 XRD diffraction patterns of mCNC3-4, I3, and dried unmodified CNCs.

2.3.2 Dilute Dispersions of Modified CNCs in Organic Solvents

Except for mCNC1 and mCNC3-1 due to insufficient ionomer coating, the dried modified CNC powders were found to be dispersible, upon sonication, in nonpolar or low-polarity organic solvents such as toluene, chloroform, and THF at dilute concentrations (around 10 $mg \cdot mL^{-1}$). The dispersions were found stable after ultrasonication for days while freeze-dried unmodified CNCs precipitated out nearly immediately after ultrasonication. However, they were not dispersible in water or high-polarity organic solvents (such as methanol, acetone, etc.) where the hyperbranched polyethylene ionomers themselves cannot disperse/dissolve, confirming the hydrophobic nature of the modified CNCs. Clearly, the dispersibility in these organic solvents can be attributed to the adsorbed ionomers. On the contrary, the large aggregates obtained in the control experiment by dropping the CNC into

pure THF without containing ionomers could not disperse THF at all due to the absence of ionomer coating.

DLS measurements were carried out on the dilute dispersions of various modified CNCs in THF to determine their Z-average hydrodynamic size (d_p), polydispersity index (PDI) of size distribution, and ζ potential. In particular, the data are listed in Table 2.2. Relative to those of the original CNCs in water (d_p = 91 nm; PDI = 0.3), all the modified CNCs show much greater d_p values (generally within 255–552 nm) and broader distribution (PDI in the range of 0.34–0.56). The higher particle sizes suggest the presence of CNC aggregates as a result of the "cross-linking" effect of the multidentate ionomers. This is further confirmed with the AFM images shown below. The ionomer modification also dramatically changes the ζ potential of the particles. Relative to the negative ζ potential of –27 mV of original CNCs, the set of modified CNC samples (mCNC2, mCNC3-3, mCNC4, mCNC5, and mCNC6) obtained at the same $(m_{ionomer}/m_{CNC})_0$ ratio with different ionomers shows increasing ζ potential values of –15, 17, 20, 22, 30 mV, respectively, with the gradual increase of ionic content in the ionomers. These ζ potential data confirm solidly the expected ionic binding of the cationic ionomers onto the negative charged CNCs, which effectively changes the surface charge of the particles. Particularly, those modified with I3–I6 have reversed charge due to the presence of excess quaternary ammonium cations.

2.3.3 Morphology of Modified CNCs by AFM

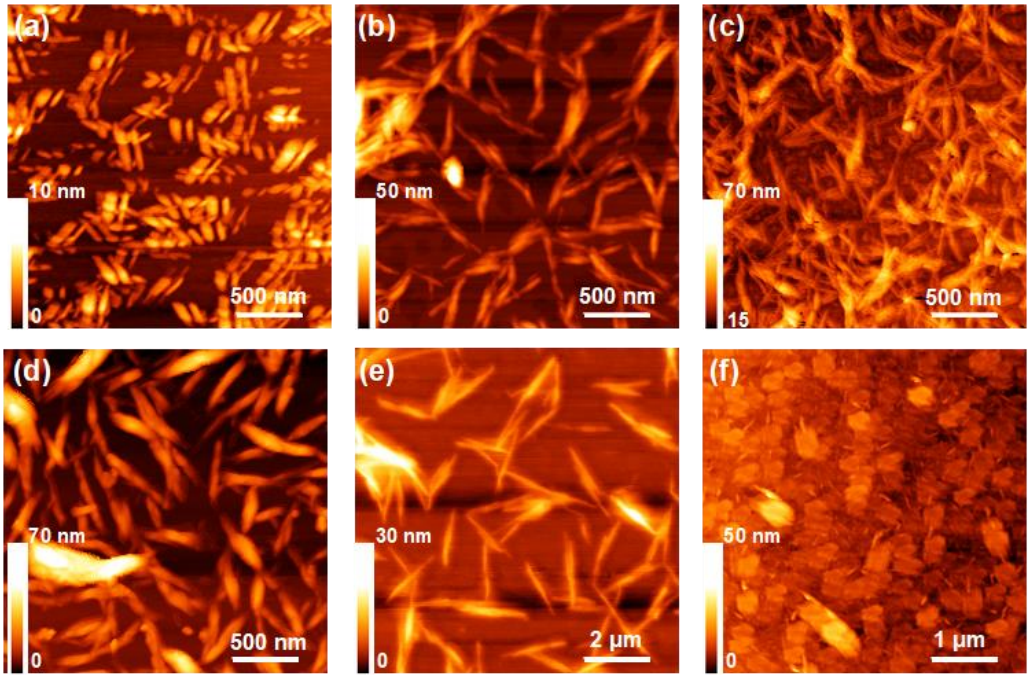

Figure 2.5 AFM height images of original unmodified CNCs (a), mCNC2 (b), mCNC3-3 (c), mCNC4 (d), mCNC6 (e, f).

AFM imaging of the morphology of modified CNCs was undertaken on samples prepared from their dilute dispersions in THF. Figure 2.5 shows typical AFM height images of original unmodified CNCs and representative modified CNCs (mCNC2, mCNC3-3, mCNC4, and mCNC6). Original CNCs (Figure 2.5(a)) show a rod-like shape with the average length and width of 119 ± 21 and 5 ± 1 nm, respectively. As opposed to the needle-like shape often observed under transmission electron microscopy, such a rod-like shape is typical of unmodified CNCs under AFM imaging due to the tip-broadening effect.[55] As such, the reported shape width data were all obtained from the AFM height profiles.[55] The ionomer modification dramatically changes the particle morphology by inducing the self-assembled

aggregations of individual CNC rods and the rod aggregates (see Scheme 2.1) due to the "cross-linking" or "bridging" effect of the ionomers.

The multidentate nature of the ionomers enables the binding of the different quaternary ammonium cations present in the same ionomer chain onto different CNC particles, causing the assembly. Meanwhile, the ionic aggregation ubiquitous in ionomers can also make a contribution through the ionic interactions of quaternary ammonium ions present in ionomer chains adsorbed on different CNC particles.

In mCNC2, mCNC3-3, and mCNC4, shapes appearing as bundles of CNCs formed through random side-to-side aggregation are extensively present (see Figure 2.5(b-d)). In these samples, the average shape length is 170 ± 33, 161 ± 28, and 403 ± 121 nm, respectively; the average width is 9 ± 2, 12 ± 4, and 19 ± 8 nm, respectively. Given the significantly greater shape length and width, the side-to-side aggregation is much more pronounced in mCNC4 than in mCNC2 and mCNC3-3, which is reasoned to result from the higher quaternary ammonium content in the enabling ionomer I4. More interestingly, two unique types of shapes with significantly larger dimensions are observed in mCNC6. Figure 2.5(e) shows a high-aspect-ratio, needle-like shape extensively present in mCNC6, which has a large average length of 1.5 ± 0.4 μm and an average width of 8 ± 2 nm, respectively. Its extremely long length indicates the extensive presence of longitudinal aggregation of CNC rods. Similar shapes resulting from longitudinal aggregation were previously reported on self-assembled duplexed DNA-grafted CNCs.[56] Figure 2.5(f) shows another sheet-like shape also extensively present in mCNC6, which is featured with a dimension of (320 ± 35) nm × (235 ±

38) nm, with a thickness of 10 ± 2 nm. This latter shape has not been previously reported for any modified CNCs. Herein, it was only observed in mCNC6 while not in the other modified CNCs. Its formation should involve highly ordered side-to-side assembly of the CNC rods. The formation of the two curious types of shapes in mCNC6 is puzzling and suggests future investigation. Given their sole presence in mCNC6, the ionic content of the enabling ionomers clearly plays a significant role in the self-assembly of the modified CNC rods to render the different shapes. On the contrary, the control sample obtained by dropping the neat CNC into pure THF without containing ionomers shows large irregular random aggregates (see Figure 2.6). A surfactant CTAB-modified CNC sample (CTAB-CNC) was also prepared as another control sample. It also shows dispersibility in THF. Like the ionomer-modified CNCs, its AFM images also show the presence of aggregates.

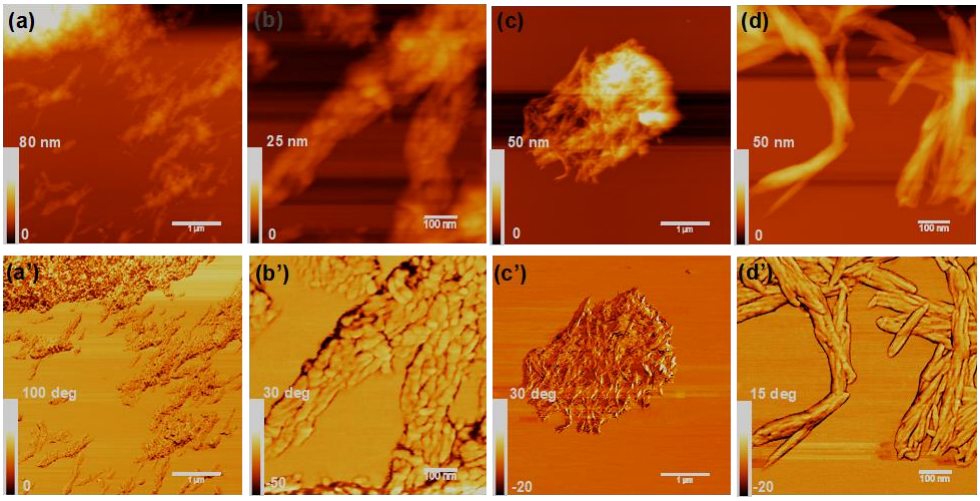

Figure 2.6 AFM height and phase images of aggregated CNCs obtained in the control experiment by dropping CNCs into pure THF (height images: a and b; phase images: a' and b'), CTAB-CNC dispersed in THF (height images: c and d; phase images: c' and d').

A representative AFM image taken on mCNC4 (Figure 2.7(a)) also provides some visual evidence confirming the presence of the ionomer coating around the shapes. In the image, every shape appears to be surrounded with a coating layer at the edge, which shows different phase compared to the surrounded area. Figure 2.7(b) shows the height profiles for two shapes denoted in Figure 2.7(a), which show the presence of the settled coating layer at a height of around 2.1–3.4 nm.

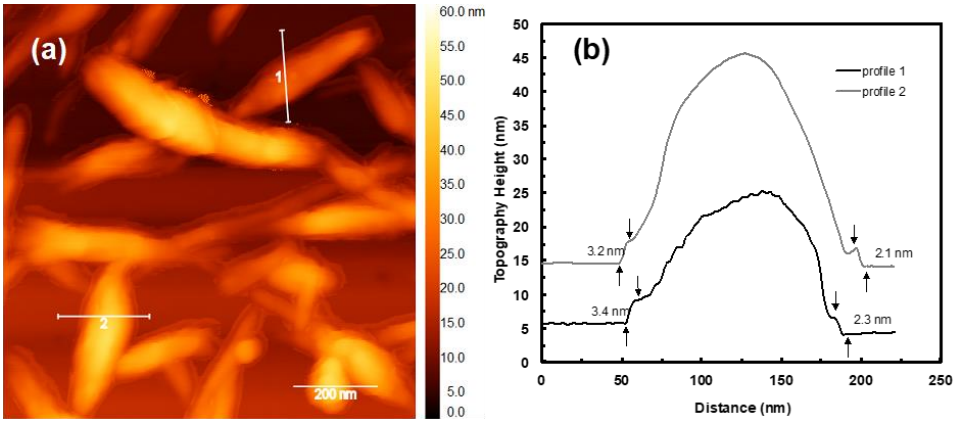

Figure 2.7 (a) AFM height image of mCNC4 at a higher magnification; (b) height profiles across two shapes denoted in (a).

2.3.4 Thixotropic Behavior of Dispersions of Modified CNCs in THF

Aqueous dispersions of sulfonated CNCs show interesting rheological behavior due to their unique rod-like shape with a charged surface and the tendency to form ordered liquid crystalline structures.[57,58] With the gradual increase of the CNC concentration, aqueous dispersions of CNCs transition from isotropic (CNC concentration ≤ ca. 3 mg·mL^{-1}) to a

biphasic suspension (ca. 3–10 mg·mL^{-1}) and to a birefringent gel-like material (≥ ca. 11 mg·mL^{-1}), which in turn changes their rheological properties.[59-61] The temperature,[60] aspect ratio,[62] surface charge,[63,64] addition of electrolytes[65,66] or polymers[67,68] into the aqueous dispersions of CNCs can also dramatically affect their rheological behavior. In addition, aqueous dispersions of HCl-hydrolyzed CNCs[69] and covalently modified cationic CNCs[70] have been reported to behave as thixotropic fluids. However, all the rheological studies have thus far focused on their aqueous dispersions, while with extremely limited study[44] on the dispersions of organo-dispersible CNCs in organic solvents.

The unique dispersibility of the ionomer-modified CNCs in nonpolar or low-polarity organic solvents enables us to study the rheological properties of their dispersions in THF. With mCNC4, a range of dispersions at different concentrations (10–75 mg·mL^{-1}) in THF was prepared. All the dispersions were left standing for a week after preparation. The dispersion at the lowest concentration of 10 mg·mL^{-1} was found to remain as a cloudy, readily flowable, isotropic dispersion without precipitation. On the contrary, all the other dispersions (within 25–75 mg·mL^{-1}) turned into white-colored organo-gels, suggesting the formation of a network structure in the dispersions. But all the dispersions/gels did not show birefringence, confirming the absence of ordered liquid crystal structures. In particular, the gels with mCNC4 concentration ≥ 40 mg·mL^{-1} remained stable even when their vials were inverted, but became readily flowable after being shaken (Figure 2.8(a,b)), indicating the breakdown of the internal structure under shear. Such a behavior is typical of thixotropic fluids. After being left overnight, the shaken flowable fluids turned back into the invertible gels again, suggesting the rebuilding of the network structure. It was found that the round-trip

transitions between gel and flowable fluid were reversible for the examined 4 cycles. The gel formed at the mCNC4 concentration of 25 mg·mL^{-1} was, however, not strong enough to support its own weight and flowed down upon the inversion of its vial (Figure 2.8(a)).

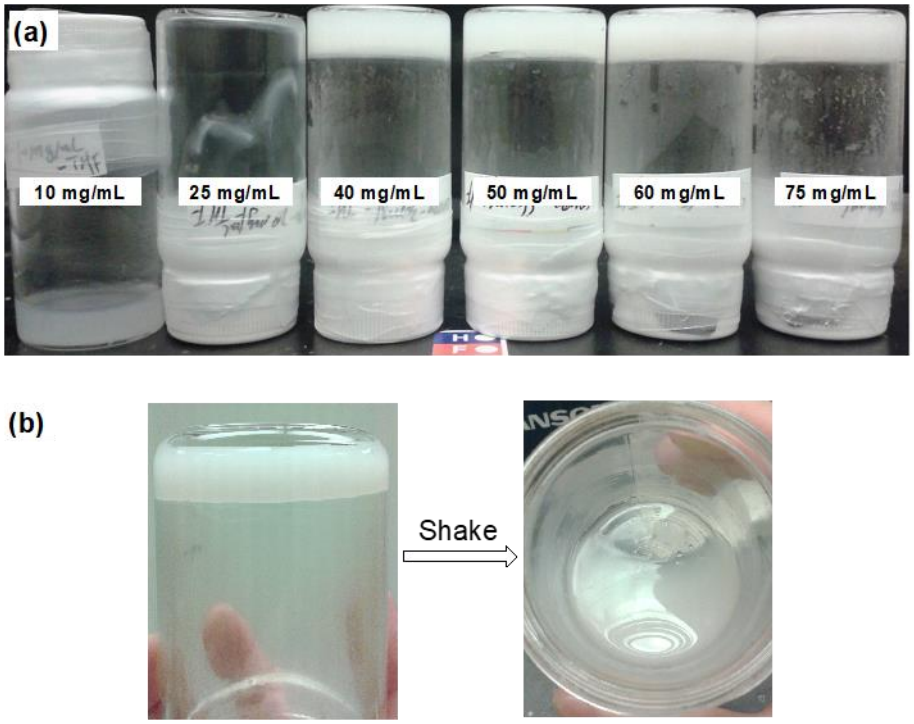

Figure 2. 8 (a) Dispersions and organo-gels of mCNC4 in THF at different concentrations (10–75 mg·mL^{-1}) after standing for a week; (b) the thixotropic behavior of the gels.

The organo-gels only formed in THF, while not in other solvents (toluene, chloroform, and chlorobenzene were examined). In these latter solvents, the dispersions, despite at high concentrations (75 mg·mL^{-1}), remained as isotropic flowable fluids even after long standing. This indicates the critical role of THF in facilitating the formation of the gel network structure in these dispersions. Clearly, the solvent-particle interactions contribute significantly to the gel formation. However, the precise mechanism for the formation of organo-gels in THF is not known at the moment and will require further investigation.

Rheological characterization of the dispersions with mCNC4 concentration within 40–75 $mg \cdot mL^{-1}$ was undertaken by both small amplitude dynamic oscillation and steady shear measurements at 10 ºC. Figure 2.9(a–d) shows the data obtained from the small amplitude dynamic oscillation measurements. At a high strain of 100%, the dispersions behave primarily as viscous fluids with loss modulus (G") greater than storage modulus (G') and both moduli show frequency dependences (Figure 2.9(a)). In Figure 2.9(b), the G" data at 0.01% is noisy; this may be caused by the continuing structure rebuilding or colloids rearrange after high strain measurement. In general, at a low strain of 0.01%, the dispersions are primarily elastic with G' much greater than G"; G' shows only very weak dependences on frequency, confirming their behavior approaching to ideal stiff gels (Figure 2.9(b)). For each dispersion, the complex viscosity (η^*) is more than one order of magnitude greater at the strain of 0.01% than at 100% (Figure 2.9(c)). The phase angle (δ) values at the strain of 0.01% stay nearly constant around 10 º across the frequency range for all these gels while the values are much greater at the strain of 100% along with the frequency dependences (Figure 2.9(d)). With the increase of the concentration of mCNC4 in the dispersions, the moduli and η^* values all increase. These oscillation results confirm the transition of the dispersions from elastic gel to viscous fluid following the breakdown of the gel network structure with the increase of strain.

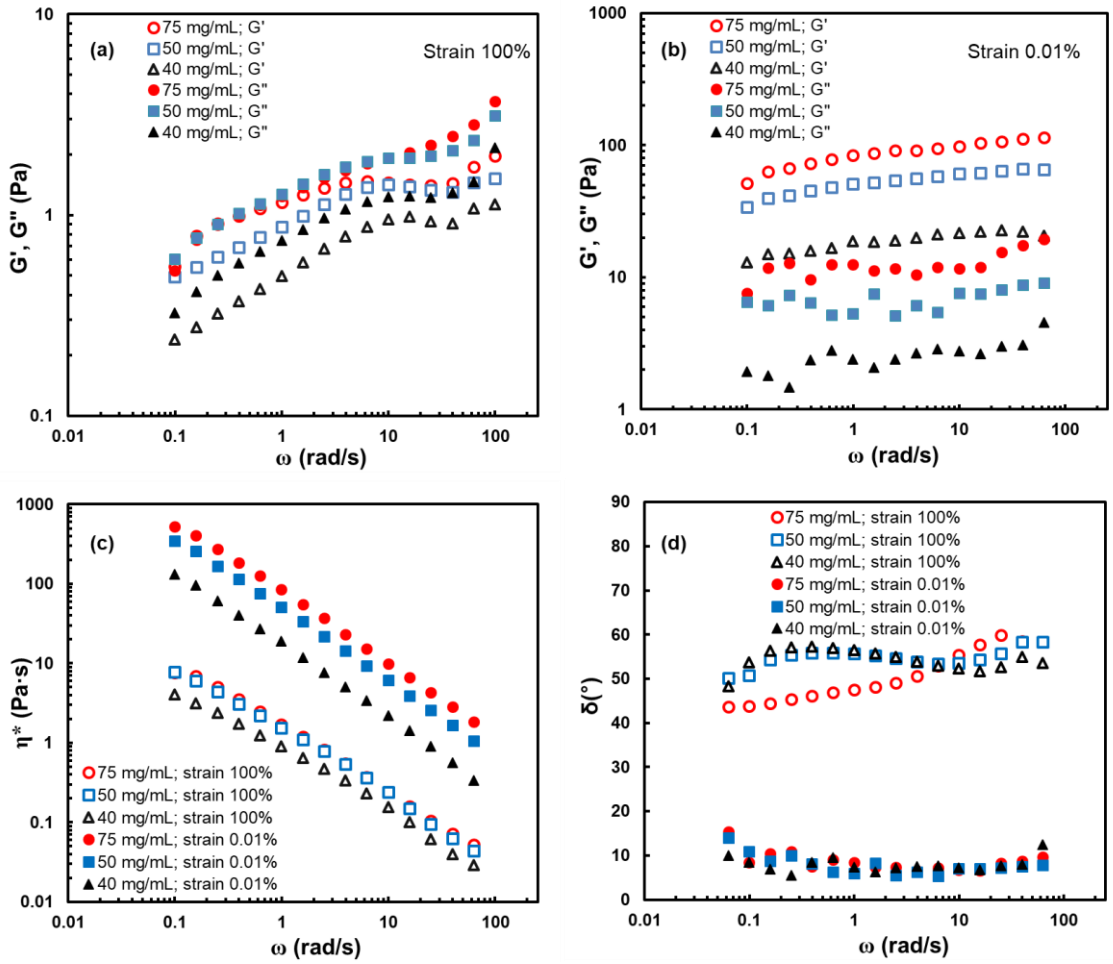

Figure 2.9 Rheological data from small amplitude dynamic oscillation measurements of organo-gels of mCNC4 in THF at different concentrations (40–75 mg·mL^{-1}) at 10 ºC: (a) dynamic moduli (G' and G") vs. frequency (ω) at the strain of 100%; (b) G' and G" vs. ω at the strain of 0.01%; (c) η* vs. ω at both strains of 100% and 0.01%; (d) phase angle (δ) vs. ω at both strains.

Figure 2.10 plots the viscosity vs. shear rate curves for the dispersions obtained in the steady shear measurements with up and down shear rate sweeps. The three dispersions show similar hysteresis loops characteristic of thixotropic fluids. The small bulge showing in the dispersion with the highest concentration (75 mg·mL^{-1}) might be caused by dilatant and shear

thinning. With the increase of the concentration of mCNC4, the area of the hysteresis loop shows a trend of increase, indicating that the extent of thixotropy increases with the concentration.

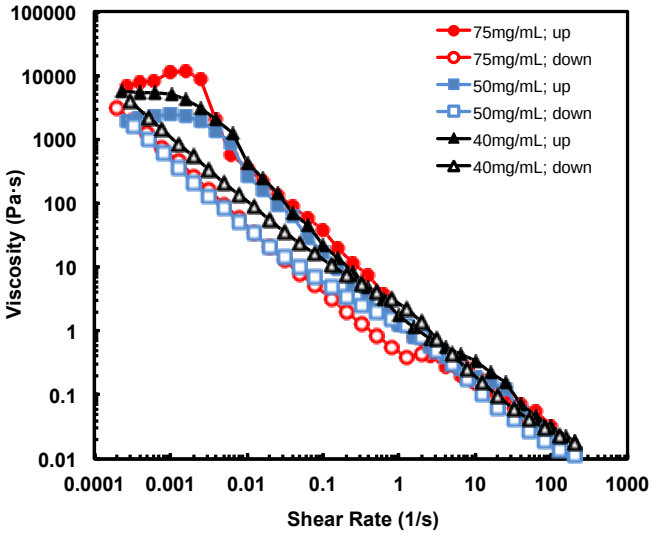

Figure 2.10 Viscosity vs. shear rate curves of thixotropic organo-gels of mCNC4 in THF at different concentrations (40–75 mg·mL^{-1}) obtained from shear measurements at 10 ºC.

Dispersions were also prepared with other modified CNCs [mCNC1, mCNC2, mCNC3-3, and mCNC6 prepared at the same $(m_{ionomer}/m_{CNC})_0$ ratio of 2] in THF at the same concentration of 75 mg·mL^{-1}. The dispersions of mCNC1 and mCNC2 remained as flowable fluids with no gel formation despite long standing while the others (prepared with mCNC3-3 and mCNC6) turned into thixotropic gels. This distinct difference suggests that the ionomers having varying ionic content employed for their surface modification plays the decisive role in the formation of gel network. Only dispersions of modified CNCs (mCNC3-3, mCNC4,

and mCNC6) prepared with ionomers of ionic content ≥ 0.7 mol% have the feature of gel formation. It is reasoned that the higher surface charge and higher shape aspect ratio following the modification of ionomers of high ionic content as shown above are the primary underlying causes of gel formation in these dispersions. It has been shown in earlier studies[62-64] that the surface charge and aspect ratio of sulfated CNCs can significantly affect gel formation.

2.3.5 EOC Composites with Modified CNCs as Reinforcing Fillers

The range of ionomer-modified CNCs was further investigated for their dispersion quality and reinforcing performance as fillers in a commercial EOC elastomer as the polymer matrix. Several grades of polyolefins (polyethylenes and polypropylenes) have been previously employed as the polymer matrices for the construction of CNC-filled composites,[32,71-77] but not ethylene-based elastomers. The EOC is chosen here because it should have good compatibility with the highly branched polyethylene skeleton in the ionomers given their structural similarity with high branching density (estimated at ca. 56 branches per 1000 carbons for EOC).[78] Composites were prepared with selected modified CNCs, including mCNC2, mCNC3-3, mCNC4, and mCNC5, at the targeted dry CNC loading of 10 wt% by the solution compounding method. In addition, composites were also prepared with dried unmodified CNCs and surfactant modified CNCs (CTAB-CNC), respectively, as fillers at the same dry CNC loading of 10 wt% for comparison. All resulting composites are named as filler/EOC (see Table 2.3).

TGA characterization of the composites was conducted. Figure 2.11 shows their TGA curves and the TGA results are summarized in Table 2.3. All the composites show a two-step weight loss. For those compounded with ionomer-modified CNCs and unmodified CNCs, the first-step weight loss occurs between 250 and 320 ºC, which is attributed to the decomposition of CNCs. For that compounded with CTAB-CNC, the first-step weight loss starts much earlier at ca. 200 ºC and is much broader (200–330 ºC), which is attributed to the decomposition/volatilization of both CNCs and the adsorbed CTAB. $T_{d,max}$ of the first step is appreciably higher in the composites compounded with ionomer-modified CNCs (286–308 ºC) than with unmodified CNCs (282 ºC) and CTAB-CNC (284 ºC), confirming again the relatively higher thermal stability of the ionomer-modified CNCs. Attributed primarily to the decomposition of EOC, the second-step weight loss occurs within 350–500 ºC for all the composites. In good agreement with the targeted value of 10 wt%, the mass content of dry CNCs in all composites was quantified, from the first-step TGA weight loss, to be about 10–11 wt%.

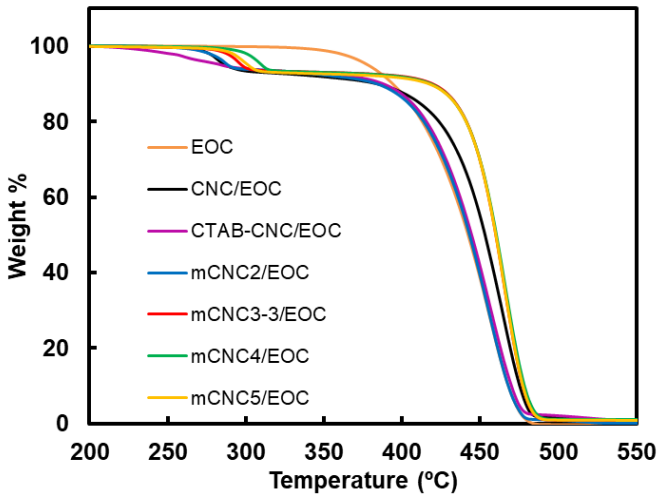

Figure 2.11 TGA curves of the various EOC composites and neat EOC. The measurements were undertaken at 10 ºC/min in N_2.

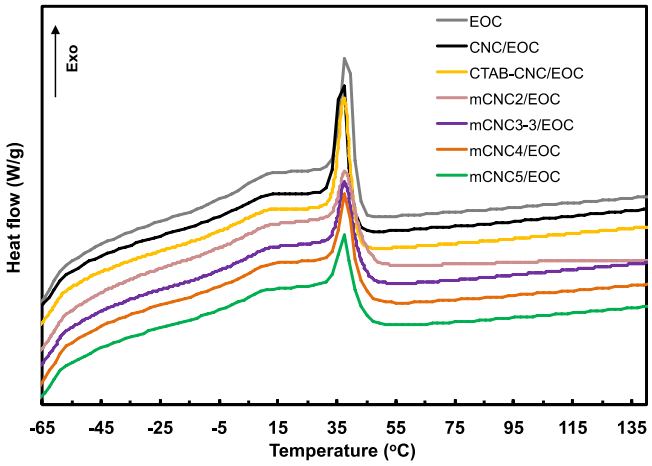

Figure 2.12 DSC crystallization curves of neat EOC and various EOC composites collected at cooling rate of 10 ºC/min.

DSC characterization was carried out to investigate the effects of the various fillers on the crystallization of the polymer matrix. Figure 2.12 shows the DSC crystallization exotherms of the various composites, along with that of neat EOC. The DSC results are also summarized in Table 2.3. Neat EOC shows a low onset crystallization temperature ($T_{c,onset}$) of 42 ºC and a small crystallization heat (ΔH_c) of 57 J/g due to its nature as a branched ethylene copolymer elastomer. The use of unmodified CNCs and CTAB-CNC as fillers leads to the negligible change in of $T_{c,onset}$. In contrast, the composites with the ionomer-modified CNCs as fillers all show appreciably increased $T_{c,onset}$ (43–45 ºC). Meanwhile, it also appears that the composites with ionomer-modified CNCs have slightly lowered ΔH_c (45–49 J/g) relative to those with unmodified CNCs and CTAB-CNC (49–50 J/g). These DSC results suggest that

the ionomer-modified CNCs are relatively better dispersed in the EOC matrix than unmodified CNCs and CTAB-CNC and can serve as nucleation agents facilitating the heterogeneous crystallization process.[79] It is known that the better dispersion of fillers helps increase the matrix-filler contact surface area and their interactions, rendering increased $T_{c,onset}$ and reduced ΔH_c.[79]

The composites, along with neat EOC, were characterized by small amplitude dynamic oscillation at 190 ºC to study the effects of various fillers on linear melt viscoelastic properties of the samples. Figure 2.13(a,b) compare their G' and δ curves, respectively. Neat EOC displays the typical viscous liquid-like behavior with $G' \propto \omega^{1.63}$ ($G'' = \omega^{0.98}$; G'' >> G') and $\delta \approx 90^{o}$ in the terminal flow range. The addition of dried unmodified CNCs in CNC/EOC at 10 wt% dramatically enhances G' by more than three orders of magnitude within the low-frequency range, along with a much lowered order (0.38) of dependence on ω. This indicates its solid-like behavior.[75,80] Meanwhile, its δ values are below 45º in the low frequency range, suggesting the presence of the percolated filler network within the composite.[75,80] As such, the dry CNC content of 10 wt% should be above the percolation threshold.

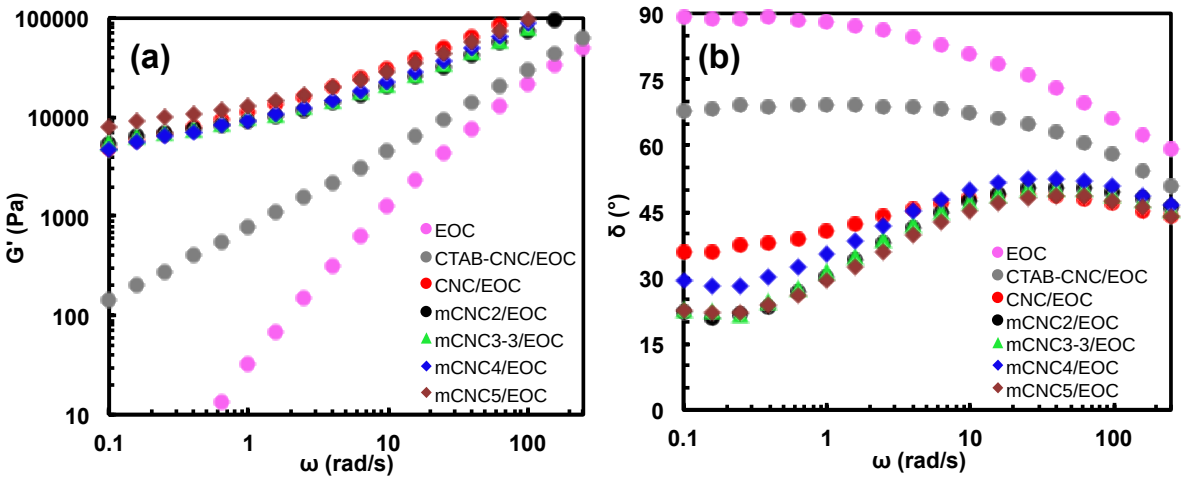

Figure 2.13 Results from dynamic oscillation measurements of various composites and neat EOC at 190 ºC: G' (a) and δ (b) as functions of frequency.

Table 2.3 Thermal and mechanical properties of EOC and its composites.

Sample	TGA results			DSC results[d]			Tensile properties[e]		
	$T_{d,max}$[a] (°C)	ΔW_1[b] (%)	Dry CNC content[c] (wt%)	$T_{c,onset}$ (°C)	ΔH_c (J/g)	T_c (°C)	σ_{max} (MPa)	ε_{max} (%)	Modulus[e] (MPa)
Neat EOC	N/A	0	0	42	57	46	2.9	1575	4.9
CNC/EOC	282	7	11	41	49	47	2.7	759	10
CTAB-CNC/EOC	284	6	10	41	50	48	2.7	832	9.5
mCNC2/EOC	286	6	10	45	50	52	2.3	1187	7.9
mCNC3-3/EOC	295	6	10	44	48	53	2.5	1099	8.5
mCNC4/EOC	308	7	11	43	49	53	2.5	1037	9.5
mCNC5/EOC	300	7	11	43	45	53	2.6	1071	9.7

[a] Peak decomposition temperature in the first-stage, weight loss within 200–330 °C. [b] Percentage weight loss in the first-stage within 200–330 °C. [c] Weight percentage of dry unmodified CNCs in the composites calculated by $\Delta W_1/0.63$. [d] Crystallization onset temperature ($T_{c,onset}$), crystallization temperature (T_c), and crystallization heat (ΔH_c) measured during the cooling step at rate of 10 °C/min. [e] Maximum tensile strength (σ_{max}), elongation at break (ε_{max}), and Young's modulus determined during tensile tests at 500 mm·min^{-1}.

The effects of CTAB-CNC on the rheological properties, however, are not so dramatic as the unmodified CNCs. CTAB-CNC/EOC still behaves primarily like a viscous liquid though with some level of enhancement in G' relative to neat EOC and the δ value shows a plateau at about 70º in the low frequency range. These results suggest the absence of the percolated filler network in CTAB-CNC/EOC even though the same dry CNC content of 10 wt% was used. This behavior is reasoned to result possibly from the desorption of CTAB or decomposition of the CTAB-CNC or both in the composite at the high measurement temperature. The sample discs of CTAB-CNC/EOC, prepared by compression molding at 135 ºC for rheology measurements, were yellow-colored as opposed to the white color found with all the other composites. This indicates the presence of decomposition even at 135 ºC when pressed at 2 MPa. Better dispersion of CTAB-CNC in EOC, may render liquid-like behavior. The desorbed CTAB or the decomposed low-molecular-weight products or both are reasoned to act as lubricants during the oscillation measurements, may also render viscoelastic solid-like flow behavior.

The ionomer-modified CNCs instead show even more dramatic effects on the rheological properties than unmodified CNCs. Significant enhancements in G' are noticed with the appearance of a plateau in the low frequency range for each one of them. The enhancements are even more significant in some of the composites than in CNC/EOC shown above. Meanwhile, the δ values of all the composites with modified CNCs are lower than those of CNC/EOC in the low frequency range. Such a flow behavior is commonly observed in percolated composites with increasing filler loading.[75,80] It indicates that not only the percolated filler network is present in all the composites filled with modified CNCs, but also the viscoelastic solid-like behavior is even more pronounced in them with stronger filler-filler and filler-matrix interactions than in CNC/EOC. Given their nearly identical dry CNC content, this rheological behavior is reasoned

to result from the better dispersion of the modified CNCs in the EOC matrix. Clearly, the ionomer modification makes the fillers more compatible with the EOC matrix, thus minimizing filler aggregation and increasing filler-matrix interface. In line with the DSC results, the rheological results also confirm the significant improvement caused by ionomer modification upon the dispersibility of the modified CNCs in EOC relative to the unmodified CNCs. Along with the TGA results discussed above, a comparison of their rheological results further verifies the higher thermal stability of ionomer-modified CNCs relative to CTAB-CNC.

The tensile mechanical properties of the various composites were characterized. The results are summarized in Table 2.3. Figure 2.14 compares the Young's modulus and elongation at break of the various composites and neat EOC. It is known that the inclusion of fillers in a polymer matrix has a reinforcing and stiffening effect, which is usually counteracted by a significant loss in ductility.[78,80] While increases in the moduli of polymer matrices are generally expected upon addition of reinforcing fillers, this reinforcement effect in polymer composites is typically accompanied by a significant reduction in elongation at break because of the presence of large aggregates that create weak spots.[78] These effects have also been observed with various CNC-filled polyolefin composites in earlier studies.[32,71,73,74,76,77] Herein, upon the addition of the various CNC fillers, the modulus is nearly doubled (from 4.8 MPa to 7.9–9.8 MPa) in all the composites, confirming the significant reinforcing effects of all the CNC-based fillers on the EOC. However, different extent of reductions in the elongation at break is found. The reduction is most severe in CNC/EOC and CTAB-CNC/EOC, with their values (759 and 832%, respectively) reduced nearly by half relative to that of neat EOC (1575%). Composites prepared with the ionomer-modified CNCs instead have maintained elongation at break (within the range of 1037–1186%). Relative to CNC/EOC and CTAB-CNC/EOC, their higher elongation at break

also confirms the improved dispersion of the modified CNCs in the matrix, as well as the improved interfacial adhesion between the modified CNCs and the matrix following ionomer modification.

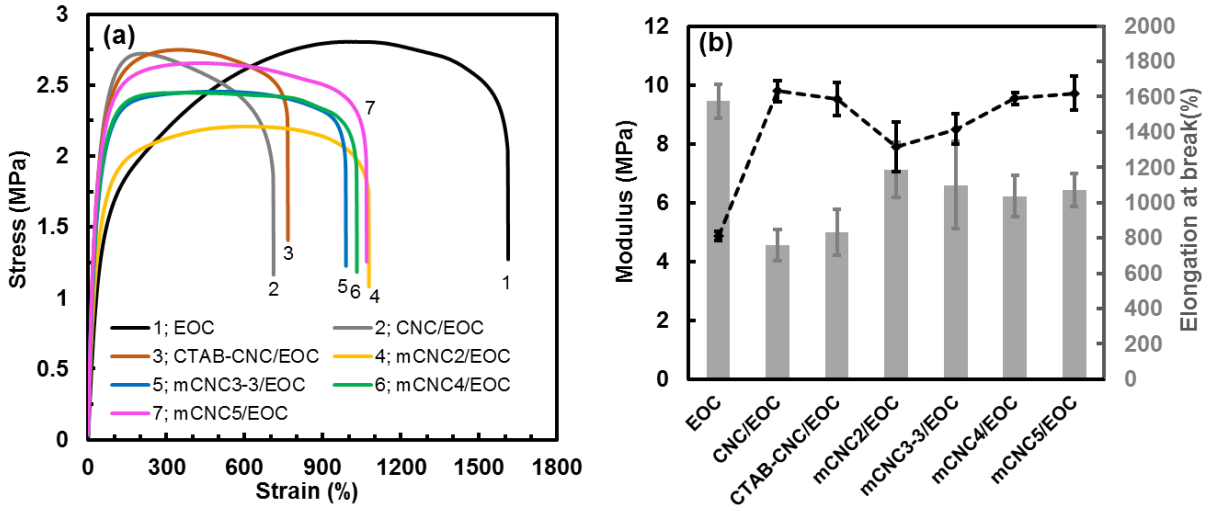

Figure 2.14 (a) Representative tensile strength vs. strain curves of neat EOC and various composites; (b) Comparison of secant modulus and elongation at break of neat EOC and various composites.

These tensile data thus confirm the advantages of the ionomer modification in improving the reinforcing performance of CNCs relative to unmodified CNCs and CTAB-modified CNCs. While there is no clear trend of differences observed among the composites compounded with the various ionomer-modified CNCs, mCNC5/EOC shows the optimally balanced tensile properties among the set, with the highest modulus of 9.7 MPa and an elongation at break of 1071%. Though demonstrated herein with the ductile EOC elastomer as the matrix, our findings here may be of significance when other polyolefin matrices are used, which may suffer significant loss in ductility in the presence of CNC-based fillers.

2.4 Conclusions

A range of quaternary ammonium-containing hyperbranched polyethylene ionomers (I1–I6) with different ionic content (0.2–2.3 mol%) has been synthesized and employed herein for the surface modification of CNCs. The simple addition and mixing of aqueous dispersion of CNCs with a THF solution of the ionomer renders conveniently the modified CNCs, primarily through the multidentate ionic assembly of the positively charged ammonium ions of the ionomers with the negatively charged CNCs. A range of modified CNCs has been prepared with the use of different ionomers. The presence of the adsorbed ionomers in the modified CNCs has been confirmed by FTIR, XRD, and TGA results. Quantification of the content of adsorbed ionomer in the modified CNCs by TGA indicates its increase with the increase of $(m_{ionomer}/m_{CNC})_0$ ratio or the ionic content of the ionomer. AFM imaging of the modified CNCs indicate their significantly enlarged shape size relative to unmodified CNCs, due to the occurrence of side-to-side and/or longitudinal assembly of individual CNCs upon ionomer modification.

Thanks to the hydrophobic hyperbranched polyethylene skeleton, ionomer-modified CNCs are dispersible in nonpolar or low-polarity solvents and hydrophobic EOC matrix. Most modified CNCs (except mCNC1 and mCNC3-1) are dispersible in solvents including THF, toluene, and chloroform. The dispersions of mCNC3-3, mCNC4, and mCNC6 in THF with concentration $\geq$ 40 mg·mL^{-1} has been found to behave as thixotropic organo-gels, which act as stiff gels at low strain (or shear rate) and as viscous fluids at high strain (or shear rate).

In the EOC matrix, the ionomer-modified CNCs show better dispersion as fillers than unmodified CNCs on the basis of the results from the thermal, rheological, and tensile

mechanical characterizations. Their better dispersion renders stronger filler-filler and matrix-filler interactions. In consequence, the EOC composites filled with the ionomer-modified CNCs are significantly reinforced with nearly doubled modulus relative to neat EOC while with much better maintained elongation at break relative those filled unmodified CNCs or CTAB-CNC.

Though demonstrated specifically with hyperbranched polyethylene-based ionomers herein, this efficient modification strategy should be general and applicable to other quaternary ammonium-containing ionomers. With the availability of various polymerization techniques for such ionomers, a rich variety of ionomer-modified CNCs can be rendered to suit various specific applications.

2.5 References

(1) De Souza Lima, M. M.; Borsali, R. *Macromol. Rapid Commun.*, **2004**, *25*, 771–787.

(2) Habibi, Y.; Lucian, L. A.; Rojas, O. J. *Chem. Rev.*, **2010**, *110*, 3479–3500.

(3) Moon, R. J.; Martini, A.; Nairn, J.; Simonsen, J.; Youngblood, J. *Chem. Soc. Rev.*, **2011**, *40*, 3941–3994.

(4) Klemm, D.; Kramer, F.; Moritz, S.; Lindström, T.; Ankerfors, M.; Gray, D.; Dorris, A. *Angew. Chem. Int. Ed.*, **2011**, *50*, 5438–5466.

(5) Lin, N.; Huang, J.; Dufresne, A. *Nanoscale*, **2012**, *4*, 3274–3294.

(6) Kelly, J. A.; Giese, M.; Shopsowitz, K. E.; Hamad, W. Y.; MacLachlan, M. J. *Acc. Chem. Res.*, **2014**, *47*, 1088–1096.

(7) Šturcová, A.; Davies, G. R.; Eichhorn, S. J. *Biomacromolecules*, **2005**, *6*, 1055–1061.

(8) Favier, V.; Canova, G. R.; Cavaillé, J. Y.; Chanzy, H.; Dufresne, A.; Gauthier, C. *Polym.*

Adv. Technol., **1995**, *6*, 351–355.

(9) Samir, M. A. S. A.; Alloin, F.; Dufresne, A. *Biomacromolecules*, **2005**, *6*, 612–626.

(10) Mariano, M.; El Kissi, N.; Dufresne, A. *J. Polym. Sci., Part B: Polym. Phys.*, **2014**, *52*, 791–806.

(11) Miao, C.; Hamad, W. Y. *Cellulose*, **2013**, *20*, 2221–2262.

(12) Shopsowitz, K. E.; Qi, H.; Hamad, W. Y.; MacLachlan, M. J. *Nature*, **2010**, *468*, 422–425.

(13) Khan, M. K.; Hamad, W. Y.; MacLachlan, M. J. *Adv. Mater.*, **2014**, *26*, 2323–2328.

(14) Giese, M.; Blusch, L. K.; Khan, M. K.; Hamad, W. Y.; MacLachlan, M. J. *Angew. Chem. Int. Ed.*, **2014**, *53*, 8880–8884.

(15) Giese, M.; Khan, M. K.; Hamad, W. Y.; MacLachlan, M. J. *ACS Macro Lett.*, **2013**, *2*, 818–821.

(16) Fox, J. D.; Capadona, J. R.; Marasco, P. D.; Rowan, S. J. *J. Am. Chem. Soc.*, **2013**, *135*, 5167–5174.

(17) Wang, B.; Walther, A. *ACS Nano*, **2015**, *9*, 10637–10646.

(18) Roohani, M.; Habibi, Y.; Belgacem, N. M.; Ebrahim, G.; Karimi, A. N.; Dufresne, A. *Eur. Polym. J.*, **2008**, *44*, 2489–2498.

(19) Bardet, R.; Belgacem, N.; Bras, J. *ACS Appl. Mater. Interfaces*, **2015**, *7*, 4010–4018.

(20) Samir, M. A. S. A; Alloin, F.; Sanchez, J. Y.; Dufresne, A. *Polymer*, **2004**, *45*, 4149–4157.

(21) Pranger, L.; Tannenbaum, R. *Macromolecules*, **2008**, *41*, 8682–8687.

(22) Querejeta-Fernández, A.; Chauve, G.; Methot, M.; Bouchard, J.; Kumacheva, E. *J. Am. Chem. Soc.*, **2014**, *136*, 4788–4793.

(23) Thérien-Aubin, H.; Lukach, A.; Pitch, N.; Kumacheva, E. *Angew. Chem. Int. Ed.*, **2015**, *54*, 5618–5622.

(24) Nguyen, T.-D.; Hamad, W. Y.; MacLachlan, M. J. *Adv. Funct. Mater.*, **2014**, *24*, 777–783.

(25) Wang, M.; Olszewska, A.; Walther, A.; Malho, J.-M.; Schacher, F. H.; Ruokolainen, J.; Ankerfors, M.; Berglund, L. A.; Österberg, M.; Ikkala, O. *Biomacromolecules*, **2011**, *12*, 2074–2081.

(26) Favier, V.; Chanzy, H.; Cavaillé, J. Y. *Macromolecules*, **1995**, *28*, 6365–6367.

(27) Hajji, P.; Cavaillé, J. Y.; Favier, V.; Gauthier, C.; Vigier, G. *Polym. Compos.*, **1996**, *17*, 612–619.

(28) Annamalai, P. K.; Dagnon, K. L.; Monemian, S.; Foster, E. J.; Rowan, S. J.; Weder, C. *ACS Appl. Mater. Interfaces*, **2014**, *6*, 967–976.

(29) Dagnon, K. L.; Shanmuganathan, K.; Weder, C.; Rowan, S. J. *Macromolecules*, **2012**, *45*, 4707–4715.

(30) Habibi, Y. *Chem. Soc. Rev.*, **2014**, *43*, 1519–1542.

(31) Eyley, S.; Thielemans, W. *Nanoscale*, **2014**, *6*, 7764–7779.

(32) Ljungberg, N.; Bonini, C.; Bortolussi, F.; Boisson, C.; Heux, L.; Cavaillé, J. Y. *Biomacromolecules*, **2005**, *6*, 2732–2739.

(33) Lin, N.; Dufresne, A. *Macromolecules*, **2013**, *46*, 5570–5583.

(34) Habibi, Y.; Dufresne, A. *Biomacromolecules*, **2008**, *9*, 1974–1980.

(35) Habibi, Y.; Goffin, A.-L.; Schiltz, N.; Duquesne, E.; Dubois, P.; Dufresne, A. *J. Mater. Chem.*, **2008**, *18*, 5002–5010.

(36) Morandi, G.; Heath, L.; Thielemans, W. *Langmuir*, **2009**, *25*, 8280–8286.

(37) Wang, H.-D.; Roeder, R. D; Whitney, R. A.; Champagne, P.; Cunningham, M. F. *J. Polym. Sci., Part A: Polym. Chem.*, **2015**, *53*, 2800–2808.

(38) Heux, L.; Chauve, G.; Bonini, C. *Langmuir*, **2000**, *16*, 8210–8212.

(39) Petersson, L.; Kvien, I.; Oksman, K. *Compos. Sci. Technol.*, **2007**, *67*, 2535–2544.

(40) Bondeson, D.; Oksman, K. *Compos. Interfaces*, **2007**, *14*, 617–630.

(41) Kim, J.; Montero, G.; Habibi, Y.; Hinestroza, J. P.; Genzer, J.; Argyropoulos, D. S.; Rojas, O. J. *Polym. Eng. Sci.*, **2009**, *49*, 2054–2061.

(42) Salajková, M.; Berglund, L. A.; Zhou, Q. *J. Mater. Chem.*, **2012**, 22, 19798–19805.

(43) Padalkar, S.; Capadona, J. R.; Rowan, S. J.; Weder, C.; Won, Y.-H.; Stanciu, L. A.; Moon, R. J. *Langmuir*, **2010**, *26*, 8497–8502.

(44) Abitbol, T.; Marway, H.; Cranston, E. D. *Nord. Pulp Pap. Res. J.*, **2014**, *29*, 46–57.

(45) Zhou, Q.; Brumer, H.; Teeri, T. T. *Macromolecules*, **2009**, *42*, 5430–5432.

(46) Cranston, E. D.; Gray, D. G. *Biomacromolecules*, **2006**, *7*, 2522–2530.

(47) Aloulou, F.; Boufi, S.; Beneventi, D. *J. Colloid Interface Sci.*, **2004**, *280*, 350–358.

(48) Mecking, S.; Johnson, L. K.; Wang, L.; Brookhart, M. *J. Am. Chem. Soc.*, **1998**, *120*, 888−899.

(49) Xiang, P.; Ye, Z. *Macromolecules*, **2015**, *48*, 6096−6107.

(50) Dong, Z.; Ye, Z. *Polym. Chem.*, **2012**, *3*, 286–301.

(51) Ye, Z.; Xu, L.; Dong, Z.; Xiang, P. *Chem. Commun.*, **2013**, *49*, 6235–6255.

(52) Espinosa, S. C.; Kuhnt, T.; Foster, E. J.; Weder, C. *Biomacromolecules*, **2013**, *14*, 1223−1230.

(53) Roman, M.; Winter, W. T. *Biomacromolecules*, **2004**, *5*, 1671−1677.

(54) Xu, X.; Liu, F.; Jiang, L.; Zhu, J. Y.; Haagenson, D.; Wiesenborn, D. P. *ACS Appl.*

Mater. Interfaces, **2013**, *5*, 2999−3009.

(55) Kvien, I.; Tanem, B. S.; Oksman, K. *Biomacromolecules*, **2005**, *6*, 3160−3165.

(56) Mangalam, A. P.; Simonsen, J.; Benight, A. S. *Biomacromolecules*, **2009**, *10*, 497−504.

(57) Beck-Candanedo, S.; Roman, M.; Gray, D. G. *Biomacromolecules*, **2005**, *6*, 1048−1054.

(58) Revol, J.-F.; Godbout, L.; Dong, X.-M.; Gray, D. G.; Chanzy, H.; Maret, G. *Liq. Cryst.*, **1994**, *16*, 127−134.

(59) Bercea, M.; Navard, P. *Macromolecules*, **2000**, *33*, 6011−6016.

(60) Ureña-Benavides, E. E.; Ao, G.; Davis, V. A.; Kitchens, C. L. *Macromolecules*, **2011**, *44*, 8990−8998.

(61) Shafiei-Sabet, S.; Hamad, W. Y.; Hatzikiriakos, S. G. *Langmuir*, **2012**, *28*, 17124−17133.

(62) Wu, Q.; Meng, Y.; Wang, S.; Li, Y.; Fu, S.; Ma, L.; Harper, D. *J. Appl. Polym. Sci.*, **2014**, *131*, 40525.

(63) Araki, J.; Wada, M.; Kuga, S.; Okano, T. *J. Wood Sci.*, **1999**, *45*, 258−261.

(64) Shafeiei-Sabet, S.; Hamad, W. Y.; Hatzikiriakos, S. G. *Rheol. Acta*, **2013**, *52*, 741–751.

(65) Dong, X. M.; Kimura, T.; Revol, J.-F.; Gray, D. G. *Langmuir*, **1996**, *12*, 2076–2082.

(66) Boluk, Y.; Lahiji, R.; Zhao, L.; McDermott, M. T. *Colloids Surf. A: Physicochem. Eng. Asp.*, **2011**, *377*, 297–303.

(67) Boluk, Y.; Zhao, L.; Incani, V. *Langmuir*, **2012**, *28*, 6114–6123.

(68) Hu, Z.; Cranston, E. D.; Ng, R.; Pelton, R. *Langmuir*, **2014**, *30*, 2684–2692.

(69) Araki, J.; Wada, M.; Kuga, S.; Okano, T. *Colloids Surf. A: Physiochem. Eng. Asp.*, **1998**, *142*, 75–82.

(70) Hasani, M.; Cranston, E. D.; Westman, G.; Gray, D. G. *Soft Matter*, **2008**, *4*, 2238–2244.

(71) Ljungberg, N.; Cavaillé, J.-Y.; Heux, L. *Polymer*, **2006**, *47*, 6285–6292.

(72) Azouz, K. B.; Ramires, E. C.; Van den Fonteyne, W.; El Kissi, N.; Dufresne, A. *ACS Macro Lett.*, **2012**, *1*, 236–240.

(73) Pereda, M.; El Kissi, N.; Dufresne, A. *ACS Appl. Mater. Interfaces*, **2014**, *6*, 9365–9375.

(74) De Menezes, A. J.; Siqueira, G.; Curvelo, A. A. S.; Dufresne, A. *Polymer*, **2009**, *50*, 4552–4563.

(75) Khoshkava, V.; Kamal, M. R. *ACS Appl. Mater. Interfaces*, **2014**, *6*, 8146–8157.

(76) Sapkota, J.; Jorfi, M.; Weder, C.; Foster, E. J. *Macromol. Rapid Commun.*, **2014**, *35*, 1747–1753.

(77) Iyer, K. A.; Schueneman, G. T.; Torkelson, J. M. *Polymer*, **2015**, *56*, 464–475.

(78) Xiang, P.; Petrie, K.; Kontopoulou, M.; Ye, Z.; Subramanian, R. *Polym. Chem.*, **2013**, *4*, 1381–1395.

(79) Gopakumar, T. G.; Lee, J. A.; Kontopoulou, M.; Parent, J. S. *Polymer*, **2002**, *43*, 5483−5491.

(80) Bailly, M.; Kontopoulou, M.; El Mabrouk, K. *Polymer*, **2010**, *51*, 5506−5515.

Chapter 3

Facile Preparation of Strong, Tough Metal Ion Cross-linked Sodium Alginate-Cellulose Nanocrystal Nanocomposite Films

Abstract

Cellulose nanocrystals (CNCs) and sodium alginate (SA) are natural biopolymers of interest for nanocomposites due to their excellent biodegradability, sustainability, and unique properties. In this chapter, a study on the synthesis, structure, and properties of strong tough SA-CNC nanocomposite films has been undertaken. A range of composite films with CNC content ranging from 10 to 97.5 wt% has been prepared simply by solution casting. The interactions between CNCs and SA have been examined with the use of dynamic light scattering and atomic force microscopy. The structure, optical, and thermal properties have been examined with UV-vis, Fourier-transform infrared spectroscopy, and thermogravimetric analysis, respectively. The composite films have also been tested for their tensile mechanical properties. Both thermogravimetric analysis and tensile testing have shown the synergistic reinforcing effects, with significantly improved thermal stability and tensile properties relative to neat SA and CNCs. The effects of the composition and further metal ion cross-linking on the tensile properties of the composite films have also been examined. The optimum calcium ion cross-linked composite films show high tensile strength and high toughness, which well exceed those of some natural and artificial nacres.

3.1 Introduction

Polymer nanocomposite films make up a class of versatile film materials, prepared from the combination of soft polymer matrices and robust nanoparticles. Normally, composite films display improved thermal or mechanical properties that are absent in neat polymers, due to the incorporated nanoparticles and the created interface.[1,2] Polymer nanocomposite films have been widely used as coating and packaging materials, and there is growing research interest in fabricating sustainable and renewable composite films.[3]

Cellulose nanocrystals (CNCs) have gained considerable attention due to the excellent mechanical property, benign ecological, low energy consumption and some other advantages.[4] More recently, intense efforts have been devoted to fabricating nanocomposite films by using CNC and different types of polymer matrices. Various natural and synthetic polymer matrices, such as alginate,[5] silk,[6] poly(lactic acid),[7] poly(vinyl alcohol)[8] have been used, and the resulting composite films demonstrated impressive enhancement of the mechanical performance compared to neat polymer films. Sodium alginate (SA) is a low-cost, water-soluble polysaccharide extracted from natural brown algae or seaweed. SA is compatible with cellulose, and it has excellent film formation property due to the mannuronic acid and guluronic acid units.[9] Each unit contains a carboxylic acid group, and the guluronic acid units can interact with different multivalent metal ions to form cross-linked structures.[5,10] For these reasons, SA or SA based materials are commonly used in the preparation of hydrogels, biomedical materials, eco-friendly absorbents, biodegradable films, etc.[9-12]

SA films are relatively weak in mechanical strength.[5] However, mixing SA with CNCs results in the composite films with enhanced mechanic properties, wherein CNCs act as the reinforcing nanofillers. There are few reports on the preparation and investigation of CNC/SA composites. Deepa et al.[9] reported a maximum increase of ca. 36% in tensile strength for the composite with 10 wt% of cellulose nanofibrils (CNFs) relative to the neat SA. They claimed that a higher content of CNFs was not suitable for composite preparation due to the excess chain entanglement and aggregation. Similarly, cellulose fibers were also used as the reinforcing fillers for the preparation of alginate composite film.[13,14] Huq et al.[15] prepared and studied the effect of CNC loadings on the mechanical property of SA/CNC composite films. The CNC content studied was in the range of 1 to 8 wt%; and it was found that the optimal composite film showed about 37% higher in strength compared to the neat SA film. While previous studies focused on the mechanical properties of composite films at low nanofiller loadings, there is still room for investigations on how the strength of composites changes with composition or even some other components. To this end, the main objective of this study is to prepare the SA/CNC based composite films and assess the potential mechanical property. The CNC loading in composites ranges from 10 wt% to 97.5 wt%. The optical, thermal and mechanical properties of the binary films have been characterized. Furthermore, composite films cross-linked by calcium ion and some other metal ions have been successfully prepared. The effects of the amount of calcium ion and the types of metal ions on modulating the composite tensile strength have been investigated.

3.2 Experimental Section

3.2.1 Materials

Cellulose nanocrystal aqueous dispersion (5.1 wt%) used in this study was supplied by CelluForce (Canada). Sodium alginate (W201502, Aldrich), $CaCl_2$ (anhydrous, ACS reagent, ≥ 96%), $NiCl_2{\cdot}6H_2O$ (ReagentPlus®), $ZnCl_2$ (anhydrous, Redi-Dri^{TM}, reagent grade, ≥ 98%), $CoSO_4{\cdot}7H_2O$ (ReagentPlus®, ≥ 99%), $MnSO_4$ H_2O (ReagentPlus®, ≥ 99%), $CuSO_4{\cdot}5H_2O$ (ACS reagent, ≥ 98%), $MgSO_4$ (anhydrous, ReagentPlus®, ≥ 99.5%), $Fe_2(SO_4)_3{\cdot}xH_2O$ (Fe 21-23 %), $Fe(NO_3)_3{\cdot}9H_2O$ (ACS reagent, ≥ 98%), $FeCl_3$ (reagent grade, 97%), $AlCl_3$ (ReagentPlus®, 99%) were obtained from Aldrich. Water with a resistivity of ca. 18 MΩ·cm was produced with a Milli-Q® Direct 16 Water Purification System, and was used for dispersion preparation and metal ion solution preparation.

3.2.2 Preparation of SA-CNC Composite Films

SA solution was prepared by dissolving the SA powder (3 wt%) in deionized water under stirring at 50 °C. Then, a desired amount of SA solution was mixed with a prescribed volume of diluted CNC dispersion (2 wt%). The original light blue color of the CNC dispersion was changed into light ivory color after the addition of SA solution. The resulting solution was further stirred at room temperature for 4 h. Afterwards, it was subjected to vacuum and sonication to remove the trapped air inside the viscous solution, and used as the casting solution for film preparation. Subsequently, 4 g of the casting solution was cast onto a polystyrene culturing dish (47 mm in diameter, Thermo Fisher Scientific). The dish was kept at room

temperature for ca. 2 days for film formation by water evaporation. A series of composite films were prepared by altering the CNC content (10, 30, 50, 70, 80, 90, 92.5, 95, and 97.5 wt%, with the films denoted as SA-CNC10, SA-CNC30, SA-CNC50, SA-CNC70, SA-CNC80, SA-CNC90, SA-CNC92.5, SA-CNC95, SA-CNC97.5, respectively). The films were peeled off from the dishes, cut into stripes, stored in sealed sandwich bags. The stripped films were annealed at 80 °C under vacuum for 1 h prior to characterizations. Ion cross-linked composite films were prepared similarly. After the casting of SA/CNC solution in the culturing dish, a prescribed volume of calcium chloride solution or other salt solution (0.75 wt%) was slowly sprayed onto the SA/CNC sol (ca. 2 g casting solution) in the dish with a sprayer. The ions diffused through the sol and induced gelation. After evaporation in air for 2 days, the ion cross-linked films were obtained. They were stored and annealed prior to characterizations as described above. The cross-linked films are named by adding the molar percentage of calcium (or other ions) relative to carbonate groups in the composite.

3.2.3 Characterizations

Fourier-transform infrared (FTIR) spectra of the films were obtained on a Nicolet 6700 Analytical FTIR spectrometer. The measurements were performed in the ATR mode. UV-vis spectroscopy was performed on a Thermoscientific Genesys 10S UV-vis spectrophotometer. Dynamic lighting scattering (DLS) and Zeta-potential measurements were performed with a Brookhaven Omni instrument which was equipped with a high power 35 mW diode laser. Each sample (ca. 0.5 wt%) was measured for five times and the average values were used. Thermogravimetric analysis (TGA) was carried out in a nitrogen atmosphere on a TA Q50 thermogravimetric analyzer at a heating rate of 20 °C/min. X-ray diffraction (XRD) experiments

were performed on an X'Pert Pro diffractometer using Cu Kα radiation. The mechanical tensile testing was performed on a TA instrument Q800 dynamic mechanical analyzer (DMA) at a test speed of 0.3%/min with a fixed gauge length of 8 mm. All the rectangular strips had the width of about 2 mm and length of about 35 mm. The thickness of the films was determined with an optical microscopy. Atomic force microscopy (AFM) images were acquired on a Bruker Instruments Nanoscope 3D Multimode Atomic force microscope operating in the tapping mode.

3.3 Results and Discussion

3.3.1 Interactions between SA and CNCs

SA is an anionic polysaccharide bearing carboxylate groups while CNC nanoparticles are negatively charged with the presence of surface sulfate groups. Both are water soluble/dispersible and are thus expected to be compatible. To investigate the possible interactions between the two, dilute solutions containing both SA and CNCs at different compositions (total concentration, 0.5 wt%; SA/CNC mass ratio = 100:0, 50:50, 30:70, 20:80, 10:90, 0:100, respectively) were characterized with DLS. For SA solution, the obtained average diameter and surface charge are 895 ± 130 nm and –78 ± 4 mV. The average diameter and surface charge obtained from original CNC dispersion are 128 ± 2 nm and –36 ± 5 mV, which indicates stable CNC suspension in water with relatively narrow particle size distribution.[16] Figure 3.1 shows the average hydrodynamic size and zeta potential of the particles in the SA/CNC solutions of varying compositions. Incorporation of SA in the dispersion of CNCs increases the overall particle average size. Comparing to original CNCs, the composites show

lower zeta potential values down to -70 mV; the zeta potential values are more negative for composites, caused by the surface carboxylic groups and anionic sulfated groups.

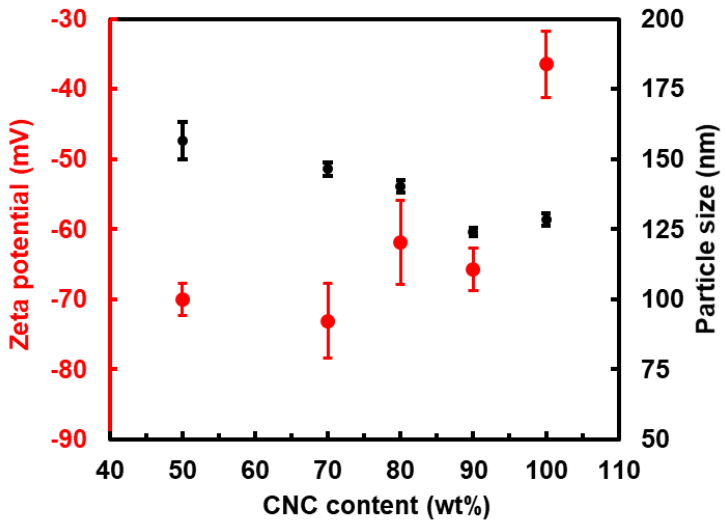

Figure 3.1 Average particle hydrodynamic diameter and zeta potential values of dilute solutions of SA and CNC at different compositions.

Surface morphology of SA-CNC composite thin films has been evaluated with AFM. Figure 3.2 shows the AFM images of the films of CNCs, SA-CNC90, and SA-CNC80. Randomly distributed CNC nanorods are distinctly observed in the image (Figure 3.2(a)) for the neat CNC sample,[17] with an average length of 107 ± 25 nm and an average diameter of 6.4 ± 0.2 nm. Meanwhile, the film of neat CNCs has a root-mean-square surface roughness of ca. 1.6 nm. Due to the presence of SA, the two composite films show different surface morphology. In SA-CNC90 with a higher CNC content (90 wt%), the majority of the CNC nanoparticles appear to aggregate to form bundles with the nanorod morphology still clearly seen. In SA-CNC80, some hazy polymer, supposed to be SA, can be observed on the surface, obscuring the clear observation of the CNC nanorods underneath. Nevertheless, CNC nanorod bundles can still be

seen though not as clear as in SA-CNC90. The formation of the nanorod bundles indicates the side-to-side aggregation of the CNC nanorods in the presence of SA. This is also suggestive of the coating of SA on the surface of CNC nanorods, which leads to the aggregation. The mean square surface roughness in SA-CNC90 and SA-CNC80 is 3.3 and 6.4 nm, respectively, significantly higher than that in the neat CNC sample. Clearly, the formation of larger bundles leads to coarser surface with higher porosity.

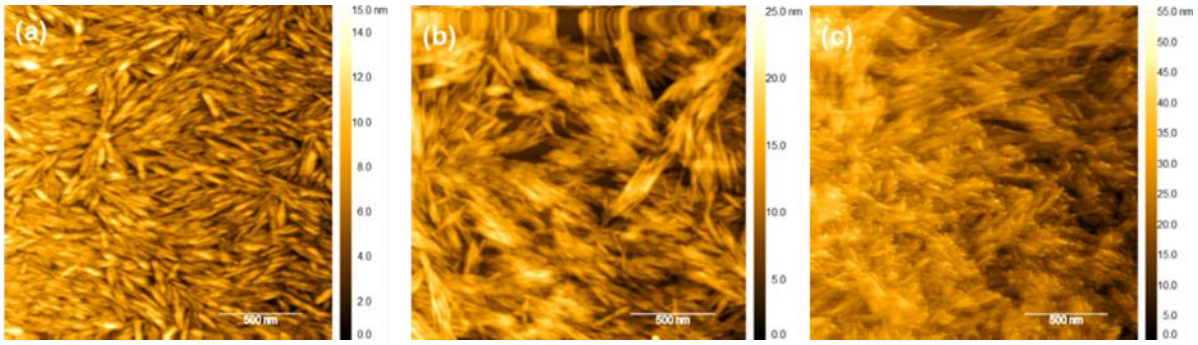

Figure 3.2 Tapping-mode AFM height images of the surface of thin films of (a) CNCs, (b) SA-CNC90, (c) SA-CNC80.

3.3.2 Optical Properties of SA-CNC Composite Films

A range of free-standing SA-CNC composite films (ca. 30 μm in thickness) at different compositions has been prepared by the solution casting method. Optical properties of the films have ben examined with UV-vis spectrophotometry. Figure 3.3 shows the UV-vis transmission spectra of the films. For the neat CNC film, a distinct peak is observed within 400–580 nm, indicative of the characteristic ordered liquid crystal structures present in the CNC film.[18] However, there is no peak found in the whole region of 200–1000 nm for the composites despite at low SA loadings, as well as SA. This indicates that the addition of SA polyelectrolyte even at

as low as 10 wt% disrupts the formation of the ordered liquid crystal structures in the composites. Similarly, Wang et al. reported the absence of ordered structures in the non-ionic PVA-CNC composites with PVA at a content greater than 40 wt%.[8] Compared to the neat CNC film, the SA-CNC90 film has much lower transmittance across the whole spectrum. This is possibly because of the non-uniform distribution of the SA and CNCs in the composite, causing light scattering and decreasing film transparency.[19] An increase in SA content from SA-CNC90 to SA-CNC30 leads to a gradual increase in the transmittance. Reducing the CNC content to 50 wt% gives the SA-CNC50 composite film the similar transparency as the neat SA film. The composites with the CNC content ≤ 50 wt% show high transmittance values (> 80%) within nearly the whole visible region. Voids are possibly diminished in these composites, giving higher optical transmittance.[20]

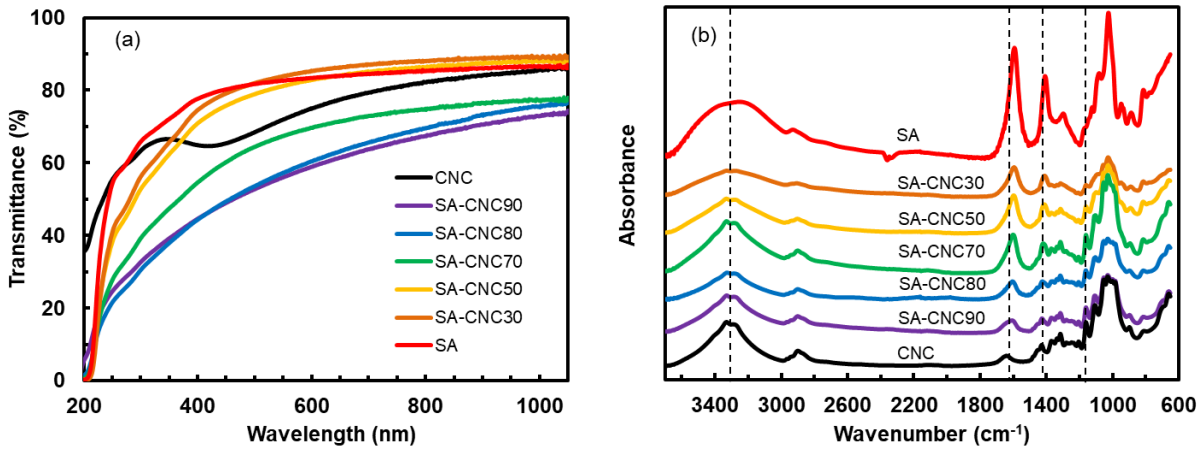

Figure 3.3 (a) UV-vis and (b) FTIR spectra of CNCs, SA and composites.

ATR-FTIR spectra of films of neat CNC, neat SA, and the composites are presented in Figure 3.3(b). Generally, all the films show similar characteristic bands for hydrophilic carbohydrates. Bands at around 3350 cm^{-1} and 2900 cm^{-1}, attributable to O-H and C-H stretching

vibrations, respectively, are observed in all the films. Compared to neat SA, the band at 3350 cm^{-1} band is sharper in neat CNCs and the composites, suggesting the presence of enhanced hydrogen bonding in neat CNCs and the composites.[15] The spectrum of neat CNCs have a relatively weak O-H bending vibration band at 1640 cm^{-1} and a broad C-O-C pyranose ring stretching vibration band at 1160-960 cm^{-1}.[21] The spectrum of neat SA shows two intense bands at around 1600 cm^{-1} and 1410 cm^{-1} assigned to COO^- stretching vibrations.[22] These two latter bands are distinctly present in the composites, with increasing intensities upon the increase of SA content. In addition, a band at 1160 cm^{-1}, which is absent in neat SA, shows the increased intensity as the fraction of CNC increases, which is often seen in typical cellulosic compound.[15]

3.3.3 Thermal Properties of SA-CNC Composite Films

TGA and derivative TGA curves for all samples are shown in Figure 3.4. All samples show an initial weight loss at 100 °C, due to the evaporation of surface adsorbed moisture and the trapped water in the samples. The initial weight loss is about 4%, 8.5%, and 5.5% for the neat CNCs, the neat SA and SA-CNC30, and the other composites, respectively. SA and SA-CNC30 that has the highest SA content among the composites show the highest initial weight loss due to the hydrophilic and non-crystalline nature of SA. Neat SA has the lowest temperature stability, with the major weight loss occurring within 200–260 °C (see Figure 3.4(b)). Compared to neat SA sample, the neat CNCs has a better stability due to its crystalline structure, with the major weight loss occurring at higher temperatures in the range of 230–300 °C and the peak-maximum temperature at ca. 255 °C. On the contrary, all the SA-CNC composites show improved stability compared to neat SA and neat CNCs. From Figure 3.4(b), the major weight loss of the

composites generally occurs within 200–360 °C depending on the CNC content. Two distinct degradation peaks are observed from their differential TGA curves. While the lower-temperature peaks are within 200–250 °C for all the composites (attributable to SA in the composites), the other higher-temperature peaks show the gradually broadened width along with increasing peak-maximum temperature and increasing peak intensity with the increase of CNC content. The higher-temperature peaks should thus correspond to the degradation of the CNC component in the composites. SA-CNC30 has the higher-temperature peak within 250–300 °C, which is a minor peak relative to the lower-temperature peak, with the peak maximum at 268 °C. SA-CNC90 has the higher-temperature peak within 270–360 °C, which is the dominant peak, with the peak-maximum temperature of 330 °C. The peak-maximum temperature of SA-CNC90 is significantly higher (75 °C) than that of neat CNCs, making it the most stable sample. This is also suggestive of the strong interactions between SA and CNCs, which improves the thermal stability of the composites. Similar features were also observed with CNC/chitosan composite films.[23] In addition, the char yield at 650 °C of neat SA sample and the composites having higher SA contents (≥ 30 wt%) are higher (31–34%) than the values (ca. 23 wt%) of neat CNCs and other composites of lower SA contents (≤ 20 wt%). This is reasoned to result from sodium carbonate produced from the degradation of SA.[24]

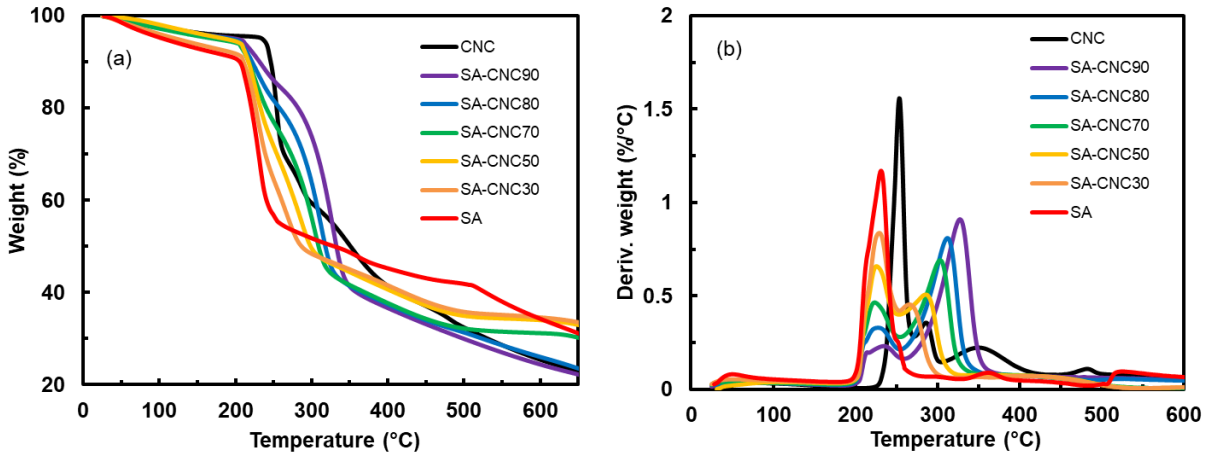

Figure 3.4 (a) TGA and (b) derivative curves of CNCs, SA and the composites in a N_2 atmosphere with a heating rate of 20 °C/min.

3.3.4 Tensile Mechanical Properties of SA-CNC Composite Films

Tensile tests were performed on the SA-CNC composite films to demonstrate the effect of CNCs on the mechanical properties. The tests were performed at room temperature with the relative humidity of 45%. All films were dried in a vacuum oven at 80 °C for 1 h to remove adsorbed moisture, which often acts as a plasticizer and causes the deterioration of mechanical properties.[25] Figure 3.5(a) plots the tensile strength and strain of the composite films as functions of CNC content. The neat CNC films are herein measured to have the average strength and strain of 132 ± 15 MPa and 1.1 ± 0.3 %, respectively, suggesting the typical brittle characteristics. The neat SA films show an average strength of 155 ± 12 MPa and an average strain of 11.2 ± 0.5 %, suggesting that they are typical flexible films. As shown in Figure 3.5(a), increasing the CNC content decreases the strain gradually. The tensile strength of the composite films shows an initial increase from 155 ± 12 MPa for neat SA to 257 ± 15 MPa for SA-CNC30 (strain 3.4 ± 0.4 %) with the increase of CNC content from 0 to 30 wt%, followed with a subsequent decrease

with the further increase of CNC content. In general, the composite films with CNC contents within 10–70 wt% have higher tensile strength than the neat CNC and SA films, showing the synergistic effect as a result of the ionic interactions between SA and CNCs. In particular, SA-CNC30 films have ca. 66% higher tensile strength relative to the neat SA films. Composite films prepared at high CNC contents (92.5, 95, 97.5 wt%) show similar tensile properties as the neat CNC films with only marginal differences, due to the insufficient SA contents.

Figure 3.5(b) plots the tensile modulus and toughness of the films as functions of CNC content. The modulus shows a general trend of increase with the increase of CNC content from 0 to 70 wt% due to the incorporation of the hard CNCs. Meanwhile, the modulus increase is more significant within the CNC content of 0–20 wt%. On the contrary, the toughness of the films decreases with the increase of the CNC content, due to the decrease in strain at breakage. The neat CNC films have a high modulus of 18.5 ± 1.5 GPa and a toughness of 0.85 ± 0.3 $MJ \cdot m^{-3}$. SA-CNC30 films show a modulus of 14.3 ± 0.5 GPa and a toughness of 5.5 ± 0.9 $MJ \cdot m^{-3}$. Along with the tensile strength, these mechanical properties of SA-CNC30 films approach well to those of nacre-mimicking composites. For example, a poly(vinyl alcohol)-clay-nanofibrillar cellulose artificial nacre was reported to have tensile strength, modulus, and toughness of 302 MPa, 22.8 GPa, and 3.72 $MJ \cdot m^{-3}$.[1] Meanwhile, the tensile strength and toughness of SA-CNC30 films well exceed those of natural nacre (80–135 MPa and 1.8 $MJ \cdot m^{-3}$, respectively), indicating its impressive mechanical performance.

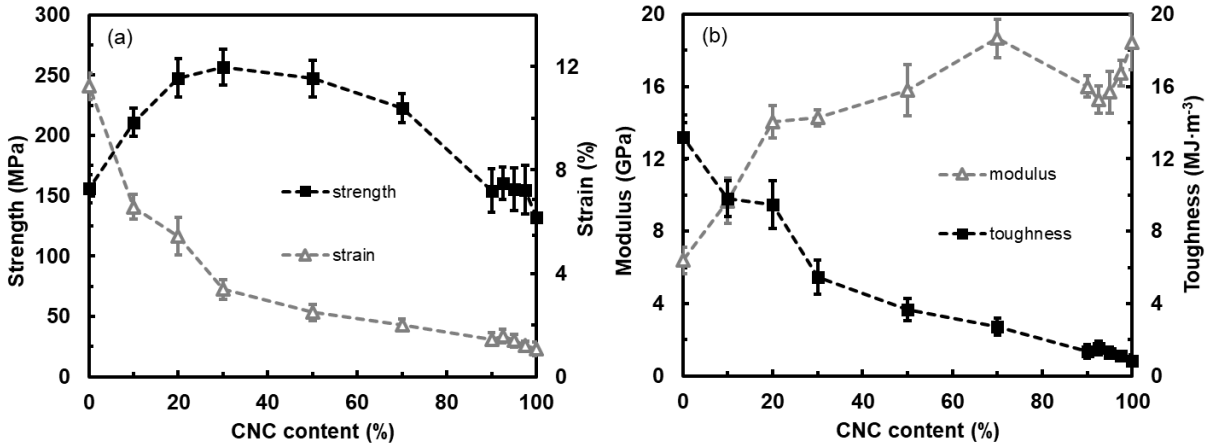

Figure 3.5 Tensile mechanical properties of films of neat CNCs, neat SA and the composites: (a) strength and strain; and (b) modulus and toughness as functions of CNC content.

3.3.5 Calcium Cross-linked SA-CNC30 Composite Films

To further enhance the mechanical properties of composite films, the effect of calcium ion cross-linking on the tensile properties of SA-CNC30 films has been investigated. The addition of calcium ions in SA has been known to result in cross-linking of the anionic polyelectrolyte. The calcium ions interact with the guluronic units on SA and form ionic bridges; the ions are then trapped in the cavities between the chains.[26] For this purpose, several SA-CNC30 films with different degrees of cross-linking were prepared by altering the added amounts of Ca^{2+}, which were dosed based on the mole amount of COO^- in the composites. The Ca^{2+} cross-linked SA-CNC30 composite films are termed as SA-CNC30-#%, with the latter percentage indicating the molar percentage of Ca^{2+} relative to the mole amount of COO^- in the composites.

Figure 3.6(a) shows the UV-vis curves of the various cross-linked SA-CNC30 films. Except SA-CNC30-100%, the curves of all the cross-linked SA-CNC30 films nearly overlap with that of non-cross-linked SA-CNC30 and their transmittance values are high across the whole visible wavelength range. For SA-CNC30-100% treated with an excess amount of calcium, the film transmittance is reduced. Clearly, an excess amount of Ca^{2+} in the films decreases the light transmittance due to the light scattering on free salt crystals inside the film. Figure 3.6(b) shows the ATR-FTIR spectra of the composite films within the wavenumber range of COO^{-} vibration. Small but noticeable left shifts of the two COO^{-} vibration bands (ca. 1600 and 1410 cm^{-1}) can be observed with the increase of Ca^{2+} dosage, verifying the presence of the strong ionic interactions between guluronic units in SA and Ca^{2+}. In particular, the asymmetric stretching vibration band at 1410 cm^{-1} is relatively more sensitive than the symmetric stretching vibration at 1600 cm^{-1}. In addition, the band shifting is more pronounced in the presence of high dosages of $CaCl_2$ (45 and 100%).

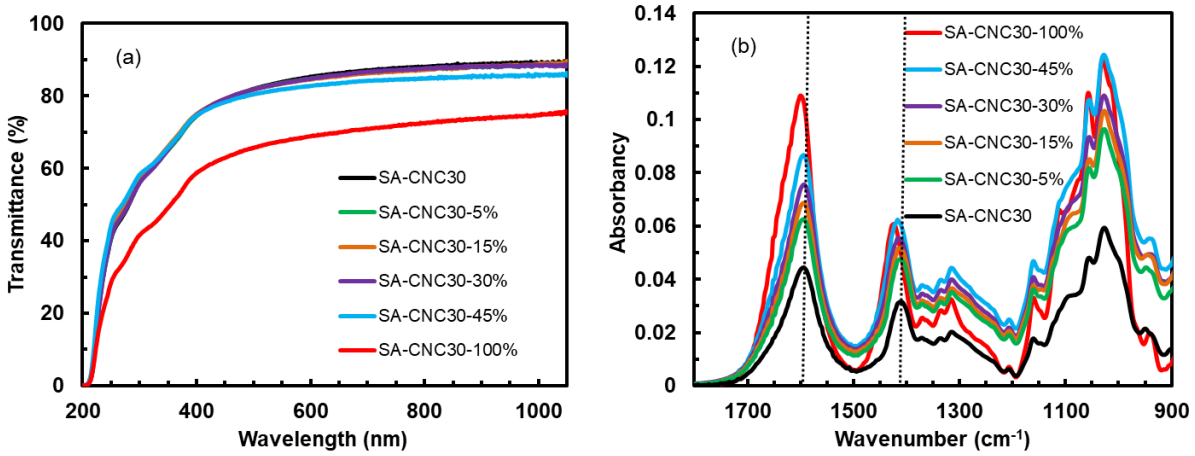

Figure 3.6 (a) UV-vis spectra and (b) FTIR spectra of Ca^{2+} cross-linked SA-CNC30 composites at different Ca^{2+} mole percentages relative to COO^{-} groups present in SA.

The TGA curves of the calcium ion cross-linked films and control SA-CNC30 film are compared in Figure 3.7. The cross-linked films exhibit overall improved thermal stability, with enhanced peak-maximum degradation temperature. While non-cross-linked SA-CNC30 shows the weight loss within the wide temperature range of 40–200 °C due to evaporation of water (free water, bound water).[26] The weight loss in the cross-linked composite films within the same temperature range is appreciably reduced. This indicates the reduced amounts of water present in the cross-linked films. After the removal of water, the main decomposition takes place in the temperature range of 200–350 °C. Nearly all cross-linked films show improved peak-maximum temperatures in the differential TGA curves.

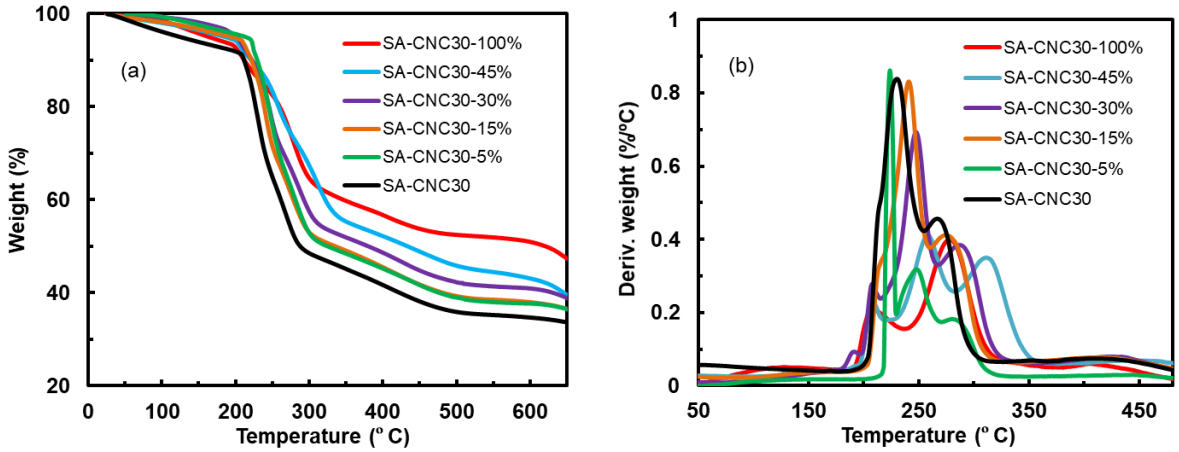

Figure 3.7 (a) TGA curves and (b) differential curves of Ca^{2+} cross-linked SA-CNC30 films and non-cross-linked SA-CNC30 as control.

XRD was performed to analyze the effects of Ca^{2+} cross-linking on the structure of the composites. Figure 3.8 compares the XRD spectra of films of neat CNCs, SA-CNC30, and SA-CNC30-30%. Neat CNC film shows two typical diffraction peaks at 2θ angles of ~15° and ~23°,

respectively, corresponding to the (110) and (200) planes of cellulose crystals.[15] SA-CNC30 containing 30 wt% of SA shows a small peak at ~13.5°, which may result from alginate according to previous studies.[27,28] The intensity of the peak at 15° for the composite film is relatively low with noisy signals compared to the neat CNC film, making the structural elucidation difficult. In the cross-linked film, the peak at ~13.5° is somehow absent, which may be caused by the subtle structural changes after cross-linking.[15,29] Figure 3.9(a) shows the photo of a piece of non-cross-linked SA-CNC30 film soaked in distilled water. After 1 h in water, the film broke into flocs with a gentle touch. On the contrary, the cross-linked SA-CNC30-30% film was swollen but remained as an intact hydrogel chunk, which could be picked out with a pair of tweezers without breakage. After wiped to remove the surface water, the amount of water trapped within the film was measured to be about 27 times of the original dry weight. This also demonstrates the dramatic effect of the Ca^{2+} cross-linking on the structure of the film.

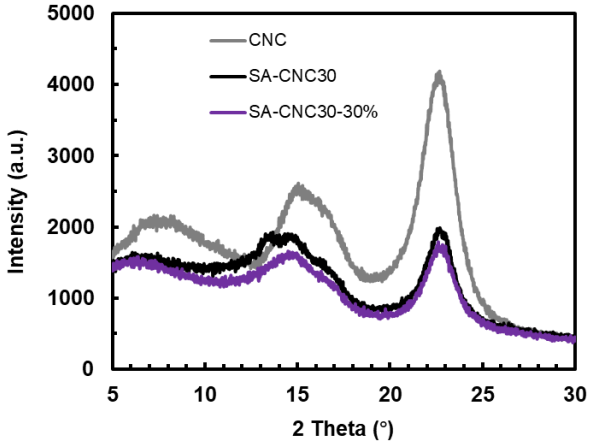

Figure 3.8 XRD patterns of films of neat CNCs, non-cross-linked SA-CNC30, and cross-linked SA-CNC30-30%.

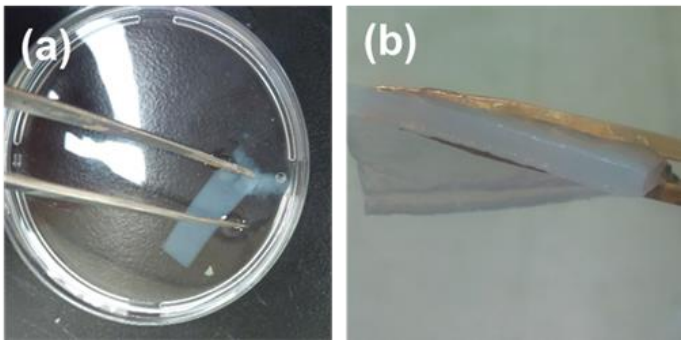

Figure 3.9 Photos of (a) non-cross-linked SA-CNC30 film in water and (b) the cross-linked SA-CNC30-30% film upon soaking in water.

Tensile tests were performed on the Ca^{2+} cross-linked SA-CNC30 films to study the effects of ionic cross-linking on tensile properties of the films. As shown in Figure 3.10, Ca^{2+} cross-linking improves appreciably the tensile strength, modulus, and toughness of the films, with the general positive dependences on the Ca^{2+} dosage in the range of 0 to 30 mol%. But the strain at breakage shows only marginal increases upon the cross-linking. Relative to the non-cross-linked SA-CNC30 film (strength, 257 ± 15 MPa; modulus, 14.3 ± 0.5 GPa; strain, 3.4 ± 0.4 %; toughness, 5.5 ± 0.9 $MJ \cdot m^{-3}$), the cross-linked SA-CNC30-30% films have the strength of 336 ± 36 MPa, modulus of 16.4 ± 1.3 GPa, strain of 4.0 ± 0.6 %, and toughness of 8.7 ± 1.5 $MJ \cdot m^{-3}$. In particular, the strength of CNC30-30% films at the optimum Ca^{2+} dosage is enhanced by 30% and 116% relative to non-cross-linked CNC30 and neat SA films, respectively. These improvements demonstrate the dramatic effects of the cross-linking on the tensile properties and are attributed to the complex structure and relaxation behavior of the multi-component films upon cross-linking.[30] A further increase of the Ca ion dosage to 45 mol%, however, leads to a subsequent moderate decrease in the strength to 323 ± 36 MPa, compared to the SA-CNC30-30%

films, indicative of excessive cross-linking. The cross-linked SA-CNC30-100% films were too brittle to be tested properly.

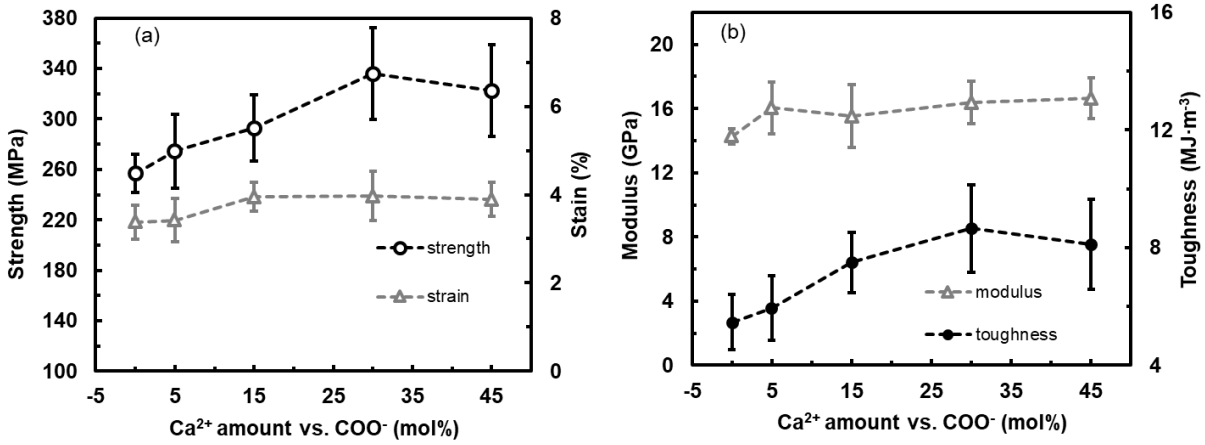

Figure 3.10 Tensile properties of cross-linked SA-CNC30 films at different Ca^{2+} dosages.

3.3.6 Cross-linked SA-CNC30 Composite Films by Different Metal Ions

The SA-CNC30 films were further cross-linked with various other divalent/trivalent metal cations to investigate the effects of ions on the tensile properties of the resulting cross-linked composite films and to screen out the optimum ions. The cross-linking experiments were carried out in the same manner as described above for the use of Ca^{2+}. To prepare divalent cation cross-linked composites, the ratio of cations to the COO^- groups in the composite was set at 30 mol%. However, crisp and curvy films yielded upon the use of trivalent cations at the same ratio after air-drying, indicative of excessive cross-linking. Therefore, a lower cation percentage of 3.5 mol% was applied for the preparation of trivalent cation cross-linked composites. Figure 3.11 summarizes the tensile properties of the resulting cross-linked films. From Figure 3.11(a), the $CaCl_2$ and $MnSO_4$ cross-linked films show the highest strength (336 ± 36 MPa and 349 ± 37 MPa, respectively) followed by the $NiCl_2$ and $CoSO_4$ cross-linked films (329 ± 31 MPa and 330

± 25 MPa, respectively). $CuSO_4$ cross-linked films present the lowest strength among the divalent cation cross-linked films. In terms of toughness, the $CaCl_2$-cross-linked films are the best (8.7 ± 1.5 $MJ \cdot m^{-3}$) among all the cross-linked films. Based on the overall tensile performance of the films, Ca^{2+} is thus the optimum cation for cross-linking.

In a previous work, Konwar et al.[10] also reported that the effect of Ca^{2+} was much greater than Cu^{2+} in the cross-linking of alginate-carbon dot composites. Meanwhile, $MgSO_4$ was found not to promote cross-linking of alginate.[26] However, Mg^{2+} addition was found to promote the aggregation of CNC nanoparticles and render lowered strain due to the reduced mobility of CNC particles.

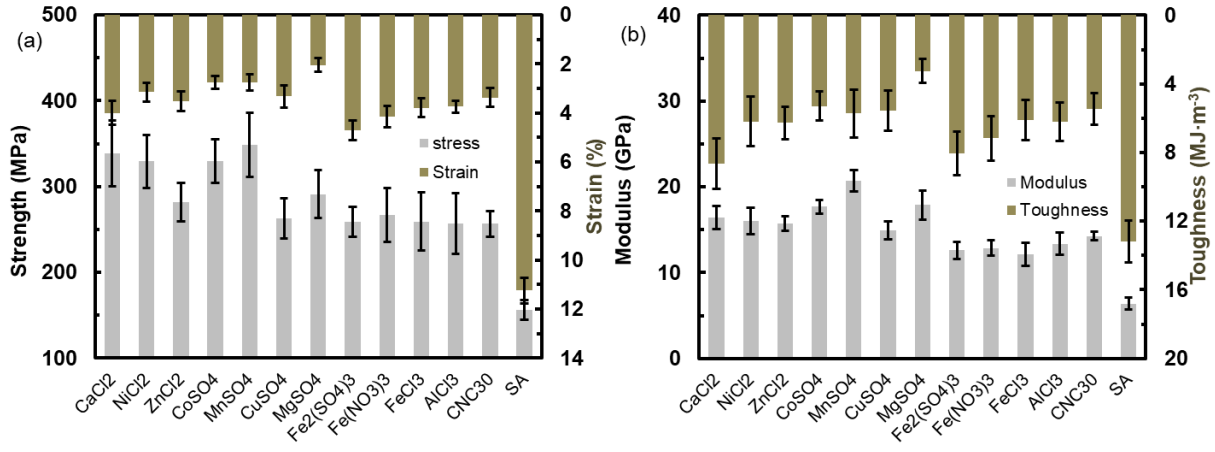

Figure 3.11 Tensile properties of films prepared with various bivalent (30 mol% of COO^- group) and trivalent (3.5 mol% COO^- group) ions.

It is also noticed that the effects of cross-linking with trivalent Al^{3+} and Fe^{3+} at 3.5 mol% are relatively less pronounced than with the divalent cations at 30 mol%. The introduction of trivalent ions slightly increases the tensile strength and strain. The various cation-cross-linked films were also characterized with ATR-FTIR, with similar shifts of the COO^- asymmetric

stretching vibration band at 1410 cm^{-1} also noticed. Figure 3.12 plots the tensile strength with the shifts of the COO^- asymmetric stretching vibration band relative to SA-CNC30. One can see a general trend of the higher composite tensile strength with the increase in the band shift, indicating a correlation between the two. This relationship needs to be further investigated.

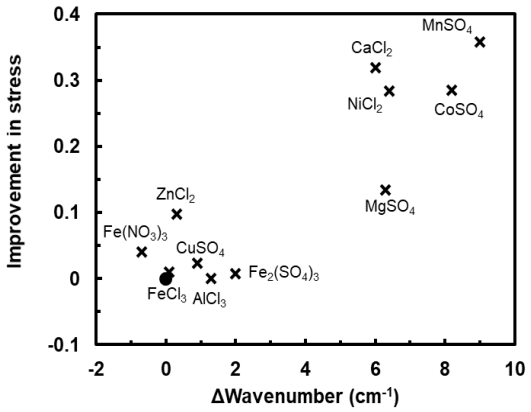

Figure 3.12 Correlation between the improvement in tensile strength and the FTIR shift in the band at 1400 cm^{-1}. Black dot represents non-cross-linked SA-CNC30.

3.4 Conclusions

In this chapter, strong tough nanocomposite films have been prepared from two renewable biopolymers, SA and CNCs. A systematic study on the structure and properties of the SA-CNC composites as well as the effects of metal ion cross-linking has been undertaken. In water dispersion, SA has been found to absorb onto the CNC particles possibly due to the ionic interactions and structural affinity, as revealed by DLS and AFM characterizations. The SA-CNC composite films show improved thermal stability compared to neat SA and CNCs, showing the synergistic effects. Composite films with CNC content ≤ 50 wt% have been found to have good optical transparency. Relative to neat CNC and SA films, tensile tests have shown the

synergistically improved tensile strength for the SA-CNC composite films with the CNC content within 10–70 wt%. In particular, SA-CNC30 shows the best tensile strength of 257 ± 15 MPa, along with high modulus of 14.3 ± 0.5 GPa and high toughness of 5.5 ± 0.9 $MJ \cdot m^{-3}$, which compare well with those of strong tough artificial nacre materials. Moreover, it has been further demonstrated that Ca^{2+} cross-linking helps further improve the tensile properties of SA-CNC30 films, with the Ca^{2+} dosage showing an important effect. Ca^{2+} cross-linked SA-CNC30-30% films with the optimized Ca^{2+} loading at 30 mol% show the tensile strength of 336 ± 36 MPa, modulus of 16.4 ± 1.3 GPa, and toughness of 8.7 ± 1.5 $MJ \cdot m^{-3}$, which exceed the corresponding tensile properties of some well-demonstrated artificial nacre materials. Meanwhile, by screening the effects of cross-linking by various metal ions, Ca^{2+} is demonstrated to be the best one to render most optimum tensile properties.

3.5 References

1. Wang, J.; Cheng, Q.; Lin, L.; Jiang, L. *ACS Nano*, **2014**, *8*, 2739–2745.
2. Podsiadlo, P.; Kaushik, A. K.; Arruda, E. M.; Waas, A. M.; Shim, B. S.; Xu, J.; Nandivada, H.; Pumplin, B. G.; Lahann, J.; Ramamoorthy, A.; Kotov. N. A. *Science*, **2007**, *318*, 80–83.
3. Choo, K.; Ching, Y. C.; Chuah, C. H.; Julai, S.; Liou, N-S. *Materials*, **2016**, *9*, 644.
4. Cao, X.; Dong, H.; Li, C. M. *Biomacromolecules*, **2007**, *8*, 899–904.
5. Smytha, M.; M'Benguea, M-S.; Terriena, M.; Picartc, C.; Brasa, J.; Foster, E. J. *Carbohydr. Polym.*, **2018**, *179*, 186–195.

6. Feng, Y.; Li, X.; Li, M.; Ye, D.; Zhang, Q.; You, R.; Xu, W. *ACS Sustainable Chem. Eng*., **2017**, *5*, 6227–6236.
7. Muiruri, J. K.; Liu, S.; Teo, W. S.; Kong, J.; He. C. *ACS Sustainable Chem. Eng.*, **2017**, *5*, 3929–3937.
8. Wang, B.; Walther, A. *ACS Nano*, **2015**, *9*, 10637–10646.
9. Deepa. B.; Abraham, E.; Pothan, L. A.; Cordeiro, N.; Faria, M.; Thomas, S. *Materials*, **2016**, *9*, 50.
10. Konwar, A; Chowdhury, D. *RSC Adv.*, **2015**, *5*, 62864–62870.
11. Kapishon, V.; Whitney, R. A.; Champagne, P.; Cunningham, M. F.; Neufeld, R. J. *Biomacromolecules*, **2015**, *16*, 2040−2048.
12. Thakur. S.; Pandey, S.; Arotiba. Q. A. *Carbohydr. Polym.*, **2016**, *153*, 34−46.
13. Wang, L-F.; Shankar, S.; Rhim, J-W. *Food Hydrocoll.*, **2017**, *63*, 201−208.
14. Ma, X.; Li, R.; Zhao, X.; Ji, Q.; Xing, Y.; Sunarso, J.; Xia, Y. *Composites: Part A*, **2017,** *96*, 155–163.
15. Huq, T.; Salmieri, S.; Khan, A.; Khan, R. A.; Tien. C. L.; Riedl, B.; Fraschini, C.; Bouchard, J.; Uribe-Calderon, J.; Kamal, M. R.; Lacroix, M. *Carbohydr. Polym.*, **2012**, *90*, 1757–1763.
16. Wu, Q.; Li, X.; Fu, S.; Li, Q.; Wang, S. *Cellulose*, **2017**, *24*, 3255−3264.
17. Cranston, E. D.; Gray, D. G. *Biomacromolecules*, **2006**, *7*, 2522−2530.
18. Cheung, C. C. Y.; Giese, M.; Kelly, J. A.; Hamad, W. Y.; MacLachlan, M. J. *ACS Macro Lett.*, **2013**, *2*, 1016−1020.
19. Zhao, J.; Wei, Z.; Feng, X.; Miao, M.; Sun, L.; Cao, S.; Shi, L.; Fang, J. *ACS Appl. Mater. Interfaces*, **2014**, *6*, 14945−14951.

20. Zhu, H.; Fang, Z.; Wang, Z.; Dai, J.; Yao, Y.; Shen, F.; Preston, C.; Wu, W.; Peng, P.; Jang, N.; Yu, Q.; Yu, Z.; Hu, L. *ACS Nano*, **2016**, *10*, 1369−1377.
21. Sofla, M. R. K.; Brown, R. J.; Tsuzuki, T.; Rainey, T J. *Adv. Nat. Sci.: Nanosci. Nanotechnol.*, **2016**, *7*, 035004.
22. Xiao, Q.; Gu, X.; Tan, S. *Food Chem.*, **2014**, *164*, 179–184.
23. Li, Q.; Zhou, J.; Zhang, L. *J. Polym. Sci. B*, **2009**, *47*, 1069–1077.
24. Soares, J. P.; Santos, J. E.; Chierice, G, O.; Cavalheiro, E. T. G. *Ecl. Quím., São Paulo*, **2004**, *29*, 53−56.
25. Yakimets, I.; Paes, S. S.; Wellner, N.; Smith, A. C.; Wilson, R. H.; Mitchell. J. R. *Biomacromolecules*, **2007**, *8*, 1710−1722.
26. Russo, R.; Malinconico, M.; Santagata, G. *Biomacromolecules*, **2007**, *8*, 3193−3197.
27. Xing, R.; Pan, F.; Zhao, J.; Cao, K.; Gao, C.; Yang, S.; Liu, G.; Wu, H.; Jiang, Z. *RSC Adv.*, **2016**, *6*, 14381–14392.
28. Lin, N.; Bruzzese, C.; Dufresne, A. *ACS Appl. Mater. Interfaces*, **2012**, *4*, 4948−4959.
29. Li, L.; Fang, Y.; Vreeker, R.; Appelqvist, I. *Biomacromolecules*, **2007**, *8*, 464−468.
30. Das, D.; Zhang, S.; Noh, I. *Biomed. Mater.*, **2018**, *13*, 025008.
31. Bertsch, P.; Isabettini, S.; Fischer, P. *Biomacromolecules*, **2017**, *18*, 4060−4066.

Chapter 4

Polycyclopentene Crystal-Decorated Carbon Nanotubes by Convenient Large-Scale In Situ Polymerization and Their Lotus Leaf-Like Superhydrophobic Films

This chapter is adapted from a paper published by L. Xu, L. Huang, Z. Ye, N. Meng, Y. Shu and Z. Gu (Macromol. Rapid. Comm. 2017, 38, 1600608). In this work, L. Xu synthesized the polycyclopentene crystal-decorated MWCNTs by in situ polymerization; L. Huang characterized the composites and prepared composite films as well as their characterization.

Abstract

In situ Pd-catalyzed cyclopentene polymerization in the presence of multi-walled carbon nanotubes (MWCNTs) is demonstrated to effectively render, in a large scale, polycyclopentene (PCP) crystal-decorated MWCNTs. Controlling the catalyst loading and/or polymerization time in the polymerization offers a convenient tuning of the PCP content and the morphology of the decorated MWCNTs. Appealingly, films made of the decorated carbon nanotubes through simple vacuum filtration show the characteristic lotus leaf-like superhydrophobicity featured with high water contact angle (> 150º), low contact angle hysteresis (< 10º), and low water adhesion, while being electrically conductive. This is the first demonstration of the direct fabrication of lotus leaf-like superhydrophobic films with solution-grown polymer crystal-decorated carbon nanotube.

4.1 Introduction

Decoration of carbon nanotubes (CNTs) with polymer crystals is a unique noncovalent strategy for the functionalization of CNTs.[1] In this regard, both single- and multi-walled CNTs (SWCNTs and MWCNTs) have been demonstrated to induce polymer crystallization from their solutions or melts, leading to the formation of nano-hybrid shish-kebab (NHSK) or the transcrystalline structures.[1,2] In particular, the transcrystalline structure forms when the fibrous CNT filler can initiate a high density of active of nuclei on its surface, which force the crystal growth only in the direction normal to the CNT axis. Thus far, the CNT-based transcrystalline structure has only been seen in few cases under appropriate conditions.[3-7] On the contrary, the NHSK structure, first discovered by Li et al.,[8,9] develops at reduced densities of active nuclei, with the CNTs (shish) decorated periodically with polymer crystal lamellae (kebabs). Through quiescent isothermal solution crystallization, CNT-based NHSK structures have been extensively synthesized by Li's and other groups with the use of various semicrystalline polymers,[1] including polyethylene (PE),[8-14] nylon,[8,9,15,16] polypropylene,[17] etc. A size-dependent soft epitaxy mechanism has been proposed by Li et al. for the formation of the NHSK structures.[8,9] Alternatively, other methods, including supercritical CO_2-induced polymer crystallization,[18-20] physical vapor deposition,[21,22] and shear-induced crystallization from polymer melts or solutions,[23-26] have also been developed by various groups for the preparation of CNT-based NHSK structures. The unique NHSK or transcrystalline structure imparts the decorated CNTs with some valuable properties. When used to construct polymer nanocomposites, both NHSK and transcrystalline structures have been demonstrated to render stronger polymer-CNT interactions and facilitate more effective load transfer to the CNTs.[5,16,23,25] Meanwhile, Li et al. have also shown that films made of PE crystal-decorated SWCNTs of the solution-grown NHSK

structure by vacuum filtration exhibit rose petal-like sticky superhydrophobicity due to the hierarchical roughness created by the NHSK structures.[27,28]

All above-mentioned methods for the synthesis of polymer crystal-decorated CNTs (predominantly, NHSK structures) often require special and strict conditions while at small production scale (e.g., high temperature and very dilute polymer solutions at ca. 0.1 $mg \cdot mL^{-1}$) for the periodic epitaxial growth of polymer crystals from the CNTs and the employed semicrystalline polymers must be synthesized beforehand. More convenient one-step large-scale methods, combining polymerization and crystallization in situ in a single step while undertaken at facile conditions, are highly desired. Several groups reported previously the synthesis of PE-CNT nanocomposites by in situ metallocene-catalyzed ethylene polymerization in the presence of CNTs.[29-37] Therein, PE-coated CNTs with sausage-like structures were often produced. The formation of NHSK structures was only observed in few cases,[29,37] but with limited control over the structure and the content of the decorating polymer crystals. Meanwhile, no application was demonstrated with the PE-CNT NHSKs produced therein. In this chapter, a one-step large-scale in situ synthesis of polycyclopentene (PCP) crystal-decorated MWCNTs is reported by convenient, direct Pd-catalyzed polymerization of cyclopentene in the presence of MWCNTs while under facile conditions. PCP is a highly crystalline polymer synthesized by catalytic addition polymerization and is typically featured with high melting point (up to 395 ºC, depending on tacticity).[38] Its use should render beneficially the crystal structures with higher temperature stability compared to PE crystals. However, PCP has not been previously employed to decorate CNTs. Herein, MWCNTs decorated with PCP crystals of high melting point (220 ºC) at tunable content are easily obtained with the in situ polymerization method. More distinctly,

films fabricated with the PCP crystal-decorated MWCNTs are demonstrated to show valuable lotus leaf-like superhydrophobicity.

4.2 Experimental Section

4.2.1 Materials

The MWCNTs used herein were obtained from Aldrich as a product of Arkema Inc., and were directly used without further purification. They were reported by Aldrich to have the external diameter of 10–15 nm, inner diameter of 2–6 nm, length of 0.1–10 μm, average wall thickness of 5–15 graphene layers, and carbon composition of > 90%. The Pd-diimine catalyst employed for the in situ polymerization cyclopentene, [(ArN=C(Me)–(Me)C=NAr)Pd(Me)(N≡CMe)]$^{+}SbF_6^{-}$ (Ar = 2,6-(*i*Pr)$_2$C$_6$H$_3$) (**1**), was synthesized according to a literature procedure.[1] Cyclopentene (96%, Aldrich), chloroform (99%, Aldrich), and methanol (ACS reagent grade, Fisher Scientific) were all used without further purification.

4.2.2 In Situ Polymerization of Cyclopentene in the Presence of MWCNTs

The following is a typical procedure employed for the in situ polymerization of cyclopentene in the presence of pristine MWCNTs. In a N_2-filled glove box, pristine MWCNTs (50 mg) was added into a dried 50 mL-glass flask equipped with a magnetic stirrer. Chloroform (15 mL) was then injected into the tube. The mixture was then sealed and ultrasonicated at ambient temperature for 2 h to form a homogeneous dispersion. Cyclopentene (2.31 g, 0.034 mol) and subsequently a prescribed amount of Pd–diimine catalyst **1** (15–45 mg, dissolved in 5 mL of

chloroform) were injected to start the in situ polymerization. During the course of polymerization, the polymerization temperature was maintained at room temperature with the use of a water bath. After polymerization for a prescribed time, the resulting mixture was transferred into 25 mL of acidified methanol (1%, v/v) and stirred for 30 min to quench the polymerization, followed with vacuum filtration through a 0.22 μm PVDF membrane. The resulting powder was further rinsed with methanol to remove the residual cyclopentene and catalyst residue, and then dried under vacuum at ambient temperature for 8 h, giving the decorated MWCNTs.

A control polymerization in the absence of MWCNTs was also carried out to render the PCP control polymer. An identical procedure as above was used except with the use of catalyst **1** at 35 mg for a polymerization time of 8 h in the absence of MWCNTs. The yield for the control polymer was 535 mg.

4.2.3 Fabrication of Films of Bare MWCNTs and PCP-Decorated MWCNTs

Bare MWCNTs and PCP-decorated MWCNTs were dispersed in toluene at a concentration of 1 $mg \cdot mL^{-1}$. The dispersions were ultrasonicated for ca. 10 min, followed by vacuum filtration through PVDF membranes (0.2 μm). The PVDF-mounted films obtained were rinsed with ethanol for at least 3 times, following with air-drying. The dried films could then peeled off from the PVDF membranes.

4.2.4 Characterizations and Measurements

Thermogravimetric analysis (TGA) was carried out on a TA instrument Q50 thermogravimetric analyzer under nitrogen atmosphere. The samples (ca. 5 mg) were first stabilized at 100 ºC for 10 min, then heated up to 800 ºC at a rate of 20 ºC/min. Differential scanning calorimetry (DSC) analysis was performed on a TA Instruments Q100 DSC equipped with a refrigerated cooling system (RCS) under N_2 atmosphere, with a N_2 purge flow of 50 $mL \cdot min^{-1}$. The samples (ca. 5 mg) were heated from 25 to 280 ºC at 10 ºC/min. Wide angle X-ray diffraction (WAXRD) measurement was done through a Phillips PW1710 diffractometer with Co Kα (40 kV, 30 mA, $\lambda = 1.79$ Å) at room temperature. Transmission electron microscopy (TEM) images were taken on a JEOL 2010F field emission electron microscope operated at 200 keV. The TEM samples were prepared by depositing a few drops of a freshly sonicated dilute dispersion of the MWCNT samples in methanol on holey grids, followed with drying in air. Scanning electron microscopy (SEM) images of the bare and decorated MWCNTs were obtained on a JEOL JSM-7401F field emission scanning electron microscope. The samples were prepared by depositing a few drops of dilute suspensions on a small piece of conductive silicon wafer followed with drying at ambient temperature, which was then mounted to a SEM specimen stub. The nanotube suspensions were ultrasonicated prior to sample preparation. A thin layer of gold (about 5–10 nm) was coated onto the samples using a vacuum sputter coater (Denton Vacuum Desk IV) in order to increase the conductivity and imaging quality. SEM images of the films of bare MWCNTs and PCP-decorated MWCNTs were obtained with a HITACHI S-4700 scanning electron microscope. Film pieces were placed on conductive adhesive tape on the specimen stub. A thin platinum layer was coated onto samples with an ion sputter (HITACHI E-1030).

Electrical conductivity of the films was measured with a 4-probe resistivity measurement system (RTS-8).

Water contact angle measurements of the MWCNT films were carried out on an OCA35 instrument (Dataphysics Instrument GMBH, Germany) with a three-axis horizontal tilt stage using the sessile drop method employing droplets of distilled water. Determination of contact angle was performed using the SCA20 software. The static contact angle was determined as an average of at least five measurements with 2 μL droplets. In dynamic contact angle measurements, advancing contact angles were measured using video recordings of the droplets as the volume was increased upon water injection with a needle. Receding contact angles were found by monitoring the droplets upon extraction of water with the needle. Average values measured from at least 5 tests were used. Droplet sliding angles were obtained by measuring 10 μL droplets as the average of at least 5 repeated tests.

4.3 Results and Discussion

4.3.1 Characterization of Decorated MWCNTs

The in situ polymerization of cyclopentene is undertaken in the presence of MWCNTs with the use of a Pd–diimine catalyst, $[(ArN{=}C(Me){-}(Me)C{=}NAr)Pd(Me)(NCMe)]^{+}SbF_6^{-}$ (Ar = 2,6-$(iPr)_2C_6H_3$) **(1)**, simply at room temperature (ca. 23 ºC) under N_2 with mild magnetic stirring. Scheme 4.1 depicts schematically this in situ polymerization method. As a unique class of late transition metal catalysts,[39] Pd–diimine catalysts similar to **1** have been previously demonstrated to produce cis-1,3-enchained high-molecular-weight PCP with high melting point of ca. 240 ºC at similar conditions.[40] In this polymerization system, the feed concentrations of MWCNTs and

cyclopentene are fixed at 2.5 and 115 mg·mL^{-1}, respectively, in a fixed volume (20 mL) of chloroform as solvent. This feed concentration of MWCNTs is much higher compared to those typically used in the small-scale isothermal solution crystallization method,[8-16] thus facilitating the more effective larger-scale synthesis herein. The loading amount of catalyst **1** and the polymerization time are the parameters that are tuned in the system to change the structure of resulting PCP crystal-decorated MWCNTs, including the content of PCP crystals and the morphology. An increase of either one, while at otherwise identical conditions, should lead to the enhanced PCP yield in the polymerization.

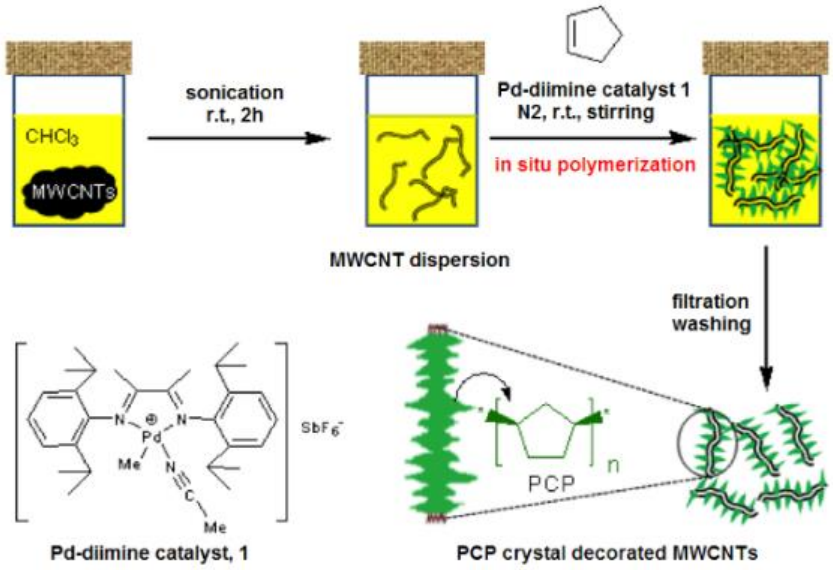

Scheme 4.1 Pd-catalyzed cyclopentene polymerization in the presence of MWCNTs for the in situ synthesis of PCP crystal-decorated MWCNTs.

The effect of the loading amount of **1** on the resulting PCP-decorated MWCNTs was first investigated. Polymerization runs were carried out at different catalyst loading (15, 25, 35, and 45 mg, respectively) with the same reaction time (72 h). Figure 4.1 shows the transmission

electron microscopy (TEM) images of the resulting decorated MWCNTs (termed as d-MWCNT1, d-MWCNT2, d-MWCNT3, and d-MWCNT4, respectively). Figure 4.2 shows their scanning electron microscopy (SEM) images, along with that of bare MWCNTs. A control run was also undertaken in the absence of MWCNTs at the catalyst loading of 35 mg, rendering neat PCP. Figure 4.3 shows the SEM and TEM images of the neat PCP. Thermogravimetric analysis (TGA, see Figure 4.4) shows that the four decorated MWCNT samples have a PCP content of 10, 68, 79, and 89 wt%, respectively, as per the weight loss at 600 ºC since bare MWCNTs have negligible weight loss at 600 ºC while neat PCP produced in the control run has the complete weight loss by 600 ºC.

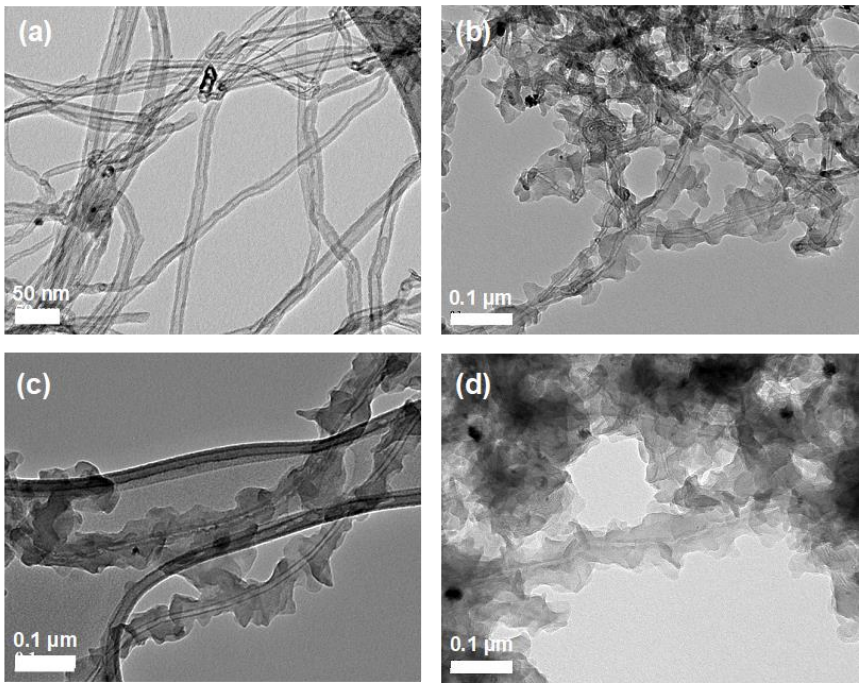

Figure 4.1 TEM images of (a) d-MWCNT1, (b) d-MWCNT2, (c) d-MWCNT3, (d) d-MWCNT4 produced at the catalyst **1** loading of 15, 25, 35, 45 mg, respectively.

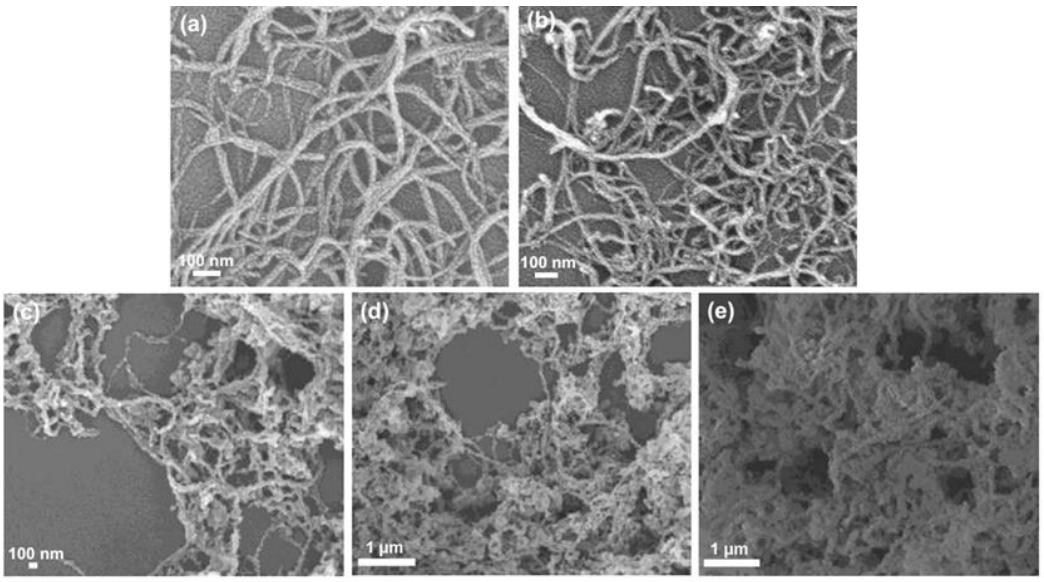

Figure 4.2 SEM images of (a) bare MWCNTs, (b) d-MWCNT1, (c) d-MWCNT2, (d) d-MWCNT3, (e) d-MWCNT4.

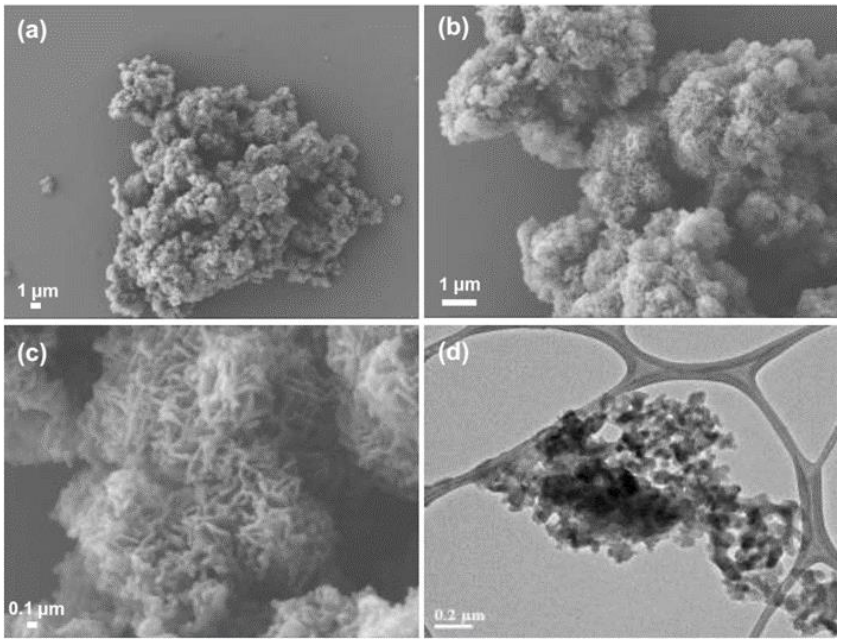

Figure 4.3 (a)–(c) SEM images of neat PCP produced in the absence of MWCNTs at different magnifications; (d) TEM image of neat PCP.

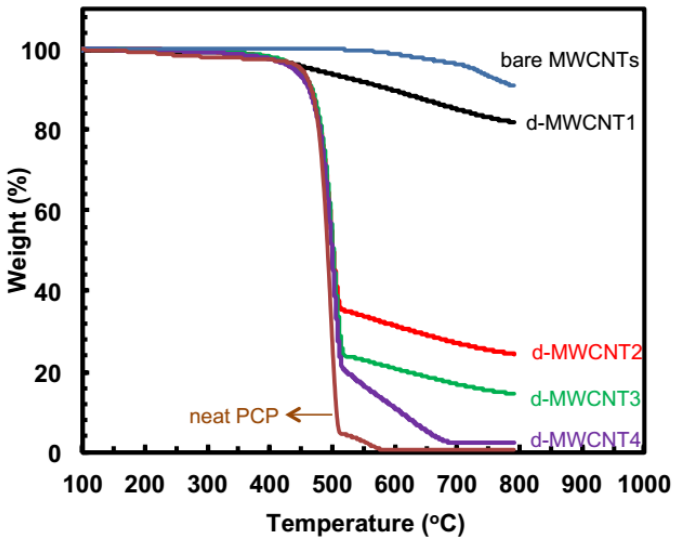

Figure 4.4 TGA curves of the decorated MWCNTs, along with those of bare MWCNTs and neat PCP.

Due to its low PCP content, d-MWCNT1, produced at the lowest catalyst loading among the four, does not show significant difference in terms of nanotube morphology compared to the bare MWCNTs from the TEM and SEM images, with no clear observation of the PCP decoration on the nanotubes within the resolution limit. PCP likely forms a thin layer around the MWCNTs in this sample, which is not clearly visible under TEM or SEM. On the contrary, all the nanotubes in the d-MWCNT2, d-MWCNT3, and d-MWCNT4 are clearly decorated with PCP (see Figure 4.1). Their morphology resembles the typical NHSK structures prepared by isothermal solution crystallization of PE or nylon on CNTs, with the MWCNTs serving as the shish and the decorated PCP of various irregular shapes as kebabs. Meanwhile, large agglomerates formed purely of PCP are not seen. With the increase of PCP content from d-MWCNT2 to d-MWCNT4, the quantity of PCP kebabs appears to gradually increase. While there are locations on the nanotubes not decorated by the PCP kebabs in d-MWCNT2, all the

nanotubes in d-MWCNT4 appear to be fully decorated and the kebabs are bigger, approaching to resemble the transcrystalline structures.[3-7] The morphology of these decorated MWCNTs is distinctively different from that of neat PCP. The neat PCP appears as loose aggregates of finer particles with a coral-like surface morphology of abundant patterned roughness (see Figure 4.3).

In PE-CNT NHSK structures produced by isothermal solution crystallization, the PE crystals often form orthogonal disc-shaped lamellae decorating periodically the CNTs.[8-14] In comparison, the shape of the PCP kebabs herein is relatively irregular, with no disc-shaped lamellae observed. Meanwhile, the lateral thickness of the PCP kebabs is at about 100 nm, with no well-defined periodicity. The irregular NHSK structures seen here are reasoned to result from the much faster crystallization kinetics in this in situ polymerization system in comparison with the slow isothermal solution crystallization. The driving force for polymer crystallization is the free-energy change involved in the phase transformation and is proportional to the supercooling, ΔT defined as $\Delta T = T_m - T_c$, with T_m and T_c denoting the melting and crystallization temperatures, respectively.[8,9] Herein, T_m of the PCP crystals is much higher than that of PE crystals while T_c (room temperature herein) is much lower than that (ca. 100 ºC) typically employed for the isothermal solution crystallization of PE. The much greater ΔT herein accounts for the relatively irregular PCP crystal morphology on MWCNTs. Additionally, the surface defects on MWNCTs may also contribute to the irregular NHSK structures. Such NHSK structures with irregular polymer crystal morphology have been commonly observed in crystallization systems involving higher supercooling, such as nylon-CNT NHSKs prepared by isothermal solution crystallization[8-16] and physical vapor deposition,[21,22] PE-CNT NHSKs prepared by CO_2-induced solution crystallization,[18-20] and PE-CNT NHSKs prepared by in situ polymerization.[29,37]

The evolution of the NHSK structures during the course of an in situ polymerization run carried out at the catalyst loading of 35 mg was further investigted. Figure 4.5 shows the TEM images of the resulting PCP-decorated MWCNTs (termed as d-MWCNT5 to d-MWCNT8, respectively) sampled after the different polymerization time of 1.5, 5, 8, and 15 h, respectively, from the run. According to their TGA weight loss at 600 ºC (see Figure 4.6), the four samples have a PCP content of 31, 56, 67, and 73 wt%, respectively. The increasing PCP content upon the extension of polymerization time confirms the continuous conversion of cyclopentene into PCP over the course of polymerization as expected. As shown in Figure 4.5(a), no shish-kebab structures are observed in d-MWCNT5. From the inset in Figure 4.5(a) at a higher magnification, the MWCNTs appear to be coated with a non-uniform layer of PCP having a thickness up to ca. 6 nm. This indicates that, at the early stage of polymerization, the produced PCP is adsorbed onto the nanotubes as a surrounding layer. From Figure 4.6(b), small polymer kebabs (see circled areas) decorated on the nanotubes can be found in d-MWCNT6 produced at 5 h. The further extension of the polymerization to 8 and 15 h leads to the gradual enlargement of the kebabs and meanwhile the growth of more kebabs (see Figures 4.5(c) and (d)). This trend of morphology evolution resembles that of NHSK structures, but differs from that of transcrystalline structures. Similar evolution of NHSK structures was previously observed in CO_2-induced PE epitaxy[18] and PE non-isothermal solution crystallization in the presence of MWCNTs.[41] In the case of transcrystalline structures, the morphology evolution is very different: the transcrystalline layer of isotactic polypropylene on CNT fibers was observed to grow uniformly along the entire fiber axial length even in the very beginning of crystallization and the extension of time just led to the gradual thickening of the layer.[3]

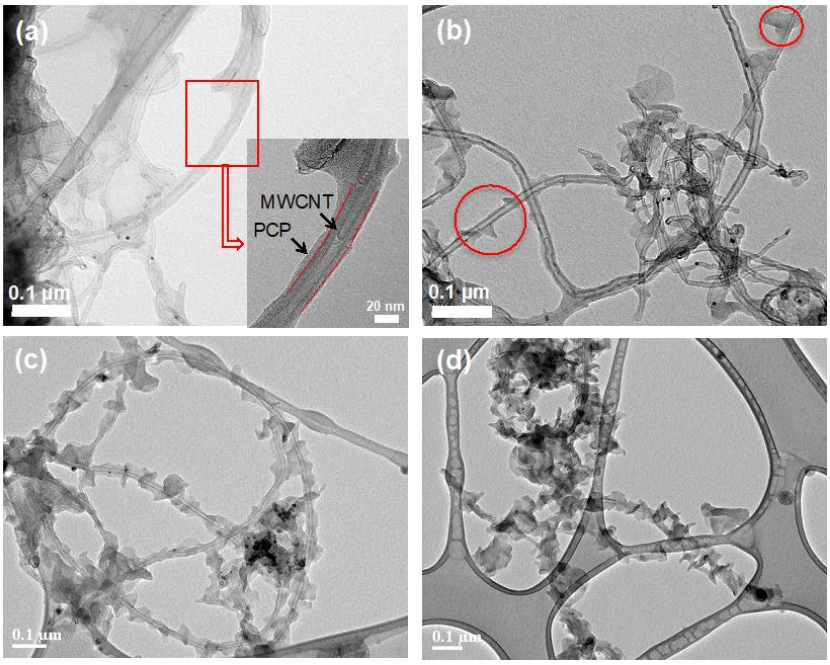

Figure 4.5 TEM images of decorated-MWCNTs (d-MWCNT5 to d-MWCNT8, respectively) collected at different polymerization time of 1.5 h (a), 5 h (b), 8 h (c), and 15 h (d) in the in situ polymerization with 35 mg of catalyst **1**.

In this unique in situ polymerization system, polymer production and crystallization occur simultaneously. The polymer chains, once produced, are reasoned to undergo fast crystallization given the large supercooling, *i.e.*, polymerization as the rate-controlling step for the crystal formation. From the trend shown in Figure 4.5, the PCP chains produced in the beginning of the polymerization precipitate and adsorb on the MWCNTs forming a surrounding layer, which serves as heterogeneous nucleation sites for subsequent epitaxial growth of the lamellae. From the increasing number of PCP kebabs over time seen in the TEM images, it is also reasoned that crystal nucleation on MWCNTs continues to occur during the course of polymerization. Along with epitaxial growth of the crystal lamellae, new nuclei may

simultaneously form elsewhere. This also contributes to the relatively irregular PCP kebabs observed herein.

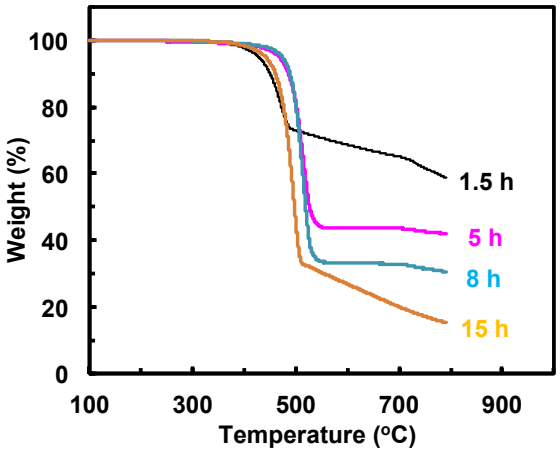

Figure 4.6 TGA curves of decorated MWCNTs (d-MWCNT5, d-MWCNT6, d-MWCNT7, and d-MWCNT8) produced at different polymerization time (1.5, 5, 8, and 15 h, respectively) with catalyst **1** loading of 35 mg.

Figure 4.7 shows the X-ray diffraction (XRD) pattern of d-MWCNT7 as a representative sample, along with those of bare MWCNTs and neat PCP for comparison. The neat PCP shows a broad XRD peak from 13 to 26º with peak maximum at 19.9º, which is typical of cis-enchained PCP produced with Pd– and Ni–diimine catalysts.[40] The bare MWCNTs show a characteristic broad peak from 24 to 32º, with peak maximum at 28.8º.[42] The diffraction pattern of d-MWCNT7 is superimposed by the peaks of neat PCP and bare MWCNTs. Figure 4.8(a) shows differential scanning calorimetry (DSC) first heating curves of the nascent d-MWCNTs, along with that of neat PCP. The curves are baseline corrected (Universal Analysis 2000). Due to the low PCP content, the curves for both d-MWCNT1 and d-MWCNT5 are nearly featureless. Neat PCP has a broad melting endotherm up to ca. 256 ºC with peak maximum at 224 ºC. The d-

MWCNT samples instead show narrowed melting endotherms (up to about 235 ºC) with slightly lowered peak maximum temperatures (196–216 ºC). The slightly lowered peak maximum temperatures are indicative of the slightly thinner lamella in the d-MWCNTs than the neat PCP. Figure 4.8(b) illustrates the subsequent DSC cooling curves of the samples. The neat PCP shows a broad crystallization exotherm covering nearly the entire temperature window (from 270 to ca. 50 ºC) with peak maximum at 192 ºC. Such broad melting and crystallization peaks are indicative of broad tacticity distribution within the neat PCP chains. Like their corresponding melting endotherms, the crystallization exotherms of the d-MWCNT samples are also much narrower with the peak maximum at about 191–203 ºC. With the increase of the PCP content, the peak maximum temperature of the d-MWCNT samples in both heating and cooling curves shows only small marginal changes.

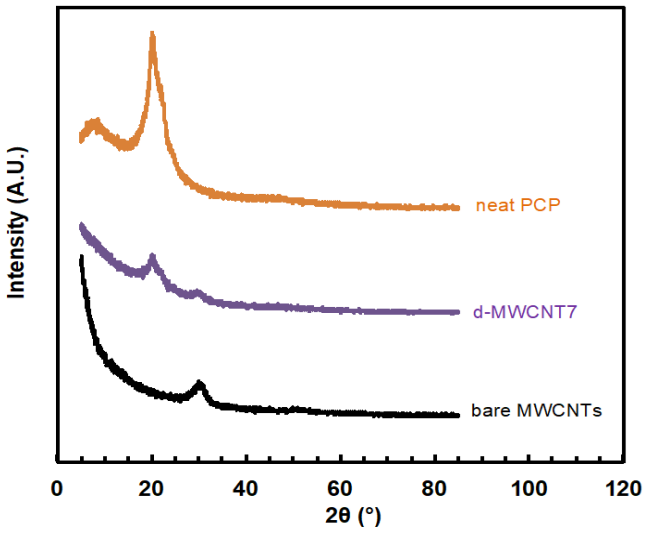

Figure 4.7 XRD patterns of d-MWCNT7, neat PCP, and bare MWCNTs.

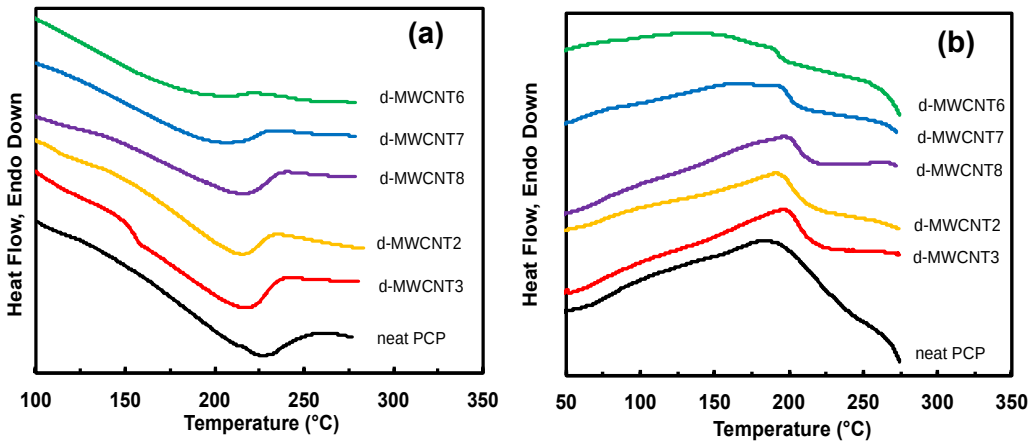

Figure 4.8 DSC 1st-heating (a) and cooling curves (b) of the d-MWCNTs and neat PCP.

4.3.2 Characterization of Films Fabricated by Decorated MWCNTs

Following their convenient successful synthesis, the above PCP-decorated MWCNTs are demonstrated for the fabrication of lotus leaf-like superhydrophobic films. CNT films are known for their exceptional mechanical and electrical properties.[43] Superhydrophobic CNT films endowed with additional superhydrophobic surface properties by controlling their surface roughness and functionality are valuable for various applications.[44,45] Simple, convenient techniques for rendering superhydrophobic CNTs films are highly desired. With the use of PE-SWCNT NHSKs prepared by isothermal solution crystallization, Li et al. first demonstrated the fabrication of rose petal-like sticky superhydrophobic CNT films.[27,28] Therein, the films were featured with high static water contact angle (up to 152º) but large contact angle hysteresis (115º) and high water surface adhesion. Nevertheless, lotus leaf-like superhydrophobic CNT films with characteristic high water contact angle (> 150º), low contact angle hysteresis (< 10º), and low water adhesion have not been previously reported yet with the simple, direct use of solution-

grown polymer crystal-decorated CNTs. Though Li et al. subsequently reported that surface coating of the solution-grown PE-SWCNT NHSKs with polytetrafluoroethylene by chemical vapor deposition rendered films with lotus-leaf like superhydrophobicity and electrical field-induced, reversible lotus-to-rose transition,[46] the requirement of additional surface coating makes their procedure inconvenient.

Herein, films with the thickness in the range of 50–100 μm have been conveniently prepared with three representative PCP crystal-decorated MWCNTs (d-MWCNT1 to d-MWCNT3) and the bare MWCNTs, respectively, through the simple vacuum filtration method. Figure 4.9 illustrates the SEM images of the top surface of the films, along with their wetting behavior determined with the sessile drop technique. The nanotubes in bare MWCNTs and d-MWCNT1 show relatively smooth surface. In the case with d-MWCNT1, this should result from the low content of PCP coating. On the contrary, the nanotubes in d-MWCNT2 and d-MWCNT3 are clearly covered by an irregular, rough layer of PCP coating. The film prepared with bare MWCNTs has a contact angle of 93º, which is close to the typical value of 82º reported for films of SWCNT films and graphite.[27,28] Meanwhile, a film of the neat PCP shows a hydrophobic surface with an intrinsic contact angle of 122º. On the contrary, the films fabricated with the decorated MWCNTs show significantly enhanced contact angles (155, 152, 154º, respectively) with no clear dependence on the PCP content. In particular, it is surprising to see that the film of d-MWCNT1 is also featured with high contact angle (155º) despite its low PCP content. In agreement with the above TEM evidence seen in Figure 4.1, this further confirms that the low content of PCP is coated effectively on the nanotubes.

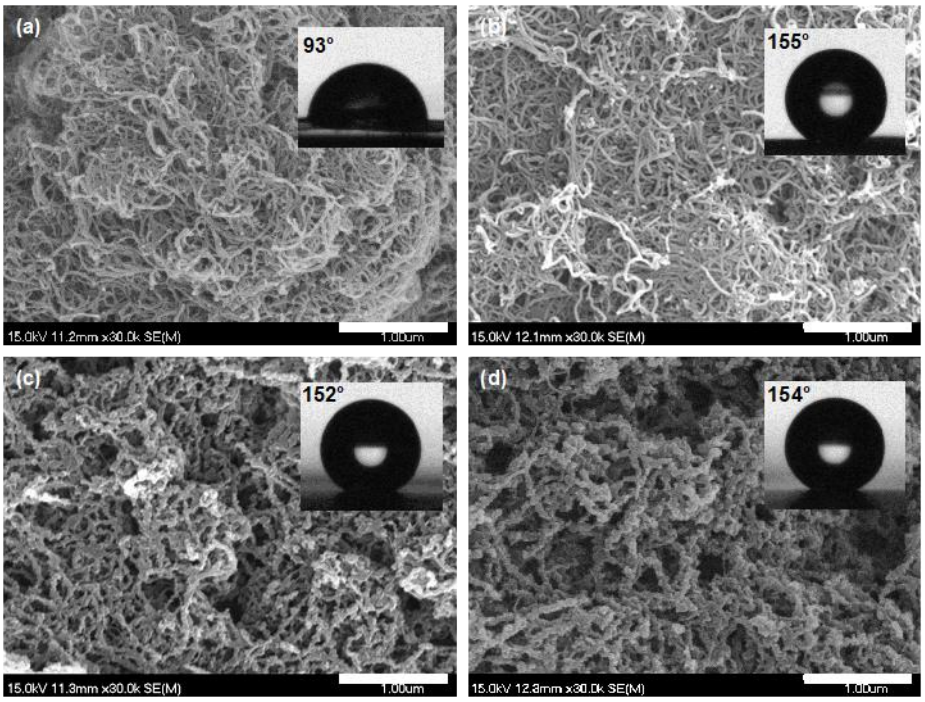

Figure 4.9 SEM images of films prepared with (a) bare MWCNTs, (b) d-MWCNT1, (c) d-MWCNT2, (d) d-MWCNT3. Inset images are 2 μL water droplets on the surface of the films with contact angle values.

The dynamic (advancing and receding) contact angles of the films were also determined. The advancing contact angles of the films of the three d-MWCNTs are 152, 146, 148º, respectively; the receding contact angles are 141, 136, 140º, respectively, indicative of very small hysteresis (8–11º). The sliding angles at which water droplets roll off the films are 8, 9, and 10º, respectively. These results confirm the lotus leaf-like, superhydrophobic, low-water-adhesion surface (the Cassie-Baxter state) of the films fabricated with the PCP-decorated MWCNTs.[47] This unique superhydrophobic surface should result from the change in surface functionality and the hierarchical nanoscale surface roughness created upon the decoration of the MWCNTs with PCP crystals through the in situ polymerization. These films are distinctively

different from the rose petal-like superhydrophobic high-water-adhesion films made with PE-CNT NHSK structures by Li et al.[27,28] Though the precise mechanism is to be investigated in further study, the difference between the two types of films is reasoned to stem from the different decorating polymer and nanoscale surface roughness.

Because of their MWCNT skeletons, the superhydrophobic films of the PCP-decorated MWCNTs are also electrically conductive. While the film of bare MWCNTs has a conductivity of 378 s/m, the films of the three d-MWCNTs show reduced conductivity values of 222, 0.28, and 0.13 s/m, respectively, due to the increasing content of the non-conducting PCP. Tuning the content of the decorating PCP by changing the loading amount of catalyst **1** or polymerization time in the in situ polymerization can thus effectively adjust the electrical conductivity of the superhydrophobic films fabricated with this range of decorated MWCNTs.

4.4 Conclusions

A simple, convenient in situ polymerization method under facile conditions is demonstrated for the large-scale synthesis of PCP crystal-decorated MWCNTs with tunable PCP content and morphology. It is further discovered that the decorated MWCNTs can render electrically conductive films featured with valuable lotus leaf-like superhydrophobicity simply via vacuum filtration. The potential applications of these films in areas such as sensors, electrochemical devices, and coating, are anticipated.

4.5 References

1. Laird, E. D.; Li, C. Y. *Macromolecules*, **2013**, *46*, 2877–2891.
2. Xu, J-Z.; Zhong, G-J.; Hsiao, B. S.; Fu, Q.; Li, Z-M. *Prog. Polym. Sci.*, **2014**, *39*, 555–593.
3. Zhang, S.; Minus, M. L.; Zhu, L.; Wong, C-P.; Kumar, S. *Polymer*, **2008**, *49*, 1356–1364.
4. Zhang, S.; Lin, W.; Zhu, L.; Wong, C-P.; Bucknall, D. G. *Macromol. Chem. Phys.*, **2010**, *211*, 1348–1354.
5. Zhang, S.; Lin, W.; Wong, C-P.; Bucknall, D. G.; Kumar, S. *ACS Appl. Mater. Interfaces*, **2010**, *2*, 1642–1647.
6. Miltner, H. E.; Grossiord, N.; Lu, K.; Loos, J.; Koning, C. E.; van Mele, B. *Macromolecules*, **2008**, *41*, 5753–5762.
7. Lu, K.; Grossiord, N.; Koning, C. E.; Miltner, H. E. van Mele, B. *Macromolecules*, 2**008**, *41*, 8081–8085.
8. Li, C. Y.; Li, L.; Cai, W.; Kodjie, S. L.; Tenneti, K. K. *Adv. Mater.*, **2005**, *17*, 1198–1202.
9. Li, L.; Li, C. Y.; Ni, C. *J. Am. Chem. Soc.*, **2006**, *128*, 1692–1699.
10. Uehara, H.; Kato, K.; Kakiage, M.; Yamanobe, T.; Komoto, T. *J. Phys. Chem. C*, **2007**, *111*, 18950–18957.
11. Zhang, S.; Lin, W.; Yu, X.; Wong, C-P.; Cheng, S. Z. D.; Bucknall, D. G. *Macromol. Chem. Phys.*, **2010**, *211*, 1003–011.
12. Zhang, S.; Lin, W.; Wong, C-P.; Bucknall, D. G.; Kumar, S. *ACS Appl. Mater. Interfaces*, **2010**, *2*, 1642–1647.
13. Wang, W.; Li, C. Y. *ACS Macro Lett.*, **2012**, *1*, 175–179.

14. Liang, G.; Zheng, L.; Bao, S.; Fei, B.; Gao, H.; Zhu, F.; Wu, Q. *Macromolecules*, **2015**, *48*, 4115–4121.
15. Li, L.; Li, C. Y.; Ni, C.; Rong, L.; Hsiao, B. *Polymer*, **2007**, *48*, 3452–3460.
16. Nie, M.; Kalyon, D. M.; Fisher, F. T. *ACS Appl. Mater. Interfaces*, **2014**, *6*, 14886–14893.
17. Ning, N.; Zhang, W.; Zhao, Y.; Tang, C.; Yang, M.; Fu, Q. *Polymer*, **2012**, *53*, 4553–4559.
18. Yue, J.; Xu, Q.; Zhang, Z.; Chen, Z. *Macromolecules*, **2007**, *40*, 8821–8826.
19. Zhang, Z.; Xu, Q.; Chen, Z.; Yue, J. *Macromolecules*, **2008**, *41*, 2868–2873.
20. Zhang, F.; Zhang, H.; Zhang, Z.; Chen , Z.; Xu, Q. *Macromolecules*, **2008**, *41*, 4519–4523.
21. Li, L.; Yang, Y.; Yang, G.; Chen, X.; Hsiao, B. S.; Chu, B.; Spanier, J. E.; Li, C. Y. *Nano Lett.*, **2006**, *6*, 1007–1012.
22. Li, L.; Li, B.; Yang, G.; Li, C. Y. *Langmuir*, **2007**, *23*, 8522–8525.
23. Ning, N.; Fu, S.; Zhang, W.; Chen, F.; Wang, K.; Deng, H.; Zhang, Q.; Fu, Q. *Prog. Polym. Sci.*, **2012**, *37*, 1425–1455.
24. Ning, N.; Luo, F.; Pan, B.; Zhang, Q.; Wang, K.; Fu, Q. *Macromolecules*, **2007**, *40*, 8533–8536.
25. Yang, J.; Wang, C.; Wang, K.; Zhang, Q.; Chen, F.; Du, R.; Fu, Q. *Macromolecules*, **2009**, *42*, 7016–7023.
26. Minus, M. L.; Chae, H. G.; Kumar, S. *ACS Appl. Mater. Interfaces*, **2012**, *4*, 326–330.
27. Laird, E. D.; Wang, W.; Cheng, S.; Li, B.; Presser, V.; Dyatkin, B.; Gogotsi, Y.; Li, C. Y. *ACS Nano*, **2012**, *6*, 1204–1213.
28. Laird, E. D.; Qi, H.; Li, C. Y. *Polymer*, **2015**, *70*, 271–277.

29. Bonduel, D.; Bredeau, S.; Alexandre, M.; Monteverde, F.; Dubois, P. *J. Mater. Chem.*, **2007**, *17*, 2359–2366.

30. Trujillo, M.; Arnal, M. L.; Müller, A. J.; Laredo, E.; Bredeau, S.; Bonduel, D.; Dubois, P. *Macromolecules*, **2007**, *40*, 6268–6276.

31. Toti, A.; Giambastiani, G.; Bianchini, C.; Meli, A.; Bredeau, S.; Dubois, P.; Bonduel, D.; Claes, M. *Chem. Mater.*, **2008**, *20*, 3092–3098.

32. Park, S.; Yoon, S. W.; Choi, H.; Lee, J. S.; Cho, W. K.; Kim, J.; Park, H. J.; Yun, W. S.; Choi, C. H.; Do, Y.; Choi, I. S. *Chem. Mater.*, **2008**, *20*, 4588–4594.

33. Park, S.; Choi, I. S. *Adv. Mater.*, **2009**, *21*, 902–905.

34. Kim, J.; Hong, S. M.; Kwak, S.; Seo, Y. *Phys. Chem. Chem. Phys.*, **2009**, *11*, 10851–10859.

35. Kim, J.; Kwak, S.; Hong, S. M.; Lee, J. R.; Takahara, A.; Seo, Y. *Macromolecules*, **2010**, *43*, 10545–10553.

36. Ravasio, A.; Boggioni, L.; Tritto, I.; D'arrigo, C.; Perico, A.; Hitzbleck, J.; Okuda, J. *J. Polym. Sci., Part A: Polym. Chem.*, **2009**, *47*, 5709–5719.

37. Bahuleyan, B. K.; Atieh, M. A.; De, S. K.; Khan, M. J.; Al-Harthi, M. A. *J. Polym. Res.*, **2012**, *19*, 9744.

38. Kaminsky, W.; Bark, A.; Spiehl, R.; Möller-Lindenhof, N.; Niedoba, S. *Transition Metals and Organometallics as Catalysts for Olefin Polymerization, (Eds: W. Kaminsky, H. Sinn), Springer-Verlag, Berlin, Heidelberg*, **1988**, p. 291.

39. Ye, Z.; Xu, L.; Dong, Z.; Xiang P. *Chem. Commun.*, **2013**, *49*, 6235–6255.

40. McLain, S. J.; Feldman, J.; McCord, E. F.; Gardner, K. H.; Teasley, M. F.; Coughlin, E. B.; Sweetman, K. J.; Johnson, L. K.; Brookhart, M. *Macromolecules*, **1998**, *31*. 6705–6707.

41. Zhang, L.; Tao, T.; Li, C. *Polymer* **2009**, *50*, 3835–3840.

42. Xu, L.; Ye, Z.; Cui, Q.; Gu, Z. *Macromol. Chem. Phys.*, **2009**, *210*, 2194–2202.

43. de Heer, W. A.; Bacsa, W. S.; Châtelain, A.; Gerfin, T.; Humphrey-Baker, R.; Forro, L.; Ugarte, D. *Science*, **1995**, *268*, 845–847.

44. Lau, K. K. S.; Bico, J.; Teo, K. B. K.; Chhowalla, M.; Amaratunga, G. A. J.; Milne, W. I.; McKinley, G. H.; Gleason, K. K. *Nano Lett.*, **2003**, *3*, 1701–1705.

45. Kakade, B. A. *Nanoscale*, **2013**, *5*, 7011–7016.

46. Laird, E. D.; Bose, R. K.; Qi, H.; Lau, K. K. S.; Li, C. Y. *ACS Appl. Mater. Interfaces*, **2013**, *5*, 12089–12098.

47. Feng, X. J.; Jiang, L. *Adv. Mater.*; **2006**, *18*, 3063–3078.

Chapter 5

Effects of Ligands on Catalytic Performance of Palladium Nanocatalysts in Selective Hydrogenation of Phenylacetylene and Diphenylacetylene

Abstract

Selective hydrogenation of alkynes to alkenes facilitated by Pd nanocatalysts is an important chemical transformation with extensive industry applications. To enhance the catalytic selectivity, small molecular ligands are often used to modify the catalytic active centers of the nanocatalysts. To date, a variety of ligands has been employed. Though individually shown effective, their effects on the performance of the nanocatalysts have not yet been compared. To identify the best ligands for achieving optimum performance in the selective hydrogenation, a systematic study has been conducted in this chapter to evaluate the effects of various ligands (including quinoline, pyridine, dimethyl sulfoxide (DMSO), 3,6-dithia-1,8-octanediol (DTO), and triphenylphosphine) on the selectivity and activity of selective hydrogenation of phenylacetylene (PA) and diphenylacetylene (DPA). Three Pd nanocatalysts have been employed for this investigation, including a colloidal hyperbranched polyethylene ionomer supported Pd catalyst, and commercial Lindlar and Pd@C catalysts. An order of efficiency of the ligands has been established, DTO > triphenylphosphine > DMSO > quinoline > pyridine. Sulfur-containing DTO shows the best performance in facilitating the highly selective hydrogenation of both alkynes while requiring the lowest dosages.

5.1 Introduction

Catalytic selective hydrogenation (or called semi-hydrogenation) of alkynes to alkenes is an important chemical transformation widely used for synthesis of alkenes as building blocks for synthesis of fine chemicals, and for the removal of trace alkyne impurities from alkene monomer stocks (such as ethylene, propylene, styrene, etc.) in polymer production.[1,2] While a variety of transition metal-based nanocatalysts have been reported, heterogeneous Pd nanocatalysts, where Pd nanoparticles (size < ca. 10 nm) are immobilized on various supports, have been considered as the most active, most selective, and most commonly used catalysts for selective alkyne hydrogenation.[3] The classical Lindlar catalyst (Pd nanoparticles supported on $CaCO_3$ modified with Pb and/or quinoline) developed in 1952 is the prototypic example of Pd nanocatalysts and remains in widespread use in industrial processes.[4]

The main goal in selective alkyne hydrogenation is to maximize the selectivity of desired alkenes by minimizing the unwanted over-hydrogenated alkanes and possible alkene isomers while at maintained high catalyst activity. However, avoiding over-hydrogenation is challenging especially at high alkyne conversions (for example, > 99%) in the hydrogenation.[5] A rapid drop in selectivity is often observed when the conversion approaches 100%. Besides the modification of Pd nanocatalysts with another alloying metal (for example, Pb in the case of Lindlar catalyst), [1-3,6,7] one efficient common strategy to improve alkene selectivity involves the modification of Pd nanocatalysts with heteroatom (such as N, S, P) containing organic ligands. Containing coordinating atoms, the ligands can reversibly bind to the surface of Pd nanoparticles through coordination. With the coordination ability often intermediate between those of alkyne and alkene (lower than that of alkyne but higher than that of alkene), their surface binding effectively

inhibits/blocks alkene adsorption so as to minimize over-hydrogenation and enhance alkene selectivity.[1,2,8]

To date, many small-molecule ligands have been reported to effectively improve the selectivity in alkyne semihydrogenation. Quinoline is the notable example in the Lindlar catalyst.[9] Pyridine derivatives[6,7] and bipyridine derivatives[16] have also been reported to tune the performance of selective hydrogenation with several different heterogeneous Pd catalyst systems. Sulfur containing compounds have been considered as strong poisons for most of the heterogeneous Pd catalysts for hydrogenation.[9] A small quantity of sulfur compounds in the reaction mixture may significantly change the performance of catalysts or even block most of the active sites. The sulfur-containing ligands can drastically influence the electronic properties of the Pd nanoparticles and thus change the hydrogenation behavior.[11] Mori et al.[12] reported that hydrogenation reactions were completely stopped at 0.01 equivalent (to the substrate) of Ph_2S_2 or PhSH even at extremely high Pd feed concentration. Takahashi et al.[13] reported that the use of dimethyl sulfoxide (DMSO) as a ligand for Pd/SiO_2 catalyst system greatly improved the selectivity of hydrogenation for several internal and terminal alkynes. Shen et al.[14] used 3,6-dithia-1,8-octanediol as the ligand for improving the selectivity in the semi-hydrogenation of 2-methyl-3-butyn-2-ol with PdZn/CN@ZnO catalyst, with a selectivity of 96% achieved at 99% of conversion. They also claimed that the sulfur-containing ligand exhibited strong poisonous property and beneficial effect for Pd catalysts at low concentration. McKenn et al.[15] reported the improved acetylene semi-hydrogenation with the use of triphenylphosphine-modified $Pd@TiO_2$ composite catalyst. However, reports of triphenylphosphine assisted selective alkyne hydrogenation with heterogeneous Pd catalysts in liquid phase are rare.[16]

Though individually proven to be highly effective in improving catalyst selectivity, the performance of the various ligands has not yet been compared. An optimum ligand is expected not only to improve selectivity but also to maintain high catalyst activity while at minimum loading. This present study is attempted to compare the performance of different ligands in liquid-phase selective hydrogenation of alkynes, with the aim of finding the optimum ones for practical applications. For the purpose, a range of most representative ligands that have been well demonstrated in the literature have been chosen, including quinoline, pyridine, DMSO, 3,6-dithia-1,8-octanediol (DTO), and triphenylphosphine. Pd nanocatalysts including both commercial heterogeneous Pd catalysts and a colloidal Pd nanocatalyst have been included for this investigation. Such a study also provides important guidelines towards efficient design of best-performing ligands for selective alkyne hydrogenation.

5.2 Experimental Section

5.2.1 Materials

Commercial Pd on activated carbon (10 wt% of Pd) and Lindlar catalyst (5 wt% of Pd on calcium carbonate, poisoned with lead) were purchased from Aldrich. Hyperbranched polyethylene ionomer supported Pd nanocatalyst (I1, 0.94 wt% of Pd) was synthesized according to a literature procedure.[17] Ultrahigh-purity H_2 (> 99.999%) was obtained from Praxair and used as received. Toluene (anhydrous, 99%), hexane (anhydrous, 99%), phenylacetylene (98%), diphenylacetylene (98%), pyridine (ReagentPlus®, ≥ 99%), quinoline (reagent grade, 98%), 3,6-dithia-1,8-octanediol (97%), dimethyl sulfoxide (DMSO) (≥ 99%), triphenylphosphine (ReagentPlus®, 99%) were obtained from Aldrich and were used as received.

5.2.2 General Procedure of Alkyne Hydrogenation

Liquid-phase hydrogenation reactions were carried out in a sealed 25 mL glass tube or a 50 mL round bottom flask connected to a hydrogen balloon. For the hydrogenation reactions catalyzed with the hyperbranched polyethylene ionomer supported catalyst, a glass tube containing a stirrer was subjected to three cycles of evacuation and purge with hydrogen gas; then a hydrogen balloon was attached to the glass tube. Afterward, a mixture of alkyne (0.5 mmol), ligand solution, Pd catalyst solution in hexane (0.2 μmol Pd), and hexane (total 5 mL) was injected into the tube to start hydrogenation reaction. For the hydrogenation reactions catalyzed by the commercial catalysts (Pd@C or Lindlar catalyst), a desired amount of catalyst was transferred into a 50 mL glass flask in a glove-box. After transferred out of the glove box, the flask was subjected to 3 cycles of evacuation and hydrogen purge, and then attached with a hydrogen balloon. Then, a mixture of alkyne (10 mmol) and the prescribed ligand in hexane (total 20 mL) was injected into the flask to start the hydrogenation. To monitor the reaction kinetics, a reaction mixture was withdrawn at prescribed times. The sampled solution was diluted with methanol and filtered with a PTFE syringe filter (0.22 μm) prior to gas chromatography (GC) analysis.

GC analysis was carried out on a HP GC-5890II instrument equipped with a supelcowax®10 capillary column (30 m × 0.2 mm × 0.2 μm), and a flame ionization detector (FID). Toluene was used as the internal standard for the calculation of alkyne conversion. Alkene selectivity was calculated from the GC results as the percentage of alkenes produced among all the products formed; cis:trans isomeric ratios were presented in molar ratios.

5.3 Results and Discussion

Three different Pd nanocatalysts, including two commercial Pd nanocatalysts (Pd@C and Pb-doped Lindlar catalysts) and a colloidal hyperbranched polyethylene ionomer-stabilized Pd nanocatalyst (termed as I1 catalyst with a Pd loading of 0.94 wt%), are employed herein to have a systematic study on the ligand effects. While the two commercial catalysts are synthesized by immobilizing Pd nanoparticles on heterogeneous micrometer-sized solid supports, the hyperbranched polyethylene ionomer supported Pd nanocatalyst was synthesized uniquely by an in situ polymerization method. Therein, ethylene copolymerization with an acrylate-type ionic liquid comonomer containing a quaternary tetraalkylammonium cation and a tetrafluoroborate counter anion is undertaken with a cationic chain-walking Pd–diimine catalyst. The polymerization renders the hyperbranched polyethylene ionomer containing a hyperbranched polyethylene backbone functionalized with quaternary ammonium ions. Meanwhile, in situ reduction of the Pd(II)-based polymerization catalyst results in Pd(0) nanoparticles during the polymerization, which are captured and stabilized by the ionomer through their quaternary ammonium ions as the macromolecular surface stabilizer/surfactant.[18] Due to the hyperbranched polyethylene skeleton, the ionomer-stabilized Pd nanocatalyst can be well dispersed in nonpolar or low-polarity organic solvents where the hyperbranched polyethylene can dissolve (such as hexane, toluene, tetrahydrofuran, etc.). In these solvents, the catalyst can thus resemble surfactant-bound colloidal nanocatalysts with the distinct advantage of high catalytic activity due to the homogeneous ionomer support.

Two most representative alkyne substrates, including phenylacetylene (PA) as a terminal alkyne and diphenylacetylene (DPA) as an internal alkyne, have been used herein to demonstrate the ligand effects on their hydrogenation under mild conditions (25 °C; 1 atm H_2 pressure). The

range of ligands studied herein include two N-containing ligands (quinoline and pyridine), two S-containing ligands (DMSO and DTO), and one P-containing ligand (triphenylphosphine).

5.3.1 Effects of Quinoline

Quinoline is the classical ligand for Pd nanocatalysts in selective hydrogenation of alkynes. Its effect was first investigated. In particular, the hydrogenation of PA (0.1 M) was undertaken with I1 catalyst at a Pd loading of 0.04 mol% and at varying quinoline/Pd molar ratios in the range 211–1687. This reaction condition is so selected as to achieve a high reaction rate accompanied with a suspected high over-hydrogenation to form ethylbenzene as the alkane side product, which allows a sensitive assessment of the effects of quinoline. The reaction should give styrene as the selective hydrogenation product and ethylbenzene as the side product by over-hydrogenation. Figure 5.1 shows kinetic curves (conversion and yield curves) of the reactions undertaken at different quinoline/Pd ratios. In the control run undertaken in the absence of quinoline, PA conversion increases from 35% at 0.5 h to nearly full conversion (99%) at 1.5 h with the alkene (styrene) selectivity well retained at around 98% during the period. The high selectivity within the period is attributed to the significant presence of alkyne in the reaction system, which has a much higher coordinating capability to the catalytic active centers than alkene and can thus inhibit over-hydrogenation to form alkane. Afterwards, a drastic drop in selectivity to 40% is observed upon extension of the reaction time to 3.5 h, due to the nearly complete consumption of alkyne (> 99% conversion) and the loss of inhibition of over-hydrogenation. The slope of the selectivity curve in the latter period is thus a sensitive indicator of the rate of over-hydrogenation, with the higher slope representing a faster drop in selectivity

and the faster occurrence of over-hydrogenation. The ligand effect on selectivity should thus be reflected mainly in the latter period following the nearly complete PA conversion.

Relative to the control run, the addition of quinoline at increasing amounts shows continuous improvements in the catalyst selectivity, along with minor enhancements in catalyst activity. As shown in Figure 5.1(a), relative to the value of 66% in the control run at the same time, the conversion of PA at 1 h is enhanced in various degrees to 95, 93, > 99.9, and 80% at the quinoline/Pd ratio of 211, 422, 844, and 1687, respectively, with the nearly complete conversion (> 99.9%) of PA reached by 1.5 h in all runs. This indicates that the addition of quinoline modifies structures of the active sites. Following the nearly complete PA conversion, the styrene selectivity curves displayed in Figure 5.1(b) show gradually slowed drop (*i.e.*, continuously reduced slopes) with the increase of the quinoline/Pd ratio. Relative to the value of 49% at 3 h in the control run, the selectivity values at the same time are 72 and 78% in the runs with quinoline/Pd ratios of 211 and 422, respectively. In the other two runs at the higher quinoline/Pd ratios, the selectivity at 3.5 h as a longer time is even better maintained at 80 and 89%, respectively. In particular, in the run at the highest quinoline/Pd ratio of 1687, the least selectivity drop (from nearly 100% at 1 h to 89% at 3.5 h) is observed. These kinetic results demonstrate the positive effect of quinoline on improving the alkene selectivity while slightly enhancing the high activity of the ionomer-supported Pd nanocatalyst.

Figure 5.2 shows the effect of quinoline on PA hydrogenation with the Lindlar catalyst at two different quinoline/Pd ratios (200 and 1000). Similarly, the addition of quinoline improves the catalytic activity with > 99.9% of PA conversion achieved earlier by 2 h and 1.6 h, respectively, relative to the control run without quinoline (by 3 h; see Figure 5.2(a)). For the styrene selectivity, a significantly reduced drop following the nearly complete PA conversion is

only observed in the run at the high quinoline/Pd ratio of 1200. No pronounced effect is observed in the other run at the quinoline/Pd ratio of 200, with its slope of the selectivity curve similar to that of the control run.

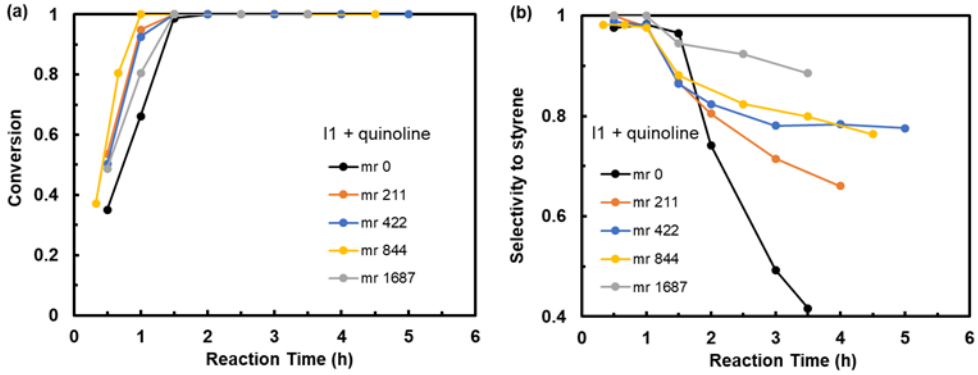

Figure 5.1 Effect of quinoline at different quinoline/Pd molar ratios on the hydrogenation of PA with the I1 catalyst: (a) PA conversion and (b) styrene selectivity. Other conditions: [PA] = 0.1 M, Pd loading = 0.04 mol%, room temperature.

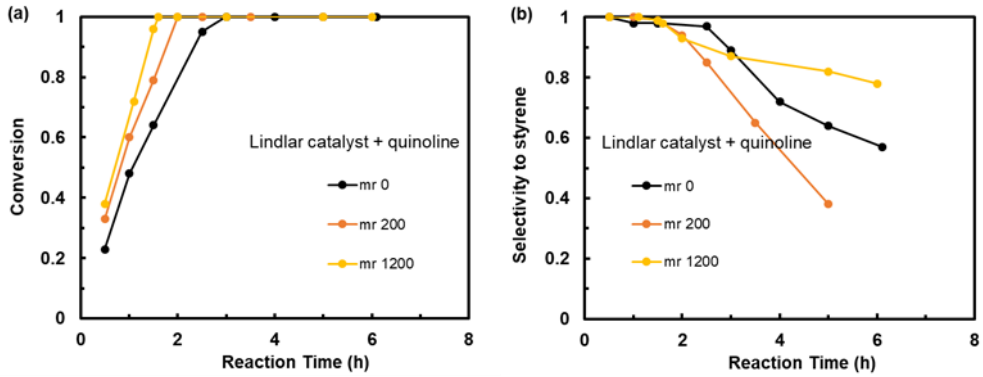

Figure 5.2 Effect of quinoline at different quinoline/Pd molar ratios on the hydrogenation of PA with Lindlar catalyst: (a) PA conversion and (b) styrene selectivity. Other conditions: [PA] = 0.5 M, Pd loading = 0.04 mol%, room temperature.

Figure 5.3 shows the kinetic curves of the PA hydrogenation reactions undertaken with the Pd@C catalyst at different quinoline/Pd ratios (100, 200, and 1200). With this catalyst, the addition of quinoline has no marked effect on catalyst activity, with similar conversion curves observed and the achievement of nearly complete conversion (99.9%) of PA by ca. 3.5 h in all runs. Meanwhile, the increase of quinoline/Pd ratio also has only marginal effects on the selectivity, with only slight reductions in the slope of the selectivity curve following nearly complete PA conversion. However, one distinct difference is that all runs with quinoline show > 99% of styrene selectivity before the nearly complete conversion of PA (99.9%) while the selectivity in the control run without quinoline is only about 92–90% even before the complete PA conversion, along with a slight drop. This indicates that the active centers in this Pd@C catalyst differ from those in I1 and Lindlar catalysts, possibly resulting from the substrate effects.

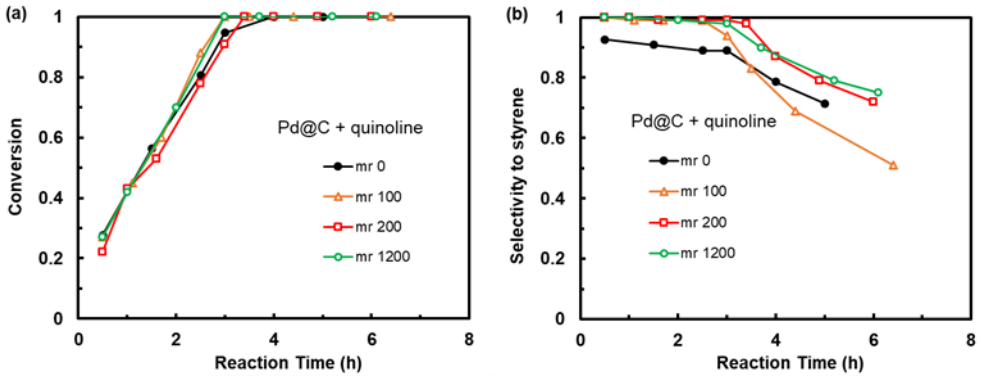

Figure 5.3 Effect of quinoline at different quinoline/Pd molar ratios on the hydrogenation of PA with Pd@C catalyst: (a) PA conversion and (b) styrene selectivity. Other conditions: [PA] = 0.5 M, Pd loading = 0.04 mol%, room temperature.

The effects of quinoline on the selective hydrogenation of DPA with the three catalysts were subsequently investigated. In the hydrogenation of DPA as an internal alkyne, two alkene

products, cis- and trans-stilbenes, are possible, with cis-stilbene as the predominant favored product and the trans-stilbene as an isomer by-product, besides the bibenzyl by-product resulting from over-hydrogenation. Figure 5.4 shows the kinetic curves of the reactions with I1 at different quinoline/Pd ratios (63, 190, 338, 633, and 1898). Increasing the quinoline/Pd ratio leads to consistently reduced activities, with the time for reaching nearly complete DPA conversion (> 99.9%) gradually postponed. In the control run without quinoline, DPA reaches the conversion of > 99.9% by 0.83 h, while it occurs at 1.5 h, 2 h, and 5 h in the runs at the quinoline/Pd ratios of 63, 190, and 338, respectively. At the even higher ratios of 633 and 1898, only incomplete conversions of 80% and 38.2%, respectively, are reached within 6 h, indicating the drastic reductions in the catalyst activity due to excessive quinoline. Simultaneously, with the increase of quinoline dosage, the alkene selectivity curve is much more stable with continuously reduced slopes compared to the control run. In the control run, a drastic decrease in alkene selectivity is observed after DPA conversion reaches 99.9%, from 95.4% at 1 h to 14.4% at 5 h. On the contrary, in the runs at the quinoline/Pd ratios of 63, 190, and 338, the alkene selectivity is well maintained at 81.4% (4 h), 88.6% (4 h), and 91.6% (5 h), respectively. In the other two runs at the ratios of 633 and 1898, alkene selectivity is maintained nearly constant at 95% and 98%, respectively, throughout the whole reaction period since complete DPA conversion has not been reached. In all the runs, the percentage of E-stilbene in the alkene products is maintained constant at 2–3%, with negligible dependences on quinoline/Pd ratio or reaction time. The same finding is seen when other ligands (pyridine, DMSO, 3,6-dithia-1,8-octanediol, triphenylphosphine) are used as shown below. This indicates that both alkene isomers have similar reactivity toward over-hydrogenation by the I1 catalyst.

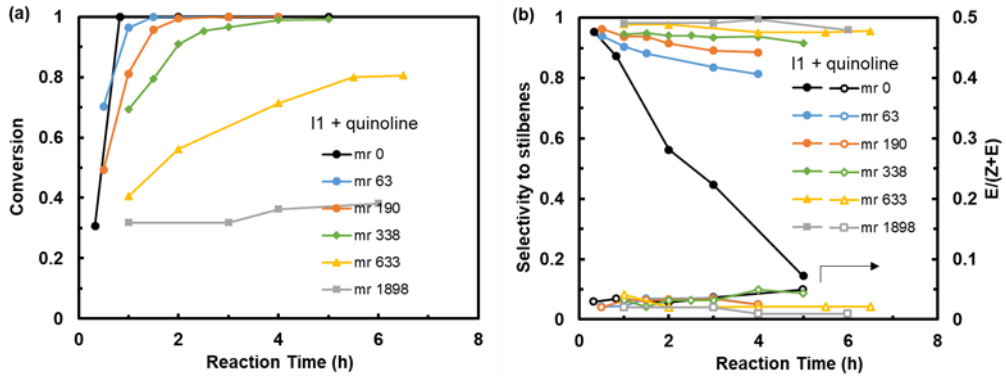

Figure 5.4 Effect of quinoline at different quinoline/Pd molar ratios on the hydrogenation of DPA with the I1 catalyst: (a) DPA conversion and (b) stilbene selectivity and E-stilbene percentage. Other conditions: [DPA] = 0.1 M, Pd loading = 0.04 mol%, room temperature.

Figure 5.5 shows the kinetic curves of DPA hydrogenation with the Lindlar catalyst at two quinoline/Pd ratios (190 and 630). Like the above ones with I1, a similar trend of effects by quinoline is also observed with significantly reduced catalytic activity and better-maintained selectivity. In the case at the quinoline/Pd ratio of 630, nearly complete DPA conversion (> 99.9%) does not reach until at about 8 h (vs. 1.5 h in control run) and the stilbene selectivity is maintained at 98% with negligible changes even 5 h after the nearly complete conversion of DPA. On the contrary, the ratio of 190 is insufficient for selectivity control though improved compared to the control run, with a selectivity drop from 95% at about 1.5 h to 82% at 5 h. With this Lindlar catalyst, the percentage of E-stilbene in the alkenes is also constant at ca. 4%, regardless of reaction time, ligand and its amount.

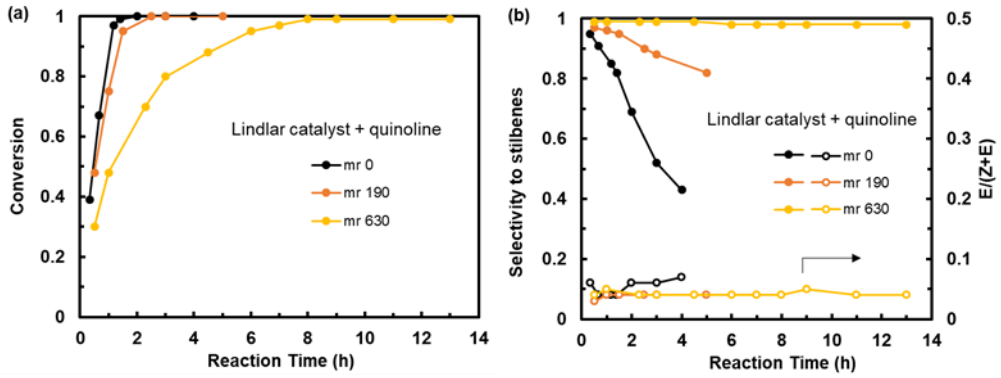

Figure 5.5 Effect of quinoline at different quinoline/Pd molar ratios on the hydrogenation of DPA with Lindlar catalyst: (a) DPA conversion and (b) stilbene selectivity and E-stilbene percentage. Other conditions: [DPA] = 0.5 M, Pd loading = 0.04 mol%, room temperature.

Figure 5.6 compares the kinetic curves in the hydrogenation of DPA with Pd@C without/with quinoline (quinoline/Pd ratio of 620). In the control run without quinoline, the stilbene selectivity is 93% at the DPA conversion of 75% (at 1 h). With the further increase of DPA conversion, the stilbene selectivity decreases to 87% (conversion: 96%) and 66% (conversion: 100%) at 1.5 h and 2 h, respectively. Afterwards, it drops rapidly to 31% and 12% at 3.5 h and 4.5 h, respectively. While the E-stilbene content in the stilbenes is nearly constant at ca. 3% by 1.5 h, it increases rapidly following the nearly complete DPA conversion (> 99.9%) to 27% at 4.5 h. Along with the simultaneous drop in stilbene selectivity, this suggests that Z-stilbene undergoes over-hydrogenation while E-stilbene can not be over-hydrogenated with the Pd@C catalyst. Consistent with the finding from the hydrogenation of PA above, the results also suggest that Pd@C possesses catalytically different active centers from the I1 and Lindlar catalysts since both E- and Z-stilbenes can be over-hydrogenated with the latter.

Compared to the control run, the addition of quinoline drastically improves the catalyst performance in rendering high/stable stilbene selectivity and minimizing the E-stilbene content but at some sacrifice of catalyst activity. The time to reach nearly complete DPA conversion (> 99.9%) is delayed to about 6 h. However, the stilbene selectivity is well maintained within 93–88% even at the extension of the reaction for additional 6 h (total 12 h). In the mean time, E-stilbene content (4–7%) in the stilbenes shows only marginal increases over the entire 12 h of reaction.

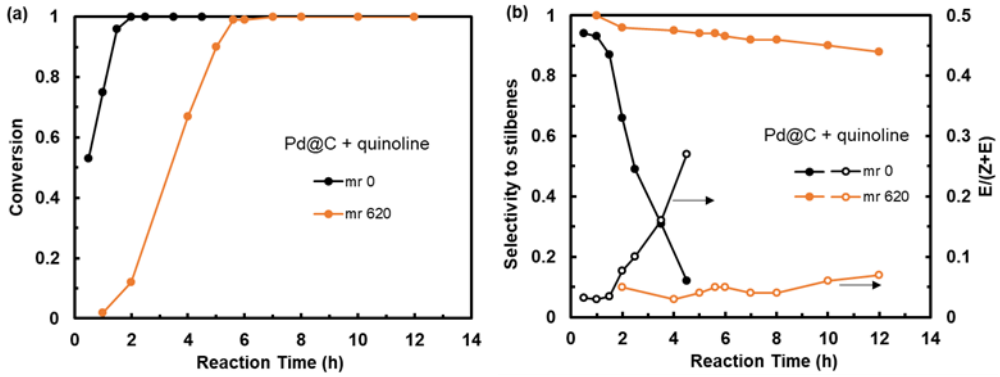

Figure 5.6 Effect of quinoline (quinoline/Pd molar ratio: 620) on the hydrogenation of DPA with the Pd@C catalyst: (a) DPA conversion and (b) stilbene selectivity and E-stilbene percentage. Other conditions: [DPA] = 0.5 M, Pd loading = 0.04 mol%, room temperature.

Based on the above results on the hydrogenation of both PA and DPA with the three catalysts, it can be concluded that the use of quinoline can improve the selectivity toward the desired alkene product by reducing over-hydrogenation. However, high quinoline/Pd ratios (such as ca. 1687 for PA and ca. 620 for DPA) are required to achieve satisfactory selectivity improvements. This can be problematic due to the need for the separation of the significant amount of quinoline from the products following reactions, which can be effort- and energy-consuming. While negligible changes or even slight improvements in catalyst activity are noted in the hydrogenation of PA as a terminal alkyne in the presence of quinoline, significant activity

decreases are found in the hydrogenation of DPA possibly due to its lowered reactivity as an internal alkyne.

5.3.2 Effects of Pyridine

Pyridine is a common ligand employed in many reactions. Given its structural similarity to quinoline, its effects on the hydrogenation of both PA and DPA have been investigated. Figure 5.7 shows the kinetic curves in the hydrogenation of PA with I1 catalyst in the presence of pyridine at different pyridine/Pd ratios. When the ratio is ≤ 1860, the addition of pyridine slightly improves the catalytic activity. But when the ratio is 3100, a slight reduction in the activity is noted. Increasing the ratio from 310 to 3100 leads to continuously improved styrene selectivity, with the slope of the selectivity curve gradually reduced. Relative to quinoline (see Figure 5.1), pyridine is less effective in improving the selectivity, with a double molar amount needed in order to achieve the similar effect on the selectivity curve.

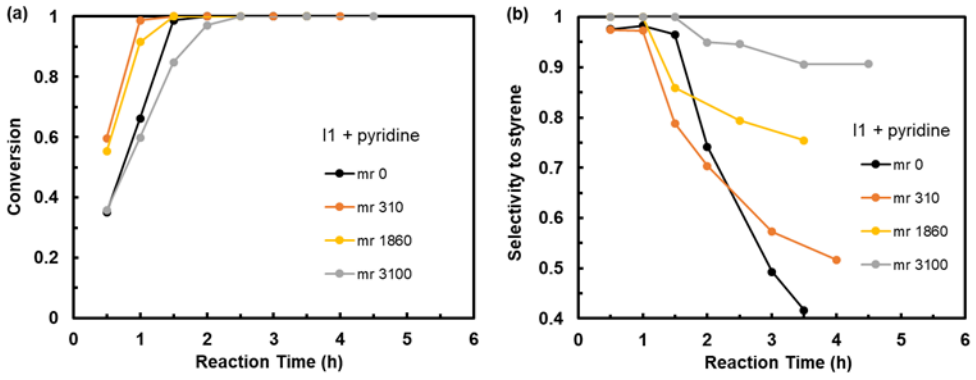

Figure 5.7 Effect of pyridine at different pyridine/Pd molar ratios on the hydrogenation of PA with the I1 catalyst: (a) PA conversion and (b) styrene selectivity. Other conditions: [PA] = 0.1 M, Pd loading = 0.04 mol%, room temperature.

Figure 5.8 shows the kinetic curves in the hydrogenation of PA with the Lindlar catalyst in the presence of pyridine at two ratios (600 and 2970, respectively). Pyridine does not seem to have a positive effect on the selectivity with the Lindlar catalyst. At the pyridine/Pd ratio of 600, one can see a slightly enhanced catalyst activity but with the deteriorated selectivity performance compared to the control run. Even at the ratio of 2970, no significant improvement is observed with the selectivity curve showing a similar slope as that of the control run, though a significant reduction in activity is noted.

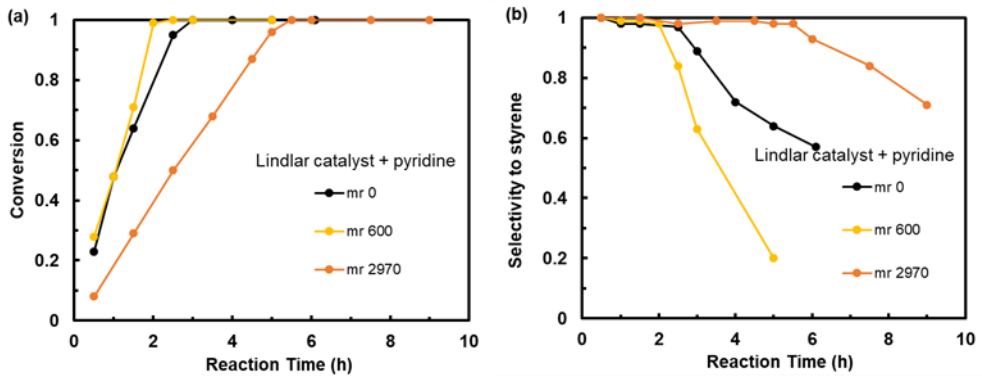

Figure 5.8 Effect of pyridine at different pyridine/Pd molar ratios on the hydrogenation of PA with the Lindlar catalyst: (a) PA conversion and (b) styrene selectivity. Other conditions: [PA] = 0.5 M, Pd loading = 0.04 mol%, room temperature.

Unlike I1 and the Lindlar catalyst, the activity of the Pd@C catalyst is somehow very sensitive to pyridine. At the high pyridine/Pd ratio of 400, the conversion reached after 4 h is only 12%. Nearly complete PA conversion (> 99.9%) can only be reached at low ratios. Figure 5.9 shows the kinetic curves at the ratios of 0.5 and 50. A significant reduction in catalyst activity is seen at the ratio of 50, while with no pronounced effect at the ratio of 0.5. In both runs,

the presence of pyridine deteriorates the selectivity with even more severe drop in selectivity following the nearly complete conversion (> 99.9%) of PA.

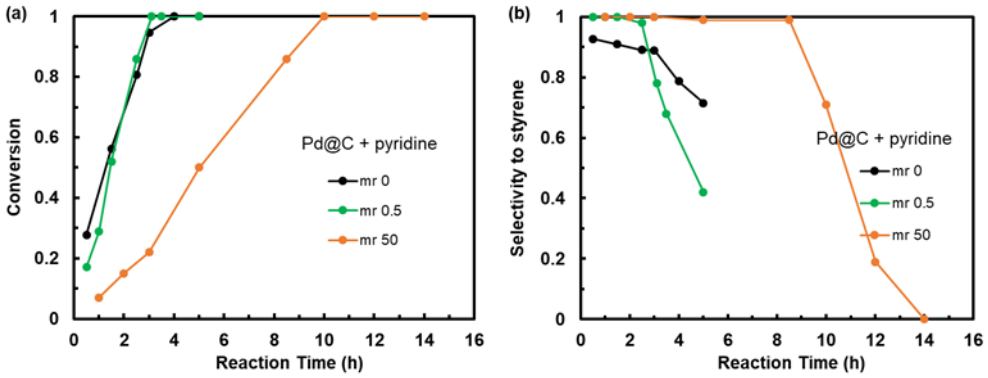

Figure 5.9 Effect of pyridine at different pyridine/Pd molar ratios on the hydrogenation of PA with the Pd@C catalyst: (a) PA conversion and (b) styrene selectivity. Other conditions: [PA] = 0.5 M, Pd loading = 0.04 mol%, room temperature.

Figure 5.10 shows the effect of pyridine on the hydrogenation of DPA with I1 catalyst. No significant effect on activity is seen except at the highest ratio of 1858. Improved stilbene selectivity curves are observed with gradually reduced slopes with the increase of the ratio. However, relative to quinoline (at ratio of 338), the amount of pyridine (ratio of 1858) required to reach the similar effect is much more, about 5–6 times.

Figure 5.11 shows the kinetic curves in the hydrogenation of DPA with the Lindlar catalyst at the different pyridine/Pd ratios. For this internal alkyne, the activity of Lindlar catalyst shows surprisingly high sensitivity towards pyridine, which differs from the hydrogenation of PA with the same catalyst/ligand system. Compared to the runs with PA, much lowered pyridine/Pd ratios (30 and 60) are used, with higher ratios leading to low DPA conversions despite long reaction times. At the ratio of 60, the time to reach the DPA conversion of > 99.9%

is postponed significantly to 10 h relative to ca. 1.4 h in the control run. From the stilbene selectivity curves, increasing the pyridine/Pd ratio shows only minor improvements in the selectivity performance, though with continuously reduced slopes noticed. In the run at the ratio of 60, the stilbene selectivity drops already to 84% at 9 h with 97% of DPA conversion.

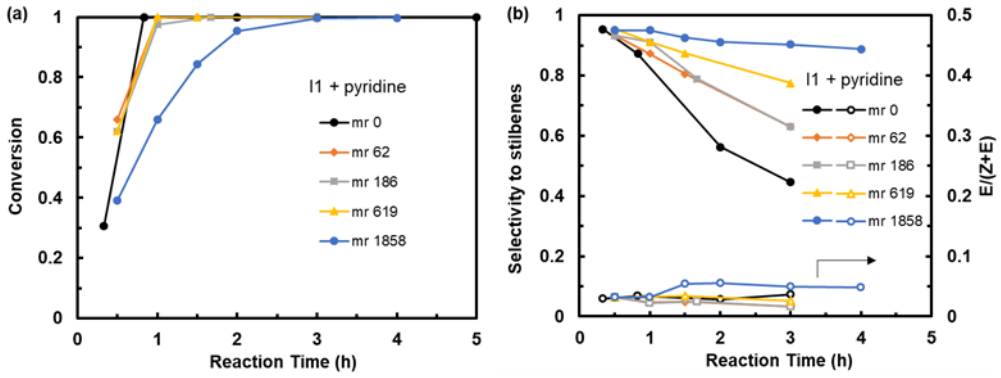

Figure 5.10 Effect of pyridine at different pyridine/Pd molar ratios on the hydrogenation of DPA with the I1 catalyst: (a) DPA conversion and (b) stilbene selectivity and E-stilbene percentage. Other conditions: [DPA] = 0. 1 M, Pd loading = 0.04 mol%, room temperature.

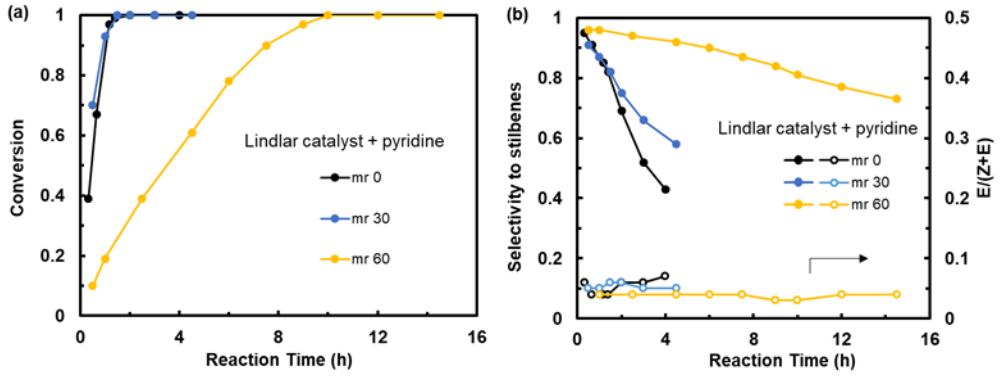

Figure 5.11 Effect of pyridine at different pyridine/Pd molar ratios on the hydrogenation of DPA with the Lindlar catalyst: (a) DPA conversion and (b) stilbene selectivity and E-stilbene percentage. Other conditions: [DPA] = 0.5 M, Pd loading = 0.04 mol%, room temperature.

Figure 5.12 displays the kinetic curves in the hydrogenation of DPA with the Pd@C catalyst at different pyridine/Pd ratios. The activity of the catalyst also shows a high sensitivity towards the pyridine/Pd ratio. Only at the low ratio of 30, a nearly complete conversion of DPA (> 99.9%) is possible within the experimental time window (5 h). However, at this ratio, the over-hydrogenation cannot be sufficiently suppressed, with fast selectivity drop over time observed after reaching the high DPA conversion (> 99.9%).

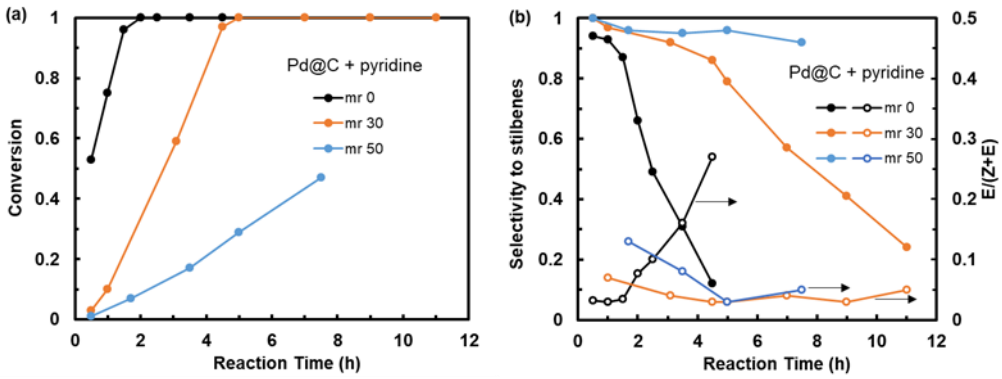

Figure 5.12 Effect of pyridine at different pyridine/Pd molar ratios on the hydrogenation of DPA with the P@C catalyst: (a) DPA conversion and (b) stilbene selectivity and E-stilbene percentage. Other conditions: [DPA] = 0.5 M, Pd loading = 0.04 mol%, room temperature.

In summary of the above runs, pyridine is not as effective as quinoline in improving alkene selectivity, though structurally similar. Meanwhile, its effects on catalyst activity depend on both the catalyst and the alkyne substrate, with the precise mechanism unknown at the moment. In reaction systems (Lindlar for DPA; Pd@C for both PA and DPA) that are very sensitive to pyridine dosage, the selectivity improvement is often very minor. In other systems (such as I1 for PA and DPA; Lindlar for PA) that can tolerate high pyridine dosages, generally much higher pyridine/Pd ratios are required to reach desired selectivity improvements.

5.3.3 Effects of DMSO

Figure 5.13 shows the effect of DMSO on the hydrogenation of PA with I1 catalyst at various DMSO/Pd ratios (14–704). At all the ratios, slight enhancements in the catalyst activity can be seen from Figure 5.13(a), with the time for reaching the PA conversion of > 99.9% shortened to around 1 h relative to 2 h in the control run. Increasing the ratio leads to significantly improved selectivity curves. In particular, at the ratios of 352 and 704, high styrene selectivity of ca. 97% is well maintained for additional 3 h after the nearly full conversion of PA with no drop at all. This is much improved relative to quinoline at similar loadings.

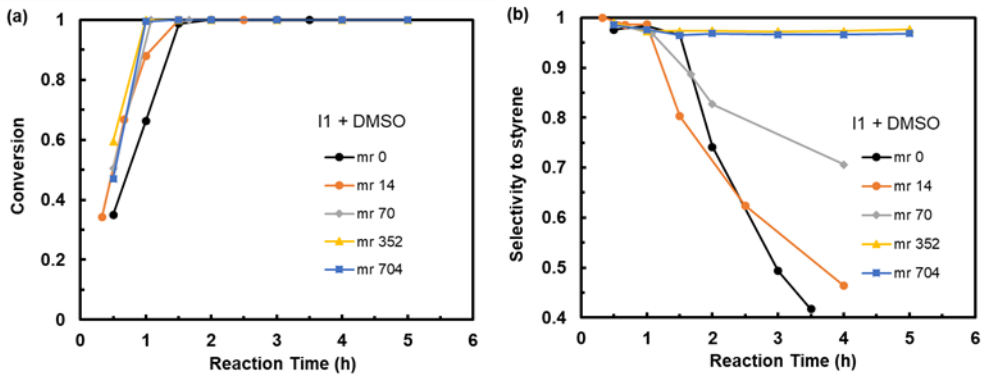

Figure 5.13 Effect of DMSO at different DMSO/Pd molar ratios on the hydrogenation of PA with the I1 catalyst: (a) PA conversion and (b) styrene selectivity. Other conditions: [PA] = 0.1 M, Pd loading = 0.04 mol%, room temperature.

While highly effective with the I1 catalyst, DMSO does not improve the selectivity performance of the Lindlar catalyst for the hydrogenation of PA. Figure 5.14 shows the kinetic curves. Relative to the control run, there are no apparent improvements in the selectivity curves (in terms of the slopes) with the DMSO/Pd ratio in the range of 10–400, though a clear reduction in the catalyst activity is noted in the run at the ratio of 400. DMSO was previously investigated

for its effect on PA hydrogenation with a Pd@SiO_2 catalyst at a DMSO/Pd molar ratio of 435. Therein, a styrene selectivity of 98% was obtained at 1 h. However, no data was reported after full conversion of PA.[13]

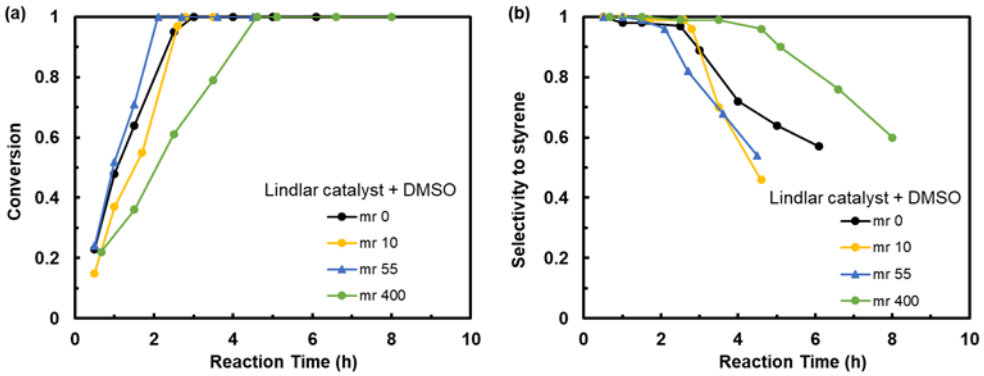

Figure 5.14 Effect of DMSO at different DMSO/Pd molar ratios on the hydrogenation of PA with the Lindlar catalyst: (a) PA conversion and (b) styrene selectivity. Other conditions: [PA] = 0.5 M, Pd loading = 0.04 mol%, room temperature.

Figure 5.15 shows the effect of DMSO on the hydrogenation of PA with the Pd@C catalyst. At the DMSO/Pd ratio of 55, a distinct improvement in the selectivity curve can be seen while with no significant change in the conversion curve. Following the nearly complete conversion (99.9%) of PA at 4 h, only minor decreases in the styrene selectivity from 97 to 91% are seen after extension of the reaction for additional 3.5 h. A further increase of the DMSO/Pd ratio to 400 leads only to marginal improvements in the selectivity curve relative to the one at the ratio of 55, while an obvious reduction in catalyst activity is seen with the time for reaching the PA conversion of > 99.9% extended to 5.8 h.

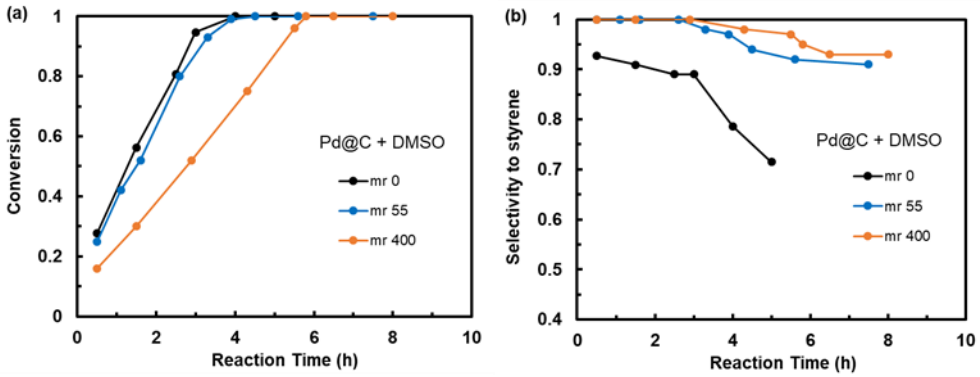

Figure 5.15 Effect of DMSO at different DMSO/Pd molar ratios on the hydrogenation of PA with the Pd@C catalyst: (a) PA conversion and (b) styrene selectivity. Other conditions: [PA] = 0.5 M, Pd loading = 0.04 mol%, room temperature.

Figure 5.16 shows the effect of DMSO on the hydrogenation of DPA with I1 catalysts. At the DMSO/Pd ratios of 7 and 28, slight reductions in the catalytic activity are observed relative to the control run, along with much reduced selectivity drop following the complete conversion of DPA. However, at the further enhanced ratio of 70, the best DPA conversion can be achieved is 97.5% despite the extension of the reaction time to 7 h, indicating the excessive DMSO.

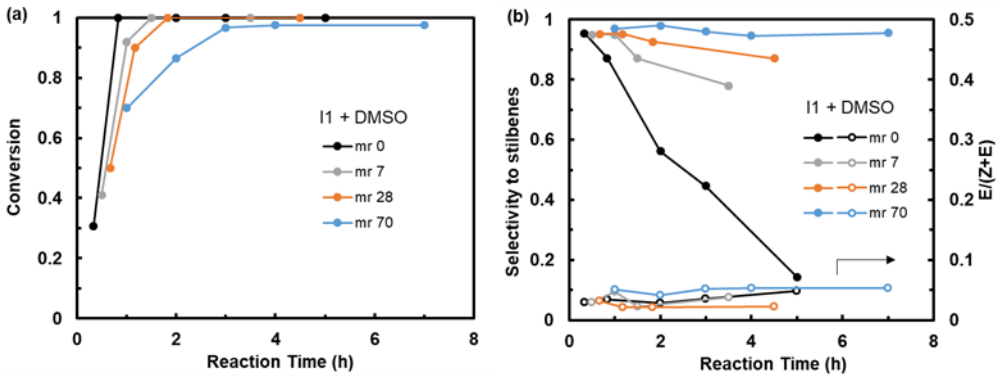

Figure 5.16 Effect of DMSO at different DMSO/Pd molar ratios on the hydrogenation of DPA with the I1 catalyst: (a) DPA conversion and (b) stilbene selectivity and E-stilbene percentage. Other conditions: [PA] = 0.1 M, Pd loading = 0.04 mol%, room temperature.

Though inefficient in improving the selectivity performance of the Lindlar catalyst toward the hydrogenation of PA, DMSO is found highly efficient in improving the stilbene selectivity in the hydrogenation of DPA with the same catalyst. Figure 5.17 shows the kinetic curves. At the DMSO/Pd ratio of 14, the progress of the reaction is slowed down significantly with the time for reaching DPA conversion of 99% postponed to 7 h (1.4 h in the control run), with no further increase after another 4 h of reaction. In consequence, the stilbene selectivity is better maintained with much reduced rate of drop relative to the control run. At the doubled DMSO/Pd ratio of 28, DPA conversion stays at 66% after 2.6 h with no further increase afterwards, suggesting its over-dosage.

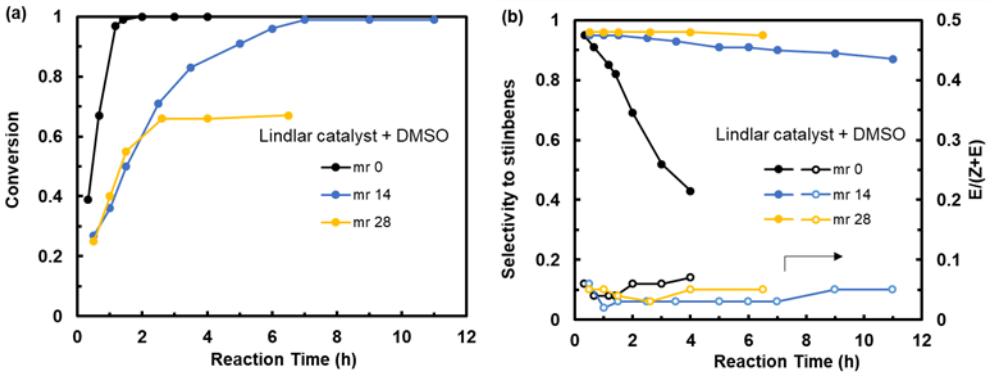

Figure 5.17 Effect of DMSO at different DMSO/Pd molar ratios on the hydrogenation of DPA with the Lindlar catalyst: (a) DPA conversion and (b) stilbene selectivity and E-stilbene percentage. Other conditions: [PA] = 0.5 M, Pd loading = 0.04 mol%, room temperature.

Figure 5.18 shows the effect of DMSO on the hydrogenation of DPA with the Pd@C catalyst at the DMSO/Pd ratio of 4.7. Despite the low ratio, a pronounced reduction in the catalytic activity is seen, with a DPA conversion of 99% reached at 7 h. The over hydrogenation is reduced to some extent relative to the control. But a significant drop of the stilbene selectivity

from 89 to 68% is found with the increase of time from 7 to 12 h. In the mean time, the E-stilbene content shows a concomitant increase, indicating the over hydrogenation of Z-stilbene only by the catalytic centers as seen in the control run.

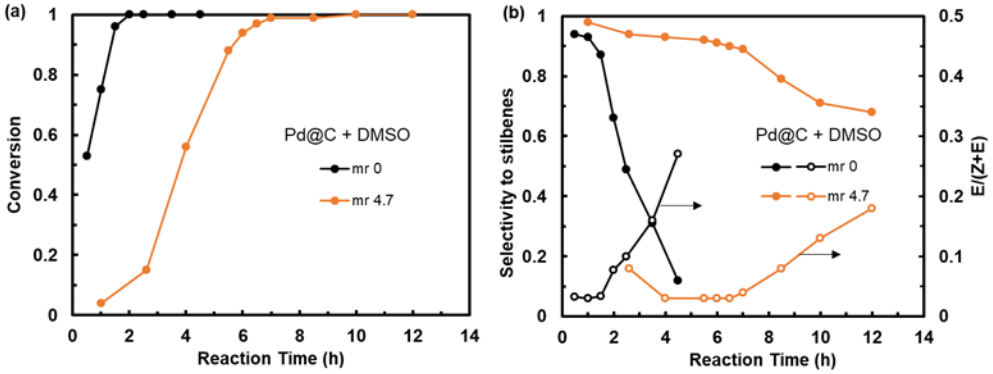

Figure 5.18 Effect of DMSO (DMSO/Pd molar ratio: 4.7) on the hydrogenation of DPA with the Pd@C catalyst: (a) DPA conversion and (b) stilbene selectivity and E-stilbene percentage. Other conditions: [PA] = 0.5 M, Pd loading = 0.04 mol%, room temperature.

From the above runs, DMSO shows effects in improving the alkene selectivity, except in the hydrogenation of PA with the Lindlar catalyst. Compared to quinoline, it requires lower dosages with a better performance in suppressing the over hydrogenation of alkenes.

5.3.4 Effects of DTO

DTO, a sulfide containing ligand, has been reported as an efficient poisoner for the Lindlar catalyst.[19] Herein, its effects on the hydrogenation of both PA and DPA have been investigated. Figure 5.19 compares the kinetic curves in the hydrogenation of PA with I1 catalyst at different DTO/Pd molar ratios (0.09–0.91). The presence of DTO at a trace amount with the

molar ratio of 0.09 is shown to drastically improve the styrene selectivity while without minimum effect on the conversion curve. In the run, the time to reach PA conversion of > 99.9% is 2.5 h relative to 2 h in the control run. Meanwhile, the styrene selectivity is 96% at 2.5 h and it remains stable at 95% at 4.7 h. Increasing the ratio to 0.33 significantly reduces the catalyst activity with the time for >99.9% of PA conversion postponed to 10.5 h, along with a further but minor improvement in the styrene selectivity, 98% at 10.5 h with no drop from 10.5 to 13.5 h. At the further increased ratio of 0.91, the progress of the reaction is further delayed with the highest PA conversion of 98% achieved after 18 h, though the styrene selectivity remains stable at 98%. These runs demonstrate the high efficiency of DTO in improving the selectivity of the I1 catalyst, with a low ratio of around 0.09 sufficient to achieve drastic effects.

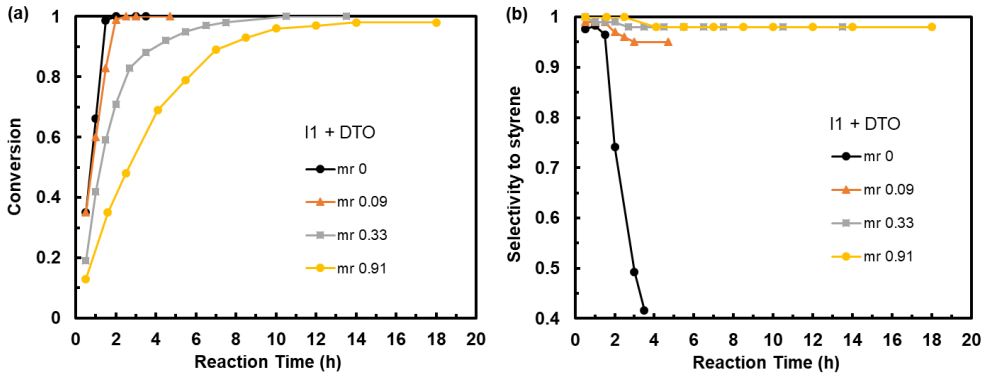

Figure 5.19 Effect of DTO at different molar ratios on the hydrogenation of PA with the I1 catalyst: (a) PA conversion and (b) styrene selectivity. Other conditions: [PA] = 0.1 M, Pd loading = 0.04 mol%, room temperature.

DTO is also highly efficient in improving the selectivity performance of both the Lindlar and Pd@C catalysts for the hydrogenation of PA. Figure 5.20 shows the effects of DTO on the hydrogenation PA with the Lindlar catalyst at two DTO/Pd ratios (0.5 and 2). At both ratios,

similar kinetic curves are obtained, with slightly reduced activity (PA conversion of 99% at 5.5 h) but significantly more stable styrene selectivity (0.98 from 5.5 to 10.2 h).

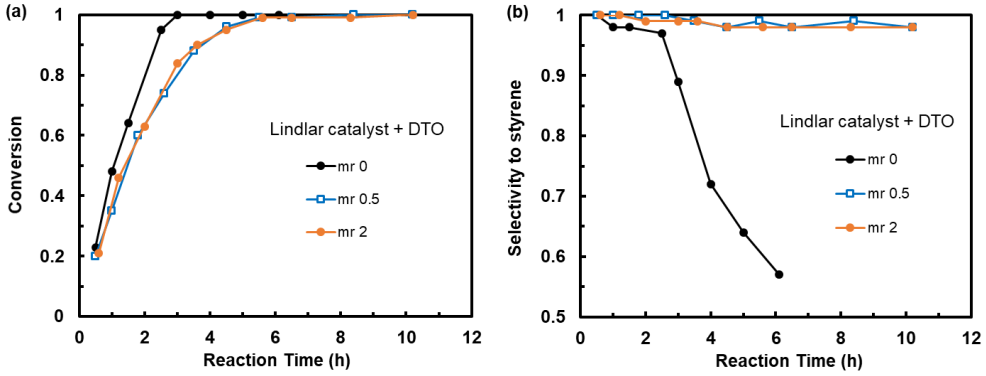

Figure 5.20 Effect of DTO at different molar ratios on the hydrogenation of PA with the Lindlar catalyst: (a) PA conversion and (b) styrene selectivity. Other conditions: [PA] = 0.5 M, Pd loading = 0.04 mol%, room temperature.

Figure 5.21 compares the kinetic curves in the hydrogenation of PA with the Pd@C catalyst in the presence of DTO at three ratios (0.5, 2, and 15). Relative to the control run, a similar PA conversion curve but with a much more stable styrene selectivity curve is achieved at the DTO/Pd ratio of 0.5. The styrene selectivity remains strikingly constant at 98% after the nearly complete PA conversion (99%) at 3 h. At the two higher DTO/Pd ratios (2 and 15), the reaction is significantly delayed with the PA conversion stilled at ca. 95% despite its extension to as high as 14 h, indicating the excessive amounts of DTO.

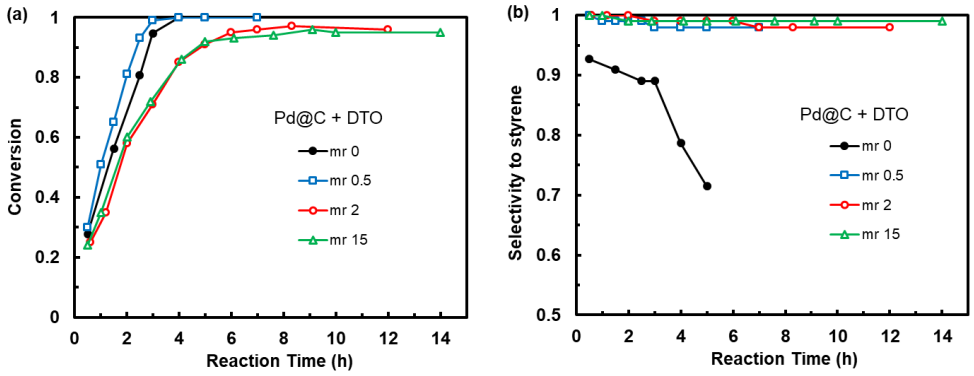

Figure 5.21 Effect of DTO at different molar ratios on the hydrogenation of PA with the Pd@C catalyst: (a) PA conversion and (b) styrene selectivity. Other conditions: [PA] = 0.5 M, Pd loading = 0.04 mol%, room temperature.

Though highly efficient in improving the performance of all three catalysts in the selective hydrogenation of PA, the effects of DTO on the hydrogenation of DPA are relatively restricted. Figure 5.22 compares the kinetic curves in the hydrogenation of DPA with I1 catalyst. Compared to the hydrogenation of PA, lower DTO/Pd ratios are used, which is also the case in subsequent runs with other two catalysts. As a clear trend, the use of DTO slows down the progress of the reaction and decreases the rate of selectivity drop after reaching the complete conversion (> 99.9%) of DPA. Nevertheless, at the ratio of 0.02, the stilbene selectivity still drops significantly from 86% at 2.6 h to 68% at 6 h, indicating the insufficient suppression of the over-hydrogenation at the ratio. The same trend is found in the runs undertaken with the Lindlar catalyst (see Figure 5.23). Increasing the DTO/Pd ratio from 0.01 to 0.06 continuously reduces the catalyst activity, along with a trend of minor improvements in the selectivity curves. Figure 5.24 shows the kinetic curves of the run with the Pd@C catalyst at the DTO/Pd ratio of 0.04.

Similarly, a drop in catalyst activity is observed relative to the control run, but only with a limited improvement in the stilbene selectivity curve.

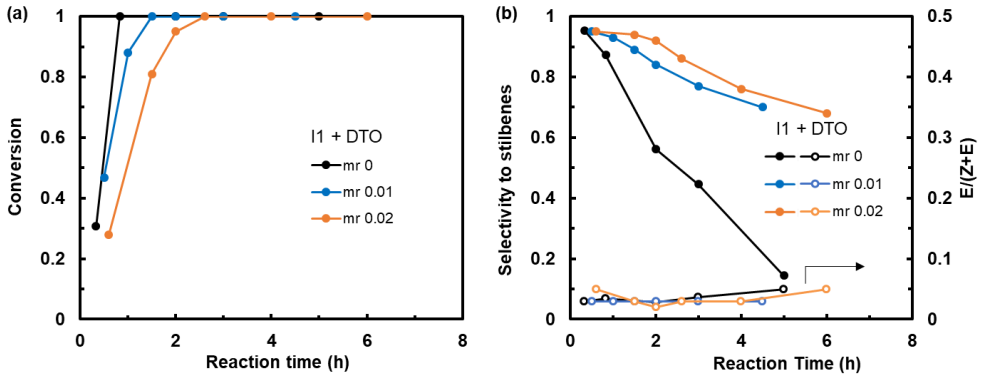

Figure 5.22 Effect of DTO at different molar ratios on the hydrogenation of DPA with the I1 catalyst: (a) DPA conversion and (b) stilbene selectivity and E-stilbene percentage. Other conditions: [PA] = 0.1 M, Pd loading = 0.04 mol%, room temperature.

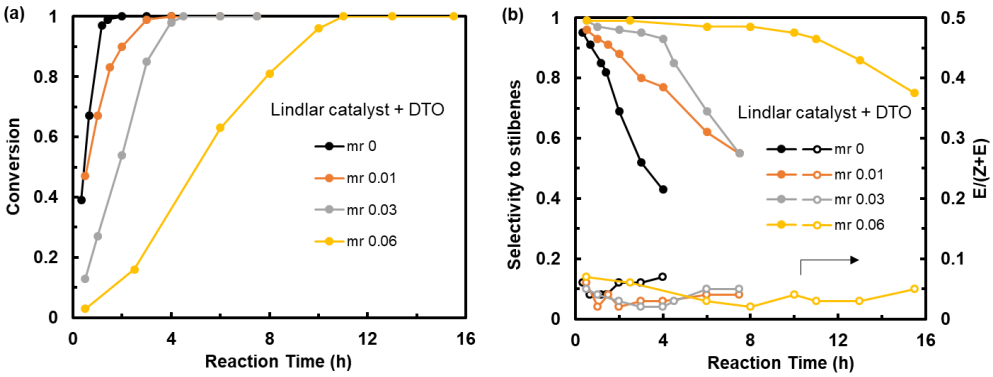

Figure 5.23 Effect of DTO at different molar ratios on the hydrogenation of DPA with the Lindlar catalyst: (a) DPA conversion and (b) stilbene selectivity and E-stilbene percentage. Other conditions: [DPA] = 0.5 M, Pd loading = 0.04 mol%, room temperature.

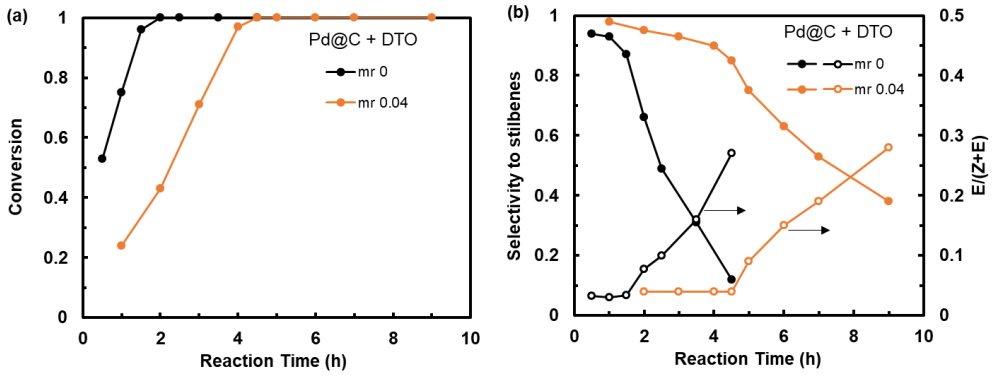

Figure 5.24 Effect of DTO at different molar ratios on the hydrogenation of DPA with the Pd@C catalyst: (a) DPA conversion and (b) stilbene selectivity and E-stilbene percentage. Other conditions: [DPA] = 0.5 M, Pd loading = 0.04 mol%, room temperature.

From the above results, DTO is a superior ligand facilitating the highly selective hydrogenation of PA. It outperforms the other ligands investigated herein with the need of lowest dosage while achieving the best selectivity. However, for the hydrogenation of DPA, its proper dosage is highly critical to render high stilbene selectivity in combination with well maintained activity.

5.3.5 Effects of Triphenylphosphine

Figure 5.25 shows the effect of triphenylphosphine on the hydrogenation of PA with I1 catalyst. The addition of triphenylphosphine at molar ratios in the range of 1.9–19.1 slightly improves the catalyst activity. Meanwhile, nearly flat selectivity curves are observed, with high, nearly constant styrene selectivity values (93–97%) maintained following the full conversion of

PA. Increasing the molar ratio slightly increase the plateau selectivity value. At the highest ratio of 50, a slight drop in catalyst activity in noted, along with a marginal up-shift of the selectivity curve.

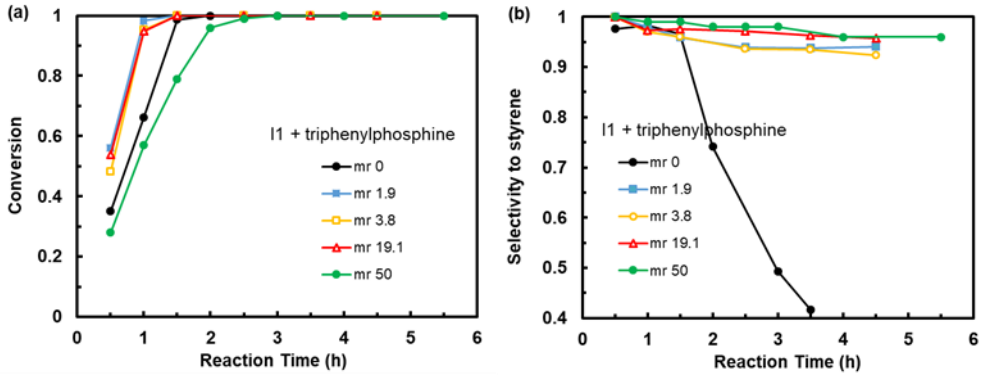

Figure 5.25 Effect of triphenylphosphine at different molar ratios on the hydrogenation of PA with the I1 catalyst: (a) PA conversion and (b) styrene selectivity. Other conditions: [PA] = 0.1 M, Pd loading = 0.04 mol%, room temperature.

With the other two heterogeneous Pd nanocatalysts, the efficiency of triphenylphosphine is, however, not as satisfying as that with the I1 catalyst though appreciable improvements are rendered. Figure 5.26 shows the hydrogenation of PA with the Lindlar catalyst in the presence of triphenylphosphine. Despite the different triphenylphosphine/Pd ratios (5–200), there are no pronounced changes in the conversion curves. Upon the full PA conversion, a gradual upshift of the selectivity curves with gradually reduced slopes is noticed. At the highest ratio of 200, the stilbene selectivity drops from 98% at 2.5 h (conversion > 99.9%) to 94% at 6 h.

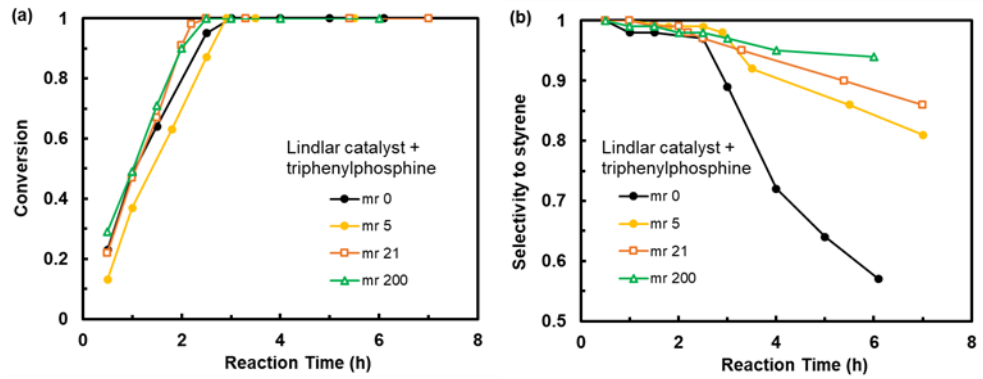

Figure 5.26 Effect of triphenylphosphine at different molar ratios on the hydrogenation of PA with the Lindlar catalyst: (a) PA conversion and (b) styrene selectivity. Other conditions: [PA] = 0.5 M, Pd loading = 0.04 mol%, room temperature.

Figure 5.27 shows the kinetic curves in the runs undertaken with the Pd@C catalyst. At the triphenylphosphine/Pd ratio of 15, relatively stable selectivity results are rendered while without the drastic reduction in catalyst activity

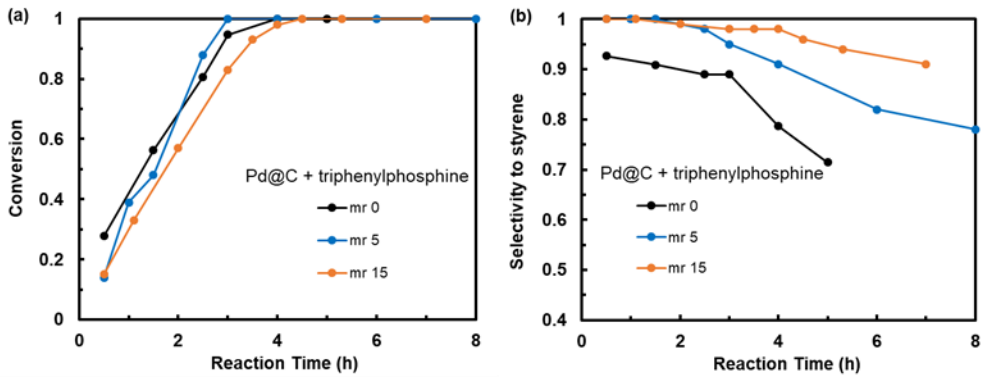

Figure 5.27 Effect of triphenylphosphine at different molar ratios on the hydrogenation of PA with the Pd@C catalyst: (a) PA conversion and (b) styrene selectivity. Other conditions: [PA] = 0.5 M, Pd loading = 0.04 mol%, room temperature.

Figures 5.28–5.30 show the effects of triphenylphosphine on the hydrogenation of DPA with the three catalysts, respectively. In general, the use of triphenylphosphine shows the clear trend of rendering the stilbene selectivity curves with reduced slopes. Increasing its dosage enhances this effect. Nevertheless, drops in the selectivity data are also noted with each catalyst.

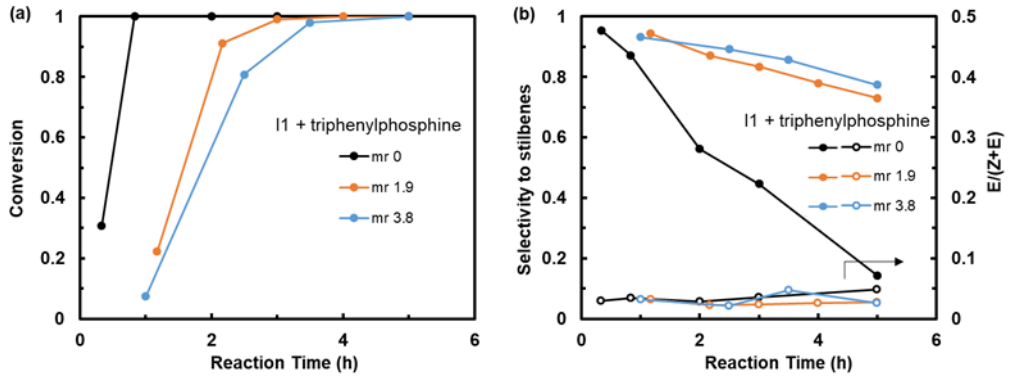

Figure 5.28 Effect of triphenylphosphine at different molar ratios on the hydrogenation of DPA with the I1 catalyst: (a) DPA conversion and (b) stilbene selectivity and E-stilbene percentage. Other conditions: [PA] = 0.1 M, Pd loading = 0.04 mol%, room temperature.

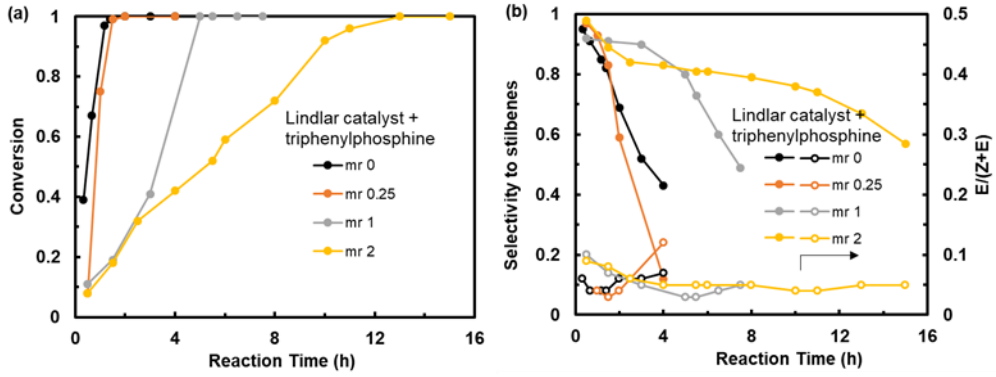

Figure 5.29 Effect of triphenylphosphine at different molar ratios on the hydrogenation of DPA with the Lindlar catalyst: (a) DPA conversion and (b) stilbene selectivity and E-stilbene percentage. Other conditions: [DPA] = 0.5 M, Pd loading = 0.04 mol%, room temperature.

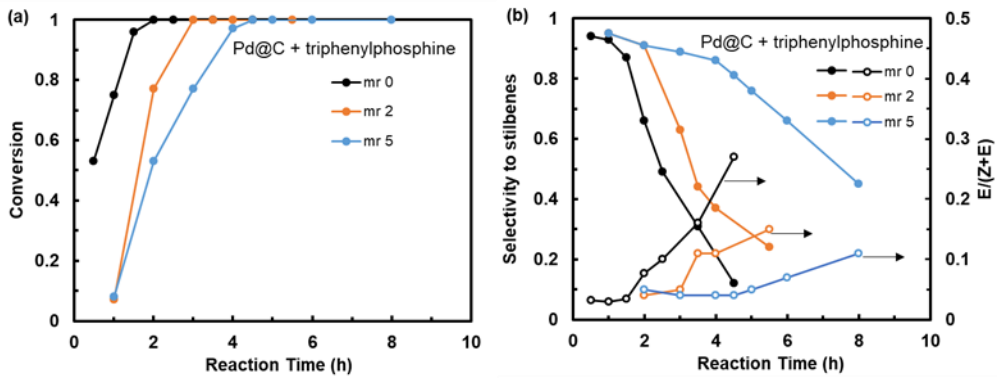

Figure 5.30 Effect of triphenylphosphine at different molar ratios on the hydrogenation of DPA with the Pd@C catalyst: (a) DPA conversion and (b) stilbene selectivity and E-stilbene percentage. Other conditions: [DPA] = 0.5 M, Pd loading = 0.04 mol%, room temperature.

5.4 Conclusions

Selective hydrogenation of PA and DPA has been studied with the use of three Pd nanocatalysts (I1, Lindlar, and Pd@C catalysts) modified with five different ligands (quinoline, pyridine, DMSO, DTO, and triphenylphosphine) with the purpose of identifying the most optimum ligands. While the effects of the ligands show some dependences on both the substrates and the nanocatalysts, this study has demonstrated a general order of the ligands in terms of their efficiency in facilitating the selective hydrogenation: DTO > triphenylphosphine > DMSO > quinoline > pyridine. Among the five ligands, sulfur-containing DTO appears to be the best ligand in facilitating the highly selective hydrogenation while requiring the lowest dosages (ligand/Pd molar ratio as low as 0.09 for PA). Both DMSO and triphenylphosphine are the second-ranked group of ligands that can also render highly selective hydrogenation but requiring significantly higher dosages (ligand/Pd ratio: around 5–400 for PA). The two N-containing ligands, quinoline and pyridine, are the third-tier ligands. These two ligands require substantially

higher loadings (ligand/Pd ratio: 1000–3000) in order to achieve significant effects. Such high loadings present serious problems for large-scale applications because of the need of their removal for product purification. The results obtained in this study is expected to provide some important guidelines in the design and selection of optimum ligands for the selective hydrogenation of alkynes facilitated by Pd nanocatalysts.

5.5 References

1. Domínguez-Domínguez, S.; Berenguer-Murcia, Á.; Linares-Solano, Á.; Cazorla-Amorós, D. *J. Catal.*, **2008**, *257*, 87−95.
2. McCue, A. J.; Guerrero-Ruiz, A.; Rodríguez-Ramos, I.; Anderson, J. A. *J. Catal.*, **2016,** *340*, 10−16.
3. Trost, B. M. *Acc. Chem. Res.*, **2002**, *35*, 695−705.
4. Fan, X.; Sans, V.; Sharma, S. K.; Plucinski, P. K.; Zaikovskii, V. A.; Wilson, K.; Tennison, S. R.; Kozynchenko, A.; Lapkin, A. A. *Catal. Sci. Technol.*, **2016**, *6*, 2387−2395.
5. Markov, P. V.; Bragina, G. O.; Baeva, G. N.; Mashkovskii, I. S.; Rassolov, A. V.; Yakushev, I. A.; Vargaftik, M. N.; Stakheev, A. Y. *Kinet. Catal.*, **2016**, *57*, 625−631.
6. Krogul-Sobczak, A.; Kasperska, P.; Litwinienko, G.; *Catal. Commun.*, **2018**, *104*, 86-90.
7. Sajiki, H.; Kuno, H.; Hirota, K. *Tetrahedron Lett.*, **1998**, *39*, 7127−7130.
8. Tejeda-Serrano, M.; Cabrero-Antonino, J. R.; Mainar-Ruiz, V.; López-Haro, M.; Hernández-Garrido, J. C.; Calvino, J. J.; Leyva-Pérez, A.; Corma, A. *ACS Catal.*, **2017**, *7*, 3721−3729.

9. McCue, A. J.; Anderson, J .A. *Catal. Sci. Technol.*, **2014**, *4*, 272−294.
10. Crespo-Quesada, M.; Dykeman, R. R.; Laurenczy, G.; Dyson, P. J.; Kiwi-Minsker, L. *J. Catal.*, **2011,** *279*, 66−74.
11. López, N.; Vargas-Fuentes, C.; *Chem. Commun.*, **2012**, *48*, 1379−1391.
12. Mori, A.; Miyakawa, Y.; Ohashi, E.; Haga, T.; Maegawa, T.; Sajik, H. *Org. Lett.*, **2006**, *8*, 3279−3281.
13. Yusuke, T.; Norifumi, H.; Takayoshi, H.; Shogo, S.; Takato, M.; Tomoo, M.; Koichiro, J.; Kiyotomi, K. *Chem. Lett.*, **2011**, *40*, 405−407.
14. Shen, L.; Mao, S.; Li, J.; Li, M.; Chen, P.; Li, H.; Chen, Z.; Wang, Y. *J Catal.*, **2017**, *350*, 13−20.
15. McKenna, F-M.; Wells, R. P. K.; Anderson, J. A. *Chem. Commun.*; **2011**, *47*, 2351−2353.
16. McCue, A. J.; McKenna, F-M.; Anderson, J. A. *Catal. Sci. Technol.*, **2015**, *5*, 2449−2459.
17. Xiang, P.; Ye, Z. *Macromolecules*, **2015**, *48*, 6096−6107.
18. Dong, Z.; Xiang, P.; Huang, L.; Ye, Z. *RSC Adv.*, 2016, 6, 43574−43590.
19. Lindlar, H.; Dubuis, R. *Org. Synth.*, 1966, 46, 89.

Chapter 6

Significant Contributions and Future Scope

6.1 Significant Contributions

In my view, the following significant contributions have been made in this thesis research to the research area.

In Chapter 2, the first surface functionalization of CNCs with ionomers containing positively charged ions through ionic interactions is demonstrated. Such functionalized CNCs have been shown to enhance dispersibility in both non-polar and low-polarity solvents, as well as in hydrophobic EOC matrix. This opens a new approach for the surface functionalization of CNCs for targeted applications through the design of desired ionomers.

In Chapter 3, a systematic study on the tensile mechanical properties of SA-CNC composite films has been undertaken. This work has revealed the desired strong tough mechanical properties of these composite films from two sustainable biopolymers, which make them promising for future applications.

In Chapter 4, a convenient large-scale in situ catalytic polymerization method has been developed for the synthesis of PCP crystal-decorated MWCNTs. This method offers a tunable control over the structure and the content of the decorating PCP crystals on the MWCNTs. Meanwhile, the PCP crystal decorated MWCNTs have been demonstrated for the facile fabrication of films of lotus leaf-like superhydrophobicity.

In Chapter 5, a systematic study on the ligand-assisted selective hydrogenation reactions of alkynes has been undertaken with the use of three different Pd nanocatalysts. Five ligands have been screened with 3,6-dithia-1,8-octanediol demonstrated to be most efficient in improving alkene selectivity while at better maintained activity. This study provides important guidelines to the efficient design of optimum ligands for selective hydrogenation of alkynes with Pd nanocatalysts.

6.2 Future Scope

The following recommendations are made for future research in the area.

(1) In Chapter 2, the ionomers used for the surface modification of CNCs were hyperbranched and thus amorphous. A promising direction will be to design and use semicrystalline polyethylene ionomers bearing the quaternary ammonium ions. Such semicrystalline polyethylene ionomers will render new enhanced properties for the modified CNCs in nanocomposite applications.

(2) In Chapter 3, the influence of microstructure on fatigue and mechanical properties of the SA-CNC composite films can be studied with the help of microscopy in the future work. This may shed light on the failure mechanism of the films, which will help the better design of films with even enhanced mechanical properties.

(3) d-MWCNT hybrid films were fabricated in Chapter 4 and the films should be solvent-resistant and heat-resistant. Further study can be undertaken to develop on the oil/water emulsion separation applications with the films at harsh conditions.

(4) Based on the results in Chapter 5, future work in the direction can be focused on the design of even more efficient S- or P-containing ligands for selective hydrogenation of alkynes.